Computational Analysis and Design of New Materials for Metal-Air Batteries

Mekonnen, Yedilfana Setarge

Publication date:
2015

Document Version
Publisher's PDF, also known as Version of record

Computational Analysis and Design of New Materials for Metal-Air Batteries

PhD Thesis

Technical University Denmark, DTU Energy

Yedilfana Setarge Mekonnen

Supervisors

Professor Tejs Vegge, DTU Energy

Associate Professor Juan Maria Garcia-Lastra, DTU Energy

Associate Staff Scientist Jens Strabo Hummelshøj, SLAC, Stanford University

October 9, 2015

Computational Analysis and Design of New Materials for Metal-Air Batteries

Submitted in candidacy for the degree Doctor of Philosophy

Yedilfana Setarge Mekonnen

Supervisors

Professor Tejs Vegge, DTU Energy

Associate Professor Juan Maria Garcia-Lastra, DTU Energy

Associate Staff Scientist Jens Strabo Hummelshøj, SLAC, Stanford University

October 9, 2015

Computational Analysis and Design of New Materials for Metal-Air Batteries

Author
Yedilfana Setarge Mekonnen
DTU Energy, Department of Energy Conversion and Storage, Technical University of Denmark, Fysikvej, Building 309, 2800 Kgs Lyngby, Denmark
E-mail: yese@dtu.dk

Supervisors
Professor Tejs Vegge
DTU Energy, Department of Energy Conversion and Storage, Technical University of Denmark, Fysikvej, Building 309, 2800 Kgs Lyngby, Denmark
E-mail: teve@dtu.dk

Associate Professor Juan Maria Garcia-Lastra
DTU Energy, Department of Energy Conversion and Storage, Technical University of Denmark, Fysikvej, Building 309, 2800 Kgs Lyngby, Denmark
E-mail: jmgla@dtu.dk

Associate Staff Scientist Jens Strabo Hummelshøj
SUNCAT Center for Interface Science and Catalysis, SLAC National Accelerator Laboratory, Menlo Park, California 94025, United States
E-mail: strabo@slac.stanford.edu

Atomic Scale Modelling and Materials
DTU Energy Conversion
Technical University of Denmark
Fysikvej 309, 2800 Kongens Lyngby, Denmark

Tel.: (+45) 46 77 58 00, Web: www.ecs.dtu.dk
E-mail: info@ecs.dtu.dk
Release date: October 9, 2015
ISBN:

Preface

This thesis is submitted in candidacy for the PhD degree from the Technical University of Denmark (DTU). It is based on the work carried out between August 2012 and October 2015 at the Section of Atomistic Modelling and Scaling (ASC) in the Department of Energy Conversion and Storage (DTU Energy) and at the Center of Atomic-Scale Materials Design (CAMD) in the department of DTU Physics. A part of the work is done in an external stay at SUNCAT Center for Interface Science and Catalysis, SLAC National Accelerator Laboratory at Stanford University, California, USA.

The project was supervised by Professor Tejs Vegge (head of the section Atomic Scale Modelling and Materials (ASC) at DTU Energy) and co-supervised by Associate Professor Juan Maria Garcia-Lastra (DTU Energy) and Associate Staff Scientist Jens Strabo Hummelshøj (at SUNCAT Center for Interface Science and Catalysis, SLAC National Accelerator Laboratory at Stanford University). The work was financially supported by the ReLiable project (project nr.11-116792) funded by the Danish Council for Strategic Research Program Commission on Sustainable Energy and Environment.

Abstract

In the last decade, great effort has been paid to the development of next generation batteries. Metal-O_2 /Air batteries (Li-, Na-, Mg-, Al-, Fe- and Zn-O_2 batteries) in both aqueous and nonaqueous (aprotic) electrolytes have gained much attention. Metal-air batteries have high theoretical specific gravimetric energy. In the case of Li-O_2, it is comparable to that of gasoline. Thus, Li-O_2 batteries could be attractive for electric vehicle manufacturers since the energy storage capacity accessible by commercially available Li-ion technology is too low to solve increasing capacity demands. However, current Li-O_2 batteries suffer from several drawbacks, e.g. dendrite formation, poor rechargeability and low capacity caused by the so-called "sudden death" at its cathode during the discharge process due to insulating discharge products. This thesis is devoted to understand the charge transport in the main reaction products of emerging nonaqueous Li- and Na-O_2 batteries at the atomistic level using the Density Functional Theory (DFT) method to address the latter problem. The role of cathode-electrolyte interface on charge transport and the implication of impurities from the air, particularly the effect of CO_2 poisoning, in the performance of the battery are addressed. The present work involves computational investigations of different charge transport mechanisms, *i.e.* ionic, coherent electron, and polaronic transport. In order to validate the outcome from DFT calculations, results are compared with relevant experiments and show a notable agreement.

The results of charge transport calculations in bulk Li_2O_2 (main discharge product in Li-O_2 batteries) revealed that though it is a wide bandgap insulator (4.96 eV) it could offer fast ionic conduction with an activation barrier of 0.40 eV. Similarly, an accessible energy barrier for sodium ion diffusion is obtained in Na_2O_2 and in NaO_2 (main discharge products in Na-O_2 batteries). The transport mechanisms at the cathode-electrolyte interfaces, *i.e.* Li_2O_2@Li_2CO_3 interface, are also examined. Lithium vacancies accumulate at the peroxide side of this interface, reducing the coherent electron transport by two to three orders of magnitude compared to bulk pristine Li_2O_2. In contrast, the Li_2O_2@Li_2CO_3 interface shows an improved ionic conduction. For polaronic transport significant differences are also found in these two scenarios. In bulk Li_2O_2 the polaronic transport at room temperature is restricted to hole polarons, whereas electron polarons display very high hopping barriers (> 1.0 eV). By contrast, it is possible to have good mobilities for electron polarons at the Li_2O_2@Li_2CO_3 interface. Finally, our studies on the reaction mechanism of Li_2O_2 revealed that the CO_2 poisoning, even at low concentrations of CO_2 effectively blocks the step nucleation site and remarkably increases overpotentials and decreases the capacity of the battery.

Resume

I det sidste årti er der blevet lagt en enorm indsats i at udvikle den næste generation af batterier. I særdeleshed metal-luft batterier (Li-, Na-, Mg-, Al-, Fe- og Zn-O_2-batterier) i enten vandige eller ikke-vandige (aprotiske) elektrolyter har fået meget opmærksomhed. Metal-luft batterier har en høj gravimetrisk energitæthed, og for Li-O_2 kemien er den sammenlignelig med benzins. Derfor kan Li-O_2 batterier åbne for produktion af nye forbedrede elektriske biler, eftersom den tilgængelige energikapacitet i markedets nuværende Li-ion batterier er for lav til at dække de stigende krav. Men Li-O_2 batterier er begrænset af flere problemer, f.eks. dendrit dannelse, lav kapacitet, dårlig genopladelighed og det såkaldte "sudden death" forårsaget af de elektronisk isolerende afladningsprodukter, der passiverer katoden. Fokus I denne afhandling er på det sidstnævnte problem, der belyses gennem øget forståelse af ladningstransporten i hovedreaktionsprodukterne i de nye og fremadstormende aprotiske Li- og Na-oxygen-batterier, opnået gennem atomarskala modellering med tæthedsfunktionalteori. Katode-elektrolyt grænsefladens role i ladningstransporten samt effekten af urenheder i luften, i særdeleshed effekten af CO_2 forurening, undersøges. Det præsenterede arbejde involverer computationelle undersøgelser af forskellige ladningstransportmekanismer, dvs. ionisk transport, koherent elektrontransport og polaronisk transport i Li- og Na-batterimaterialer. Ydermere er der udført enkelte relevante eksperimenter, der viser en rimelig overensstemmelse.

Resultaterne af ladningstransport beregningerne af afladningsprodukternes masse afslørede, at selvom Li_2O_2 er en isolator med et stort båndgab (4.96 eV), viste materialet en god ionisk ledningsevne med en aktiveringsbarriere på 0.40 eV. Ligende energibarrierer findes for natrium-ion diffusion i Na_2O_2 og NaO_2 (de dominerende afladningsprodukter i Na-O_2 batteriet). Udover studierne af ladninstransporten i afladningsprodukternes masse har vi undersøgt transportmekanismerne ved katode-electrolyt grænsefladerne i ikke-vandige Li-luft batterier, dvs. Li_2O_2@Li_2CO_3 grænsefladen. Lithium vakancer akkumulerer ved peroxid delen af denne grænseflade, og reducerer dermed den koherente elektrontransport med to til tre størrelsesordner sammenlignet med transporten i en uberørt Li_2O_2 masse. I kontrast til dette forbedrer grænsefladen den ioniske ledningsevne. I Li_2O_2 massen er polarontransporten ved stuetemperatur styret af hulpolaroner, da electronpolaronerne har en hopping barriere på mere end 1 eV. I kontrast til dette er det muligt at have en god elektronisk polarontransport i Li_2O_2@Li_2CO_3 grænsefladen. Vores studier af vækstmekanismerne for Li_2O_2 viste at CO_2 forurening, selv ved lave koncentrationer på 1%, blokerer for trin nukleations pladsen, derudover forøges overpotentialet og kapacitetes faldet dramatisk med CO_2 koncentrationen.

Acknowledgements

I have studied at Technical University of Denmark for three years and now the time has come to say thanks for those who collaborate and helped me along the way. First of all I would like to express my gratitude to my supervisor Tejs Vegge for guiding me throughout the project and for his motivation and valuable comments, and also for giving me a chance to try a number of different things beyond the project. I would like to thank my co-supervisor Juan Maria Garcia-Lastra for the continuous support of my PhD study and also supporting me to get insight to the basics of DFT and different codes. I would also like to thank my co-supervisor Jens Strabo Hummelshøj for making possible my external stay at Suncat, SLAC national accelerator laboratory Stanford University and for fruitful discussions.

Beside my supervisors, I would also like to thank my colleagues for stimulating discussions and for a good working environment and for various helps along the way to mention few Jon Steinar, Peter Jensen, Steen Lysgaard, Rune Christensen, Kristian, Jonathan, Poul, Johan and so many other. My special thanks go to colleagues who proofread the thesis and gave me helpful comments and suggestions Peter, Steen, Rune, Vladimir, Supti, Arghya, Nicolai and Simon. I would also like to thank administrative staffs for facilitating things at DTU in general and DTU Energy and DTU Physics (CAMD) in particular. Last but not the least, I would like to thank my wife Tilaye for taking care of our children Buruktawit and Abiy, and supporting me in versatile ways.

Copenhagen, October 9, 2015
Yedilfana Setarge Mekonnen

Contents

List of Figures

List of Tables

CHAPTER 1

Introduction

The accessibility of energy sources is a critical issue for the future of mankind. It is vital for the well-being and also determines the standard of living. Nowadays, billions of people do not have access to electricity and again billions of people worldwide still use conventional fuels for household purposes, especially in the developing countries. [1] Therefore, in order to secure their surplus energy demand, many developing nations are constructing grand power systems, mostly from renewable sources (for example Ethiopia is constructing a 6 GW hydro power on Nile River [2]). Whereas, most developed nations had already reached a steady state in terms of additional energy requirements about three decades ago. Currently, these countries engaged on the process of replacing traditional fuels with renewable ones. For example, Denmark has set a target to have fully phased out fossil fuels in 2050. [3]

If the global fossil-fuel consumption continues at the current pace the concentration of CO_2 in the atmosphere is anticipated to be doubled by 2050 and tripled by 2100. As a consequence, an average global warming is estimated to be about 4.5 ^{o}C by 2100. This global warming could potentially be reduced to 3 ^{o}C or increased to 6 ^{o}C depending on the degree to which society utilizes fossil fuels and renewable energy sources as illustrated in Figure 1.1. [4][5] Regardless of the remarkable oil-price drop during autumn 2014 and the increase in global energy consumption (annually growth, 1.5 % in recent years), the share from renewable energy grew persistently in 2014, and for first time in the last 40 years the world-wide carbon emission linked with energy consumption remained steady [2], thanks to sustainable energy alternatives (renewables).

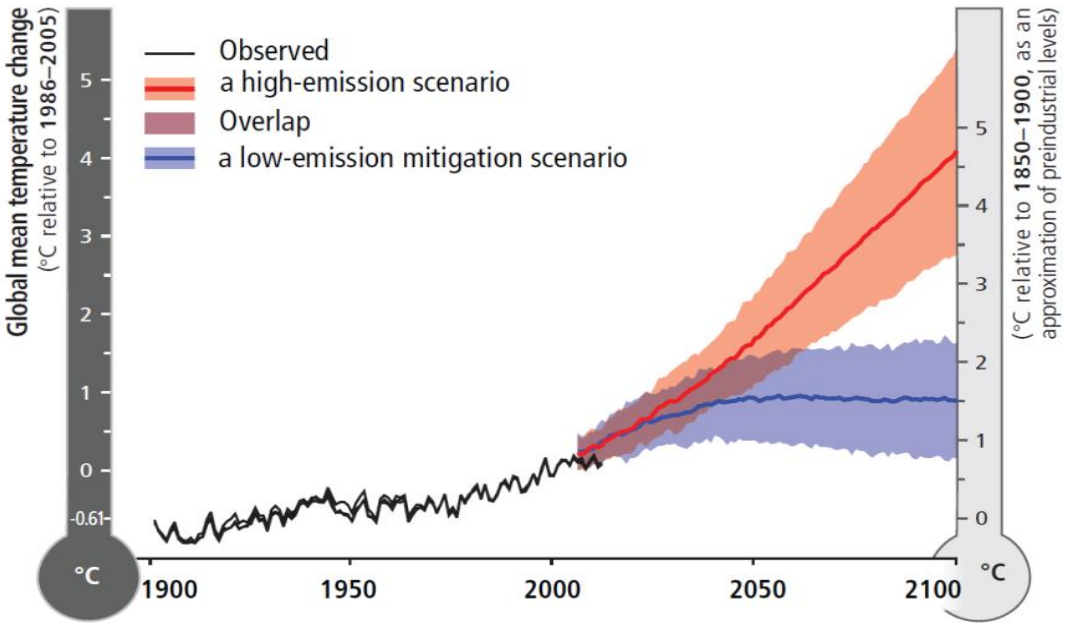

Figure 1.1: The surface air global temperature changes depend on net emissions of greenhouse gases in a low- and a high-emission mitigation scenario projected till 2100. Source: IPCC 2014 report [4].

1.1 Renewable Energy

According to Renewables 2015 Global Status Report [2], about 19.1 % of the 2013 global energy supply was input from all renewable energy sources such as wind energy, solar energy, hydroelectricity, geothermal, biomass and biofuel. However, above 78.3 % of the global energy supply is still coming from the fossil fuels, and the remaining 2.6 % share is from nuclear power. About 78 % of the total greenhouse gases (GHGs) emission increase in the last four decades is coming from direct CO_2 emissions from fossil fuel combustion and industrial processes. In particular, in the last decade (2000-2010) the highest emission levels in human history were recorded. For instance, in 2010 alone, 49 (± 4.5) Gt of CO_2 equivalents was released. [6] These emissions cause changes to the world climate and disrupts nature and human systems universally. Thus, it is necessary to reduce CO_2 emissions. The only way to this, in a scenario in which global energy demand is rising, is to significantly increase the energy share from renewable sources. Considering that approximately half of the CO_2 emissions originate from the transportation sector, a plausible measure is to gradually replace the fossil-fuel propelled vehicles by electric vehicles (EVs) charged using energy from a renewable source.

In this regard, the progress towards renewables particularly in the transport sector has been impressive in the recent times. Despite the fact that commercially available electric vehicles (EVs) are expensive and only offer short driving range per charge, the demand for electric vehicles is growing rapidly. For example, according to the latest REN21's 2015 report [2], the number of EVs in use in 2014 is nearly doubled compared to 2013, *i.e.* the number of electrified vehicles increased from 350, 000 to 665,000. According to recent energy reports, the higher share of CO_2 emissions from energy supplies next to industries is that of the transportation sector.[6] Therefore, the ongoing electrification of vehicles in the transportation sector will play a very important role in mitigating a significant amount of direct CO_2 emissions to the environment and thereby regulating the climate changes. As can be seen in Figure 1.2, the cost of Li-ion battery packs for electric vehicles are promptly decreasing. [7] A long-term global-emission goal can also boost further energy technology development. [4]

1.1.1 Batteries: Li-ion Batteries

Batteries or electrochemical cells convert the stored chemical energy directly into electrical energy. The first electrochemical battery was built in 1800 by Alessandro Volta using copper and zinc electrodes and brine (NaCI solution) socked paper as an electrolyte. Latter in 1836, John Frederic Daniell invented the Daniell cell that paved the way for modern battery technologies. A subsequent development and emergence of new battery technologies have taken place since then. Batteries can be divided into two major types: Primary and secondary batteries. The former one is a disposable battery type. Once this type of batteries stops producing currents, it is disposed of. However, the latter type of batteries, also known as rechargeable batteries, can be charged and discharged for multiple times.

Nowadays, secondary batteries are present almost everywhere. Particularly the Li-ion batteries are used to power both small-sized appliances such as watches, hearing aids, smart phones, laptops and GPS devices and large devices such as power backups and electric vehicles. Rechargeable lithium batteries were introduced in 1978 by Whittingham *et al.* [8]. In 1981, Goodenough *et al*. [9] made a significant contribution to the technology by discovering the cathode material Li_xCoO_2 for the Li-ion battery. Since then, countless efforts have been made to advance the technology and latter in 1991, Sony succeeded in commercializing the first Li-ion battery.

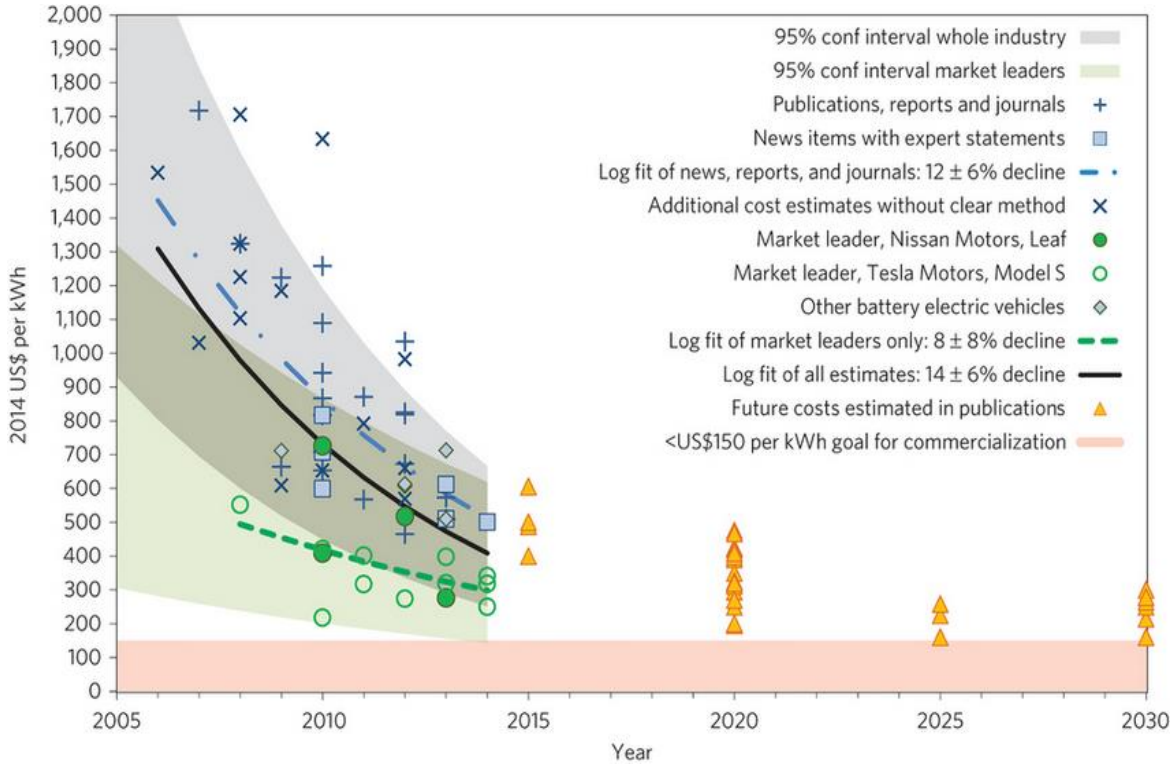

Figure 1.2: Cost of Li-ion battery packs in battery EVs til 2030. Figure is taken from.[7]

The searches for improved Li-ion battery materials for versatile applications have been greatly accelerated. However, regarding the application of Li-ion batteries to EV, there are still several drawbacks associated with this technology compared to gasoline, such as low driving range, high price and low energy/power densities and theoretical limitations of the technology by itself. Therefore, in addition to the improvement of the existing Li-ion battery performance, it is also equally important to investigate other alternatives beyond Li-ion batteries, *i.e.* next generation batteries that comprise the metal-air battery technology as a promising candidate.

The main motivation of this work is therefore to study the burgeoning renewable energy technology of metal-air batteries displaying the highest theoretical specific energy (see the comparison plot for various battery types in Figure 1.3). [7][10][11] In particular, the Li-O_2 and Na-O_2 batteries show great potential to provide a driving range competitive to that of fossil-fuel based locomotive technologies.

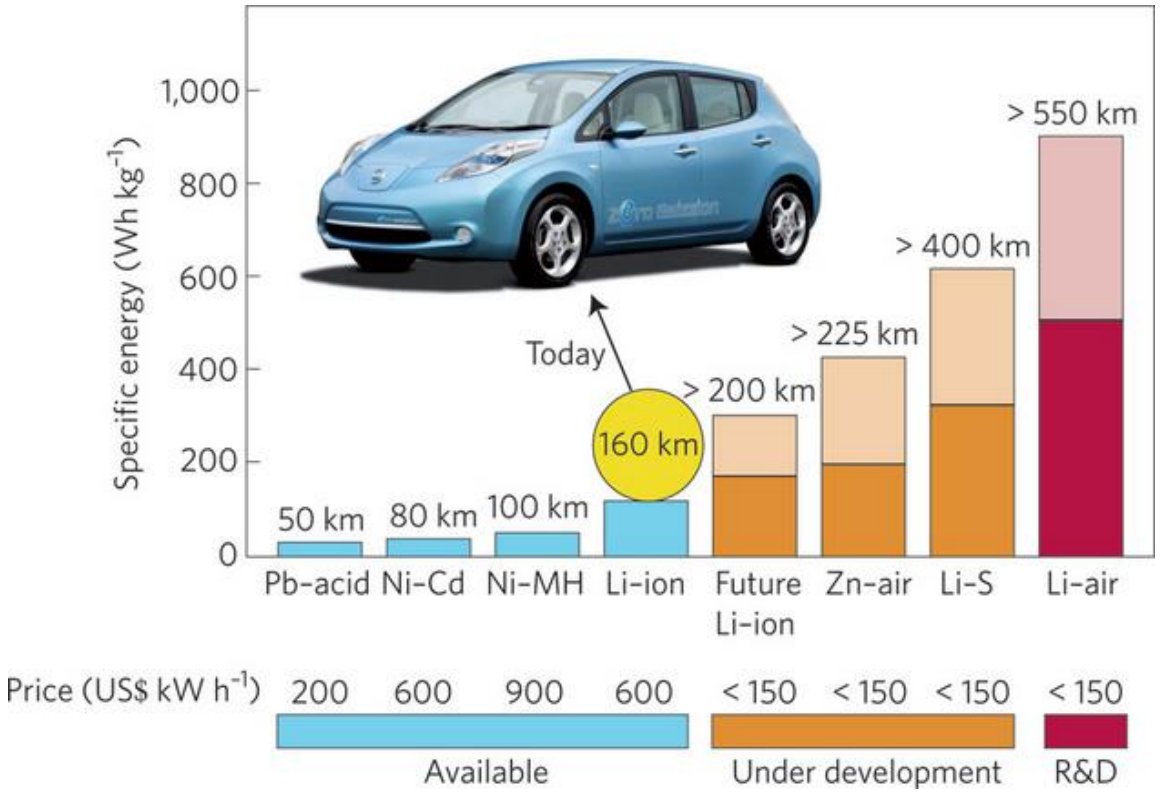

Figure 1.3: Practical specific energies (Wh Kg^{-1}) for prevalent secondary battery technologies, with the existing and estimated driving range and pack prices (US$ kW h^{-1}). Figure is taken from [11] with permission.

1.1.2 Next Generation Batteries: Metal-O_2 /Air Batteries

In the last decade, enormous effort has been paid to the development of next generation batteries. In particular metal-O_2 /Air batteries (Li-, Na-, Mg-, Al-, Fe- and Zn-O_2 batteries) in either aqueous or nonaqueous (aprotic) electrolytes have gained a lot of attention. [12][13] Metal-air batteries have high specific gravimetric energy comparable to gasoline in the case of Li-O_2 chemistry. Thus Li-O_2 batteries could be an alternative to the existing Li-ion battery technology [14]. Metal-air batteries have high theoretical specific energies since the technology use metal as an anode and oxygen gas from air as a cathode. The reaction products are either oxides, peroxides or superoxides during discharge depending on the experimental conditions and cell components used in the system. The oxygen reduction (ORR) and oxygen evolution reaction (OER) are the two main reactions taking place reversibly during discharge and charge, respectively.

The aprotic Li-air (shortly, Li-O_2) battery offer extremely high specific energy (comparable to gasoline, see Figure 1.4) [15] that is nearly an order of magnitude higher than that of the existing Li-ion batteries (latest specific capacity ~300 mAh/g) [16]. However, in practice nonaqueous Li-air batteries suffer from numerous drawbacks that must be solved before they enter to the market. The worst drawback of the Li-O_2 battery is the so-called "sudden death" of the battery, due to the formation of a passivation layer in the cathode during the discharge. [17][18] In the last couple of years nonaqueous Na-O_2 battery was reported as a promising alternative to the Li-ion battery with a specific capacity of ~1500 mAh/g [19], which is about half of the state of the art Li-O_2 battery specific capacity, *i.e*. ~3842 mAh/g [15]. The former could offer low cost and low overpotentials even at too high current densities that account for high electrical energy efficiency of ~ 90 % [20].

1.2 Thesis Outline

This work collects theoretical investigations of the charge transport mechanisms at the cathode of Li- and Na-O_2 batteries. The modeling presented in the thesis is based mainly on Density Functional Theory (DFT) calculations. [21][22] DFT+U (DFT combined with Hubbard's correction (U) for insulator systems) [23] as it is implemented in the GPAW code [24] is used for polaronic conduction studies and a non-equilibrium Green's function (DFT-NEGF) [25] is applied to obtain the coherent electron transport measurements (*I-V* curves) in the tunneling regime. In addition to the large volume of theoretical investigations some relevant experiments have been carried out by experimentalist colleagues in our group in order to validate the theory. The main tasks addressed in this thesis are the following:

- We have looked at charge transport (ionic and coherent electronic and polaronic transport) in the bulk of different reaction products at the cathode of the newly emerging metal-air batteries, *i.e.* Li_2O_2 for the Li-O_2 battery and NaO_2 and Na_2O_2 for the Na-O_2 battery.
- In addition to the study of charge transport in the bulk of discharge products in Na- and Li-O_2 batteries, we have examined the transport mechanisms at the cathode-electrolyte interfaces in nonaqueous Li-O_2 /Air battery, *i.e.* the Li_2O_2@Li_2CO_3 interface.
- We have carried out reaction mechanism studies (growth/depletion) on some selected step surfaces with and without air impurities to reveal the effect of CO_2 poisoning on the overpotential and capacity of the nonaqueous Li-air battery. Similarly, the effect of step surfaces of (001) and (100) facets of NaO_2 and $(1\bar{1}00)$ facets of Na_2O_2 on dis/charge overpotentials have also been studied.

Excluding the introduction chapter the rest of the thesis is organized in five chapters as follows.

Chapter 2: This chapter covers the concepts and basic principles of electronic structure calculations in general and density functional theory (DFT) in particular. Different computational methods applied in the work are presented in subsections.

Chapter 3: The pros and cons of nonaqueous rechargeable Li-O_2 batteries (when only pure oxygen is considered) and the working principle of the state of the art Li-O_2 battery are discussed. In addition, electronic properties and main results of the ionic, coherent electronic transport and polaronic conduction studies in Li_2O_2, the main discharge product, are presented.

Chapter 4: The chapter focuses on the implication of air impurities, particularly the influence of carbon dioxide poisoning, on the overpotentials and capacity of the nonaqueous secondary Li-air battery. The results of the modeling are compared with experimental work carried out in our group. The stability of aprotic electrolytes and graphite cathode are discussed in brief. Moreover, the charge transport (ionic, coherent electron tunneling and polaronic) at the cathode-electrolyte interface (CIE), particularly the Li_2O_2@Li_2CO_3 interface is discussed in detail. Finally, the summary of the charge transport and CO_2 poisoning studies are presented in brief.

Chapter 5: This chapter provides a general overview of the nonaqueous rechargeable Na-O_2 battery and computational reaction mechanism studies on some selected stable step surfaces of NaO_2 and Na_2O_2 (the two main reaction products in Na-O_2 batteries). Moreover, the ionic conduction studies in both NaO_2 and Na_2O_2 materials and polaronic conduction studies in Na_2O_2 are discussed. Finally, the summary of the growth/depletion on step surfaces and charge transport studies in NaO_2 and Na_2O_2 are presented in brief.

Chapter 6: The summary of the present work and an outlook on the future are presented in this chapter.

List of Papers

This work produced two peer reviewed publications and one manuscript to be submitted. All are attached at appendixes.

Paper I

The Influence of CO_2 Poisoning on Overpotentials and Discharge Capacity in Nonaqueous Li-Air Batteries

Yedilfana S. Mekonnen, Kristian B. Knudsen, Jon S. G. Mýrdal, Reza Younesi, Jonathan Højberg, Johan Hjelm, Poul Norby, Tejs Vegge

The Journal of Chemical Physics **140**, 121101 (2014); doi: 10.1063/1.4869212

Paper II

Role of Li_2O_2@Li_2CO_3 Interfaces on Charge Transport in Nonaqueous Li-Air Batteries

Yedilfana S. Mekonnen, Juan M. Garcia-Lastra, Jens S. Hummelshøj, Chengjun Jin, Tejs Vegge

The Journal of Physical Chemical C 2015, 119 (32), 18066-18073 DOI: 10.1021/acs.jpcc.5b04432

Paper III

Thermodynamic and Kinetic Limitation of Sodium Peroxide and Formation of Sodium Superoxide in Na-O_2 Batteries (*to be submitted*)

Yedilfana S. Mekonnen, Rune Christensen, Juan M. Garcia-Lastra, Tejs Vegge

CHAPTER 2

Electronic Structure Methods

This chapter provides an overview on the theoretical background and the computational tools that are applied in the work presented in this thesis. This chapter will cover the concepts and basic principles of electronic structure calculations in general and density functional theory (DFT) in particular. DFT is a technique that allows solving a Schrödinger equation in approximate, accurate and affordable way. In order to solve strongly correlated systems we apply a special DFT flavor that is DFT + U, which will be briefly introduced in section 2.2. Moreover, other algorithms based on DFT results such as NEB and NEGFs will be discussed in this chapter. The NEB method is used to describe the transition state energy between two stable sates. The NEGFs method is used to estimate the coherent electronic transport in the material that is connected between two leads. We will discuss these methods separately in sections.

Firstly, we will start by introducing the time independent Schrödinger equation, which is the basis of all electronic structure methods, including DFT.

2.1. The Time Independent Schrödinger Equation

In principle, any observable properties of a given system can be obtained by solving the time independent Schrödinger equation which is an eigenvalue equation. The time independent Schrödinger equation for an isolated system containing N electrons and M nuclei is described by

$$\hat{\mathrm{H}}\Psi = \mathrm{E}\Psi \tag{2.1}$$

where $\Psi\left(\mathrm{r}_1, \mathrm{r}_{2,} \ldots \mathrm{r}_{\mathrm{N},} \mathrm{R}_1, \mathrm{R}_{2,} \ldots \mathrm{R}_{\mathrm{M}}\right)$ is the wave function (eigenfunction) describing the quantum state of the system depending on the spatial coordinates of the electrons, $\mathrm{r}_{\mathrm{i},}$ and the nuclei R_{j}. E are the eigenvalues of the system. The Hamiltonian operator $\hat{\mathrm{H}}$ of the system can be written as,

$$\hat{\mathrm{H}} = \overbrace{-\frac{1}{2}\sum_{i=1}^{N}\nabla_i^2}^{\hat{T}_e} \overbrace{-\frac{1}{2}\sum_{A=1}^{M}\frac{1}{M_A}\nabla_A^2}^{\hat{T}_N} \overbrace{-\sum_{i=1}^{N}\sum_{A=1}^{M}\frac{Z_A}{r_{iA}}}^{\hat{V}_{Ne}} \overbrace{+\sum_{i=1}^{N}\sum_{j>i}^{N}\frac{1}{r_{ij}}}^{\hat{V}_{ee}} \overbrace{+\sum_{A=1}^{M}\sum_{B>A}^{M}\frac{Z_A Z_B}{R_{AB}}}^{\hat{V}_{NN}} \tag{2.2}$$

where the first two terms $\hat{T}_e$ and $\hat{T}_N$ are the kinetic energy contributions from N electrons and M nuclei, respectively. The potential energies contributions from the electrostatic interactions are respectively, nucleus-electron $(\hat{V}_{Ne})$, electron-electron $(\hat{V}_{ee})$ and nucleus-nucleus $(\hat{V}_{NN})$ interactions. The distance between electron and nucleus is described as $r_{iA} = |r_i - R_A|$ and similar denotations apply to define distances between electron-electron (r_{ij}) and nucleus-nucleus(R_{AB}).

Equation (2.2) is in general very complex, and in order to make tractable and solve it, some approximations need to be done. The first of these approximations is the so-called Born-Oppenheimer Approximation.

Born-Oppenheimer Approximation is an assumption that separates the electronic and nuclear motion for a given system and treats them independently. The approximation relies on the fact that the two particles have enormous differences in weight. A nucleus is much heavier than an electron, approximately 2000 times higher than that of an electron. Therefore, electronic motion is 3-5 orders of magnitude faster than that of the nuclei.

Thus, in the Born-Oppenheimer Approximation the time independent Schrödinger equation is first solved for the electronic part fixing the nuclei positions at a given geometry.

$$\hat{\mathrm{H}}_{ele}\varphi_i(\vec{\mathrm{r}}_{N,}\vec{\mathrm{R}}_M) = \in_i (\vec{\mathrm{R}}_{M,})\,\varphi_i(\vec{\mathrm{r}}_{N,}\vec{\mathrm{R}}_M) \tag{2.3}$$

where $\hat{\mathrm{H}}_{ele}$ is the electronic Hamiltonian that can be solved is written as follows

$$\hat{\mathrm{H}}_{ele} = \overbrace{-\frac{1}{2}\sum_{i=1}^{N}\nabla_i^2}^{\hat{T}_e} \overbrace{-\sum_{i=1}^{N}\sum_{A=1}^{M}\frac{Z_A}{r_{iA}}}^{\hat{V}_{Ne}} \overbrace{+\sum_{i=1}^{N}\sum_{j>i}^{N}\frac{1}{r_{ij}}}^{\hat{V}_{ee}} \tag{2.4}$$

The three terms are the kinetic energy of the moving electrons$(\hat{T}_e)$, the electrostatic interaction between the electrons $(\hat{V}_{ee})$ and the electrostatic interactions between the electrons and the frozen nuclei $(\hat{V}_{Ne})$.

It should be remarked that the coordinates of nuclei only enter as parameters in equation (2.4). φ_i, is the eigenfunction of the reduced Schrödinger equation of the electronic Hamiltonian, $\hat{H}_{ele}$, and $\in_i$ are the corresponding eigenvalues.

Once the electronic part of the Hamiltonian is solved for a set of different nuclear coordinates, it is possible to solve the nuclear part of the Hamiltonian.

$$\hat{\mathrm{H}}_{nuc}\phi_j(\vec{\mathrm{R}}_M) = \mathrm{E}_{tot}(\vec{\mathrm{R}}_M)\phi_j(\vec{\mathrm{R}}_M) \tag{2.3}$$

where $\hat{\mathrm{H}}_{nuc}$ can be described as

$$\hat{\mathrm{H}}_{nuc} = \overbrace{-\frac{1}{2}\sum_{A=1}^{M}\frac{1}{M_A}\nabla_A^2}^{\hat{T}_N} + \overbrace{\sum_{A=1}^{M}\sum_{B>A}^{M}\frac{Z_A Z_B}{R_{AB}}}^{\hat{V}_{NN}} + \in_i(\vec{\mathrm{R}}_M) \tag{2.4}$$

E_{tot} is the total energy of the system (including nuclei and electrons).

It should be noticed that the eigenvalues of the electronic part of the Hamiltonian, $\in_i$, enter as a potential in the nuclear part of the Hamiltonian. The total wave functions of the system are then written as:

$$\Psi(\vec{\mathrm{r}}_N, \vec{\mathrm{R}}_M) = \varphi_{ele}(\vec{\mathrm{r}}_N, \vec{\mathrm{R}}_M)\phi_{nuc}(\vec{\mathrm{R}}_M) \tag{2.5}$$

2.2. Density Functional Theory (DFT)

Density functional theory (DFT) is, by far, the most popular technique applied to solve the electronic part of the Schrödinger equation in systems within the range from 10 to 1000 atoms. DFT was initially introduced in 1964 when Hohenberg and Kohn come up with electron density, $\rho(\mathrm{r})$, as an essential quantity to tackle a complex many body problem instead of the wave function.[21] [26]

The density functional theory reduces the 3N variables in the wave function for N particles to only 3 variables, keeping a reasonably high degree of accuracy. As a consequence, the electronic structure calculation reduces its cost drastically.

DFT has its foundation on the Hohenberg-Kohn Theorems. The first theorem states that *the electronic density, $\rho(r)$, of the ground state of a system is uniquely defined by the external potential applied to it*. In our case the external potential is the electron-nuclei potential.

According to this theorem, the ground state energy of a system can be expressed as a functional of the electron density as shown below.

$$E[\rho(r)] = T[\rho(r)] + \ U[\rho(r)] + V[\rho(r)] \tag{2.6}$$

where the first term is the kinetic part, the second term refers the electron-electron interaction and the last term is the external potential due to stationary nuclei. The second theorem stated that *the energy obtained from the trial density, $\acute{\rho}(r)$, is always less than or equal to the ground state energy, E_O, described as*

$$E_O \leq E|\acute{\rho}(r)| \ ; \ E_O = \min_{\rho} E|\acute{\rho}(r)| \tag{2.7}$$

The ground state energy can be obtained according to the variational principle until we reach to the density that minimizes the total energy that corresponds to the exact ground state density. Once the ground state density of the N-electrons system is determined then other properties can be calculated as a response function.

Once that the total energy of the ground state of a system has been demonstrated to be uniquely determined by its electronic density it is necessary is necessary to find a practical way to obtain both the electronic density of the ground state and its energy. This is done by solving the Kohn-Sham equations. The starting point for solving the Kohn-Sham equations is a set of *fictitious* non-interacting electrons. However, they are employed in such a way that the density of these *fictitious* non-interacting electrons is the same as the exact density of the real system. The Kohn-Sham equations are described by the local effective external potential usually denoted as $V_{eff}(r)$ in which the fictitious electron move. This is also known as the Kohn-Sham potential, $V_{KS}(r)$.

$$V_{KS}(r) = \overbrace{\int \frac{\rho(r')}{|\mathrm{r} - \mathrm{r}'|} dr'}^{V_H[\rho(r)]} + v_{ext}(r) + v_{xc}(r) \tag{2.8}$$

The first term refers to the Hartree potential, $V_H[\rho(r)]$, which takes into account the coulombic repulsion interaction between one electron and the mean electron density. It should be noticed that $V_H[\rho(r)]$ contains the repulsive interaction of one electron with itself. The second term is the coulombic interaction between the electron and nuclei. The last term, $v_{xc}(r)$, describes the

exchange-correlation functional that takes care of the exchange term (based on Pauli principle) and the correlation term. Apart of the exchange based on Pauli principle, the exchange part of $v_{xc}(r)$ contains an attractive interaction of an electron with itself which should, cancel out the repulsive self-interaction of the Hartree term. The correlation accounts for the potential that is not incorporated in the Hartree term; since in reality a single electron normally interacts not to the mean rather with the rest of all individual electrons.

In the Kohn-Sham formalism $V_H[\rho(r)]$ and $v_{ext}(r)$ are treated exactly. However, the exact analytical expression for $v_{xc}(r)$ is unknown and it needs to be approximated. We will present some of the most common approximations for $v_{xc}(r)$ later in this chapter.

The single particle Schrödinger equation for non-interacting particles is based on the Kohn-Sham potential is given by

$$\hat{\mathrm{H}}_{ks}\,\Psi_i(r) = \left(-\frac{1}{2}\nabla^2 + V_{KS}(r)\right)\Psi_i(r) = \epsilon_i\ \Psi_i(r) \tag{2.9}$$

The solution to the KS Hamiltonian is wave function which consists of a slater determinant of one-electron wave functions for N particle system.

$$\Psi_{ks} = \frac{1}{\sqrt{N!}}\,det[\varphi_1\varphi_2 \ldots \varphi_N] \tag{2.10}$$

Thus, the total electronic density of the system is expressed as $\rho(r) = \sum_i \Psi_i^*(r)\,\Psi_i(r)$. Since V_{KS} depends on $\rho(r)$ and $\rho(r)$ depends on $\Psi_i(r)$, $V_{KS}(r)$ depends itself on the solutions of equation (2.9). This makes that the KS equations must be solved consistently. An initial guess electron density, $\rho(r)$ is used to solve equation (2.9). This allows obtaining a new electronic density which is used to build a new $V_{KS}(r)$, which is used to solve equation (2.9) again. The convergence reaches numerically through some self-consistent iterations, see Figure 2.1.

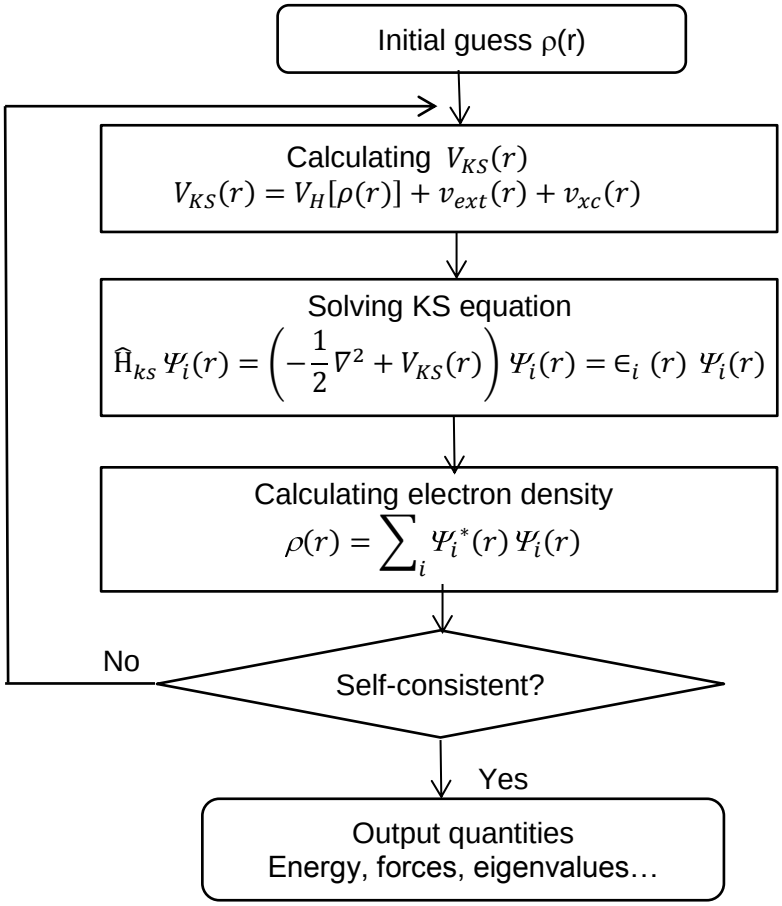

Figure 2.1: A simplified flowchart that illustrate the self-consistency loop for solving KS equations.

We will introduce now three of the most common exchange correlation functionals in DFT, namely, the Local Density Approximation (LDA), the General Gradient Approximation (GGA), and Hubbard-Corrected DFT functionals (DFT + U). The local density approximation (LDA) [22] is one of the simplest approximations to the exchange correlation. This approximation relies only on the local density and is written as

$$E_{XC}^{LDA} = \int \varepsilon_{XC}(\rho)\rho(r)d^3r \tag{2.11}$$

where $\varepsilon_{XC}(\rho)$ is the exchange correlation energy of a homogeneous electron gas. The exchange part for the homogenous electron gas can be solved analytically and it can be written as:

$$\varepsilon_X[\rho] = \frac{3}{4}\left(\frac{3}{\pi}\right)^{1/3}\rho^{1/3}$$

However, to tackle the correlation part, high accuracy quantum Monte-Carlo simulations [27] method should be applied. By fitting these Monte-Carlo simulations to analytical expressions it is possible to obtain a correlation functional. The ones proposed by Perdew and Zunger [28], and by Vosko, Wilk and Nusair [29] are the most widely employed. Improvements relative to the LDA functionals are the GGA functionals which take into consideration the densities gradient as shown below

$$E_{XC}^{GGA} = \int \varepsilon_{XC}(\rho_{\uparrow}, \rho_{\downarrow}, \nabla\rho_{\uparrow}, \nabla\rho_{\downarrow})\rho(r)d^3r \tag{2.12}$$

There are a number of functionals formulate on GGA approximation that are optimized for different applications. Among the most used GGA based exchange and correlation functionals are PW-91 (Perdew−Wang) [30], PBE (Perdew-Burke-Ernzerhof) [31] and RPBE (revised Perdew-Burke-Ernzerhof [32] functionals.

As we have mentioned before, $v_{xc}(r)$ should include an attractive potential between the electron and itself which has to cancel out the repulsive self-interaction part of the Hartree potential. In the case of the homogeneous electron gas this cancellation occurs, both in LDA and GGA. However, in many systems, in particular molecules, semiconductors and insulators, the $v_{xc}(r)$ in LDA and GGA do not cancel completely the repulsion of one electron by itself. This is called the self-interaction error (SIE). SIE is the main source of the underestimation of bandgaps observed with LDA and GGA. Moreover, SIE leads to a wrong description of the localization of charge (*i.e.* polarons) in solids.

One possibility to palliate the SIE is to use the so-called Hubbard-corrected functional, referred also in the literature as DFT+U. In DFT+U an additional U parameter correction is introduced to the ordinary DFT method to account for the strong coulomb interaction of localized electrons at a particular orbital. The U parameter basically describes the strength of the on-site coulomb interactions and the on-site exchange interaction. The U parameter can be extracted from ab-initio calculations, but often is obtained semi-empirically. The DFT+U corrections can be implemented in different ways. In this thesis we use the one proposed by Anasimov *et al*. [23] In the Anasimov DFT+U implementation the total energy is written as:

$$E_{DFT+U} = E_{DFT} + \sum_{a} \frac{\mathrm{U}_{eff}}{2} Tr(\rho^a - \rho^a\rho^a) \tag{2.14}$$

where ρ^a is the atomic orbital occupation matrix. Thus we add a penalty functional to the DFT total energy expression that forces the on-site occupancy matrix to be either fully occupied or fully unoccupied levels.

DFT + U (precisely, RPBE+U) methodology is vastly employed in the work presented in this thesis. This method is mainly applied to investigate the localization of holes and electrons at the 2p orbitals of oxygen and/or carbon of systems that contain peroxide, carbonate, or superoxide ions.

2.3. Transition State Theory (TST)

TST explains the reaction times between two stable/meta-stable configurations of a system, *i.e.* the initial and final states. The energy barrier between the two configuration, E_b, is usually called activation energy of transition. According to Arrhenius law the transition rate between the initial and final state depends on E_b as follows:

$$r(T) = vExp^{\left(\frac{-E_b}{k_B T}\right)} \tag{2.15}$$

where the prefactor v is the so-called attempt frequency or hopping rate, it is given by ($v = \frac{\Pi\omega_{IS}}{\Pi\omega_{TS}}$)

where ω_{IS} and ω_{TS} are the vibrational frequencies at the initial and saddle points respectively within harmonic transition state theory. [33]

The diffusion coefficient (D) of a particular defect can be determined using $D = va^2e^{-E_b/k_BT}$. It can be simplified as $D = a^2r$, where a is the jump length.

2.4. Nudge Elastic Band (NEB) Method

The nudged elastic band (NEB) method [33-35] is the most popular computational tool to locate the transition states and their corresponding E_b. NEB method optimizes a set of intermediate images along the path that connects the initial and final states. Each image is optimized applying constrains that forces an equal spacing between neighboring images. The constrains are imposed through a force $\mathrm{F_i^{NEB}}$, made of two components (see Figure 2.2), namely: The parallel force also known as the spring force ($\mathrm{F_i^{S||}}$) that tie the neighboring images and prevents them from moving into either the initial or final states. The other component is true force perpendicular to the path ($\mathrm{F_i^{\perp}}$). The force acting on an individual image i is then changed from $\mathrm{F_i}$ to $\mathrm{F_i^{NEB}}$ ($\mathrm{F_i^{NEB}} = \mathrm{F_i^{S||}} + \mathrm{F_i^{\perp}}$).

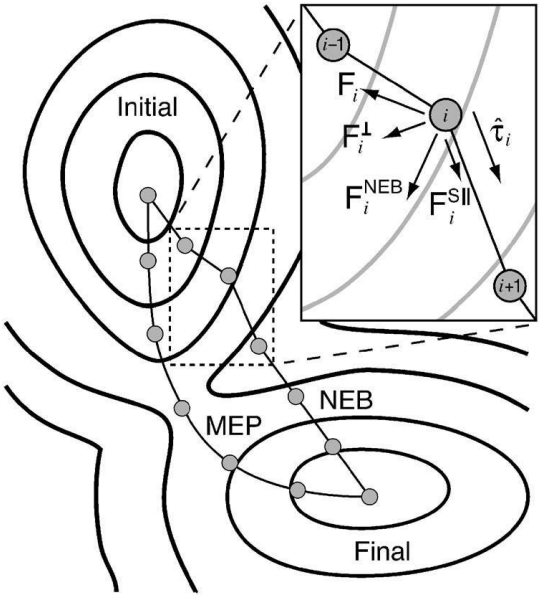

Figure 2.2: An illustration of a potential energy land scape drawn by contour lines between the relaxed initial and final states separated by a number of intermediate images connected by a spring. Figure is taken from [114].

The energy barrier for defect migrations (ionic diffusion and polaron hopping) are obtained from a slightly modified NEB method, *i.e.* the climbing image nudge elastic band method (CI-NEB) [36]. The latter improves the energy barrier for finding the minimum energy pathway in such a way that the highest energy image is made to climb up to the saddle point. This image will be converged at the exact saddle point.

2.5. Nonequilibrium Greens Function (NEGFs)

All presented coherent electronic transport calculations in the tunneling regime are carried out using the Non-equilibrium Green's function (NEGF) formalism. The calculations are performed using a localized linear combination of atomic orbitals (LCAO) basis set (double-zeta plus polarization quality basis for all atomic species) as implemented in the Atomistix ToolKit (ATK) package [37] [25] [38]. The device region contains a central device region (C) that connects to two semi-infinite leads at fixed electronic chemical potential of the left and right electrodes μ_L, μ_R, respectively, see Figure 4.16. Electronic potential inside the leads in the device converges rapidly to their corresponding bulk values as a result of sets the boundary conditions and the electronic screening. Green's function (GF) of the central region defined by.

$$G(E) = \left[ES - H_C - \sum\nolimits_L (E) - \sum\nolimits_R (E)\right]^{-1} \tag{2.16}$$

where S and H_C are the overlap and Hamiltonian matrix of the central region in the LCAO basis. The self-energies $\Sigma_{R/L}$, include the open boundary conditions of the infinite bulk electrodes.
The transmission spectrum of the system is obtained from which current can be extracted after solving the self-consistent non-equilibrium density matrix in ATK.

The transmission coefficient at energy ε is obtained by summing up the transmission from all the states at this energy,

$$T(E) = \sum_k t_k^\dagger t_k^\dagger \delta(\varepsilon - \varepsilon_k) \tag{2.17}$$

where $t_k^\dagger$ is the transmission amplitude at the fraction of a scattering state k which propagates via a device.

Alternatively, the retarded Green's function can also yield the transmission coefficient as shown below

$$T(\varepsilon) = G(\varepsilon)\Gamma_L(\varepsilon)G(\varepsilon)^\dagger\Gamma_R(\varepsilon) \tag{2.18}$$

where $\Gamma_{L/R}(\varepsilon) = i(\Sigma_{R/L}(\varepsilon) - \Sigma_{R/L}(\varepsilon)^\dagger)$ and the trace is taken over the central region basis functions. In physical terms $T(\varepsilon)$ gives the transmission coefficient (probability) for an electron incident on the interface with an energy E under an applied bias V. Finally, the current per unit cell is obtained from the transmission coefficient using

$$I(V_L, V_R, T_L, T_R) = \int_{\mu_L}^{\mu_R} T_\sigma(E)\left[f\left(\frac{E-\mu_R}{K_B T_R}\right) - f\left(\frac{E-\mu_L}{K_B T_L}\right)\right] dE \quad (2.19)$$

where f is $T_{L/R}$ is the electron temperatures of left/right electrode, and $T_\sigma(E)$ is the transmission coefficient doe spin component σ.

The energy dependent conductance $G(E)$ is described as

$$G(E) = \frac{e^2}{h} T(E)$$

For an ideal system $G(E) = G_O$, where $G_0 = 2e^2/h$ which is the quantum unit of conductance and corresponds to a resistance of 12.9 kΩ.

The chemical potentials of the left and right electrodes relative to Fermi level of their respective electrode are defined as $\mu_L = E_F^L - eV_L$ and $\mu_R = E_F^R - eV_R$, respectively.
The applied bias voltage across the device region is obtained is defined as $\mu_R - \mu_L = eV_{bias}$; leads to $V_{bias} = V_L - V_R$.

2.6. Codes

All DFT calculations presented in this thesis have been performed by means of GPAW code and the NEGF calculations have been carried out using the ATK code. We present the main features of both codes in the following paragraphs.

GPAW [24][39] is a DFT package that uses a real space basis set calculated on a uniform grid algorithm. It is based on the projector-augmented wave (PAW) function method [40]. PAW method describes the non-valance electrons (core electrons) in a frozen core approximation since core electrons are localized around nuclei and are chemically inert. It is combined with the atomic simulation environment (ASE) [41] that can be used to setup and analyze atomistic simulations.

ATK refers to Atomistix ToolKit [25] [37] [38] simulation software for nanoscience. ATK is used in this thesis popular to obtain the electron transport calculations for atomic scale systems connected to semi-infinite electrodes with an applied bias. The tool is based on DFT, using numerical atomic orbital basis sets. The effects of core electrons are described by using nonlocal norm-conserving pseudopotentials. The NEGF formalism takes into accounts both the self-consistency and the solution of the electrostatic problem.

CHAPTER 3

Li-O_2 Batteries

3.1. Introduction

As use of renewable energy sources increases, the demand for high energy storage on various time scales is rapidly growing for a wide range of applications. For short time energy needs, batteries are preferable for instance to use as a backup in case of power fluctuations. Rechargeable batteries are used for electrification of vehicles in the transport services. Today, most electric and hybrid electric vehicles (HEV) rely on Li-ion batteries. The main drawbacks of Li-ion batteries are their high price per kWh of storage energy, slow charging and low energy/power density compared to that of gasoline. [42] In other words, the capacity offered by the state of the art Li-ion technology is too low to solve the increasing energy storage demands. The latest capacity of Li-ion batteries is ~300 mAh/g [16]. This technology probably will not be able to increase appreciably from the present capacity since it has almost reached its theoretical limitations.[42] The number of HEV and electric vehicles on the road are rapidly increasing globally. The latest affordable electric vehicles offer a limited driving range at a maximum of 120 miles. The luxury EV (Tesla S model) provides a driving range of up to 270 miles but it costs nearly ~100, 000 $. The need for development of safe, long-lived rechargeable batteries, with considerably higher energy density and specific energy which can provide the desired driving range at a reasonable price, is evident. [18]

Recently, technologies “beyond Li-ion batteries”, such as metal-air batteries, have gained great interest as a future alternative to Li-ion batteries in the transportation sector. Particularly, the Li-O_2 couple appears as a promising choice due to its superior energy storing capacity of all beyond Li-ion batteries. The rechargeable Li-O_2 battery using aprotic solvent, where Li_2O_2 is formed during discharge at the cathode, was initially reported by Abraham *et al*. in 1996. [43] The development of Li-O_2 /Air batteries is making progress; however, to produce commercial working batteries substantial improvements are still needed. In the following section some pros and cons associated with this technology will be discussed.

3.1.1. Pros and Cons of Non-Aqueous Li-O_2 Batteries

As mentioned earlier, the Li-O_2 battery is a potential breakthrough in battery technologies in general as it has the highest achievable specific capacity ~3842 mAh/g [15]. This is about ~5-10 times greater than currently available Li-ion batteries, and it could probably offer the desired driving range (> 300 miles per charge), see Figure 1.3. Unlike Li intercalation in graphite in Li-ion batteries, the Li-O_2 technology if succeed may use the lightest metal, lithium directly in pure form as anode. The other reaction component is oxygen gas (O_2), which is taken from ambient atmosphere using some sort of purifying membrane.

There are many fundamental and technical challenges linked with this emerging technology. Unlike the Li-ion batteries, the metal air batteries in general and Li-O_2 in particular suffer from complex parasitic side reactions. Limited electric efficiency is caused by overpotential/polarization losses at the cathode in both discharge and charge processes. Less than 70 % electrical efficiency is attained due to typically observe high overpotential (> 1.0 V) during charging process. Moreover, the limited power and current densities currently achievable are main challenges. In order to solve these cons mentioned above it is crucial to gain a fundamental understanding of the reaction mechanisms of charge/discharge processes. Moreover, charge transport studies in the reaction products for example in Li_2O_2 and other side products such as Li_2CO_3 and various cathode-electrolyte interfaces like Li_2O_2@LI_2CO_3 are equally important.

In general, the Li-O_2 chemistry is complex and this makes the charge transport mechanisms more challenging. Moreover, complex interfacial phenomena, influences of air impurities, the two electrodes stability, choice of appropriate electrolytes and safety are among critical issues that need to be addressed in non-aqueous rechargeable Li-O_2 battery research. [44][45]

According to G_oW_o calculations Li_2O_2 is an insulator material with a bandgap of 4.9 eV.[46][47] This material deposits at the cathode surface during discharge and significantly limits the electronic conduction from the cathode electrode to the active site where the discharge reaction is taking place. Thus, 5−10 nm thick Li_2O_2 film deposits lead to so called “sudden death” during discharge. [48-50] An electron transport mechanism alternative to tunneling is required, to obtain enhanced conductivity. DFT+U studies by Garcia-Lastra *et al*. [51] revealed a hole polaronic conduction as an alternative conduction mechanism in Li_2O_2. Moreover, HSE functional studies also found hole and electron polaronic hops as the preferable conduction mechanism in Li_2O_2. They also found that the hole polarons have higher mobility, *i.e*. low energy barrier compared to the electron polarons hops. Furthermore, Luntz *et al*, have shown that polaronic transport is more important in Li_2O_2 at

elevated temperatures and at low current densities.[52][53] In addition to coherent transports through tunneling and polaronic conduction mechanism, there are also other possible charge transport mechanisms under investigation such as adding dopants [54] [55] and surface conductance [56] among others.

3.1.2. Li-O_2 /Air Battery Working Principle

The basic design of a Li-O_2 cell is similar to any other conventional electrochemical cell as it contains two electrodes and an electrolyte. Namely, the lithium metal anode (-) and the air cathode (+) where oxygen gas (O_2) is taken from air or tank and diffuse on the surface of a porous carbon, and the non-aqueous electrolyte in between the two electrodes as shown in Figure 3.1.

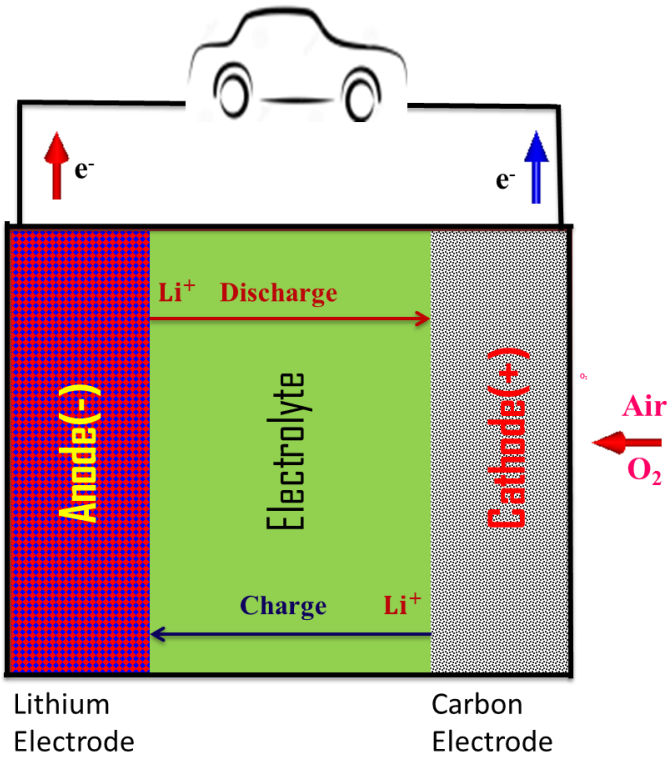

Figure 3.1: Schematic of Li-O_2 battery.

During the discharge process, a Li^+ ion is released from the anode and moves to the cathode through the electrolyte. In the charging process Li^+ ion is reduced to metallic lithium (Li^o) and deposited back to the lithium electrode. The two processes occur at different chemical potentials and the difference of the two chemical potentials defines the open circuit voltage (OCV) as shown below.

$$\mathrm{OCV} = \frac{\Delta G^{\theta}}{zF} \tag{3.1}$$

where ΔG^{θ} is the change in Gibbs free energy of the reaction, F is the Faraday constant and z is the charge number which is 1 for systems that use lithium.

During discharge process, the electrons will move through an external circuit, whereas, the lithium ion moves through the electrolyte. In both cases the move is from anode (-) to cathode (+) during discharge. The electrolytes are supposed to be ionic conductors but not electron conductors. The amount of energy transferred to electric devices is equivalent to the OCV multiplied by z, the charge number.

The ORR and OER mechanisms, and species formed during operation in Li-O_2 batteries are dependent on the electrolyte selection, whether it is aqueous, non-aqueous (aprotic) or solid. In a rechargeable Li-O_2 battery that uses aprotic solvents Li_2O_2 is formed during discharge at the cathode with lithium superoxide (LiO_2) as an intermediate product (equation 3.3). The proposed electrochemical reaction mechanisms at the electrode following series of reports from McCloskey *et al*. [57], Abraham *et al*. [58] and Bruce *et al*. [59], and many other reports are given by:

Anode reaction: $$2\mathrm{Li} \rightarrow 2(\mathrm{Li}^+ + \mathrm{e}^-) \tag{3.2}$$

Cathode reactions: $$\mathrm{Li}^+ + \mathrm{e}^- + {\mathrm{O}_2}^* \leftrightarrow {\mathrm{LiO}_2}^* \tag{3.3}$$

$$ {\mathrm{LiO}_2}^* + \mathrm{Li}^+ + \mathrm{e}^- \leftrightarrow {\mathrm{Li}_2\mathrm{O}_2}^* \tag{3.4}$$

$$ {\mathrm{LiO}_2}^* + {\mathrm{LiO}_2}^* \leftrightarrow {\mathrm{Li}_2\mathrm{O}_2}^* + \mathrm{O}_2 \tag{3.5}$$

In an ideal rechargeable Li-O_2 system, two electrons are consumed (evolved) per oxygen molecule in the discharge (charge) process, assuming that only oxygen gas is consumed or evolved, and no other side reaction products are formed due to electrolyte decomposition, air impurities or degradation. However, in reality there are a number of side reactions that could occur and result in formation of several species such as carbonates and hydroxides.

3.2. Electronic Properties of Li_2O_2

3.2.1. Bulk Phases of Li and Li_2O_2 Crystal Structures

Cota and Mora [60] reported that lithium peroxide (Li_2O_2) crystalizes with hexagonal crystal structure that belongs to the *P6₃/mmc* space group with the experimental lattice parameters of a = b = 3.187 Å, c = 7.726 Å [60]. It can effectively be viewed as individual peroxide O_2^{-2} ions embedded in sea of Li^+ ions, as shown in Figure 3.2.

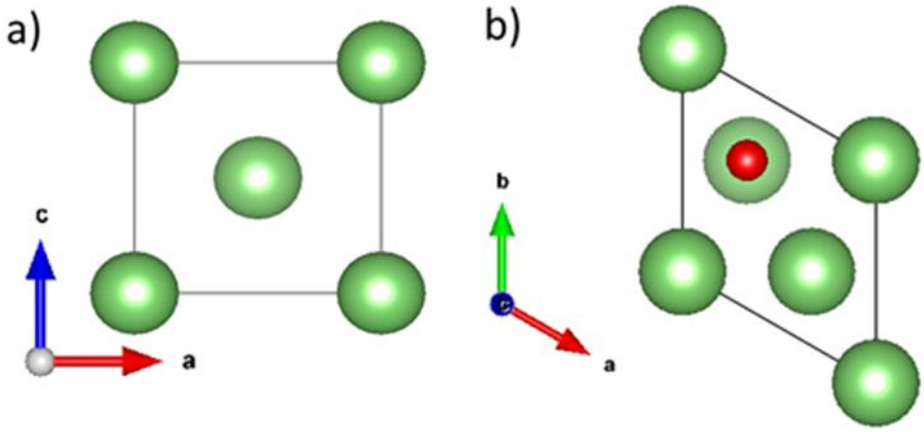

Figure 3.2: a) Body-centered cubic (BCC) Lithium structure with lattice a = 3.48 Å at room temperature. b) Hexagonal Li_2O_2 unit cell structure (top view) with lattice parameters a = b = 3.187 Å, c = 7.726 Å (space group P63/*mmc*). Color: Lithium (green) and oxygen (red).

The metallic lithium crystallizes in the body-centered cubic (BCC) structure at ambient temperature and pressure. [61][62] The cubic unit cell contains two lithium atoms and half of the total energy of the unit cell which corresponds to the single metallic lithium atom has been used to calculate the formation energies of lithium containing species.

3.2.2. Density of States (DOS)

The states close to Fermi level of bulk Li_2O_2 originate from peroxide ions (O_2^{-2}), not Li^+ ions. Hence, DOS revealed that both the highest occupied molecular orbital (HOMO) and the lower unoccupied molecular orbital (LUMO) are almost entirely arising from the 2p orbitals of the peroxide ions (O_2^{-2}). In Figure 3.3, we can see that Li_2O_2 is a wide bandgap insulator with a DFT + U (at U = 6 eV) calculated bandgap of 5.03 eV. The DOS of a defect system with a Li^+ vacancy reveals that the vacancy levels pin the Fermi level.

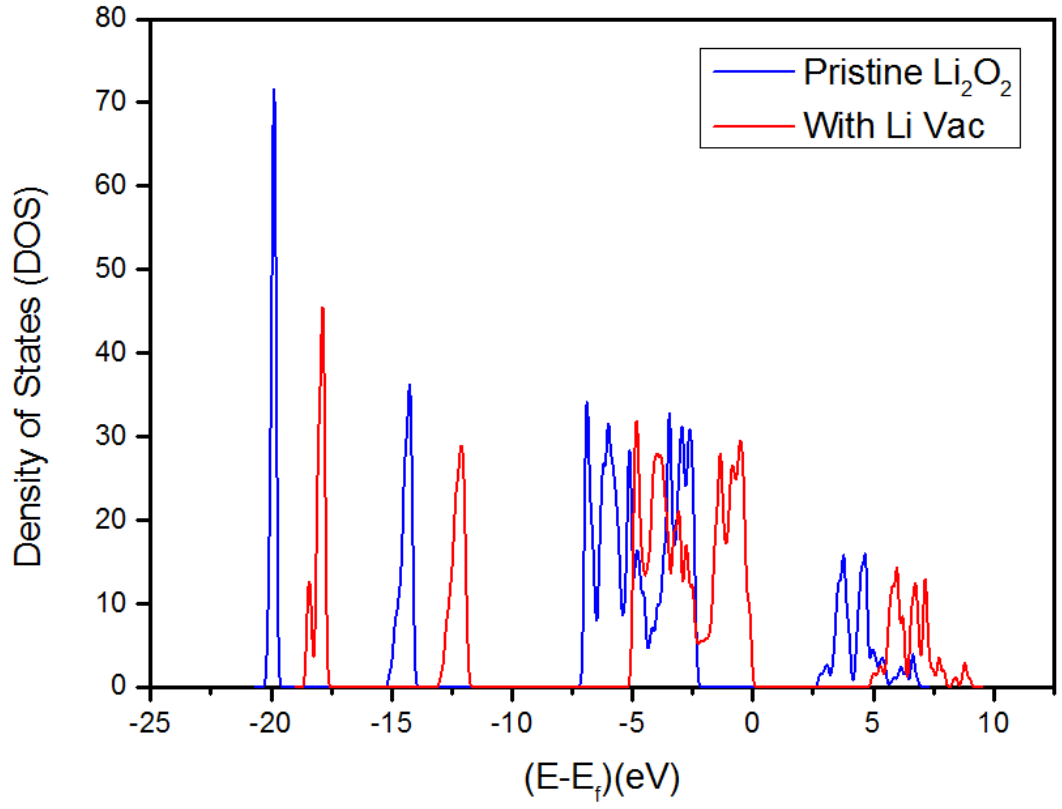

Figure 3.3: The total density of states (DOS) relative to the Fermi energy for pristine Li_2O_2 and with defect (neutral Li-vacancy) using RPBE + U (at U = 6 eV)

3.2.3. Stable Surfaces of Li_2O_2

In several computational studies it has been reported that reconstructed (0001), $(1\bar{1}00)$ and $(11\bar{2}0)$ surfaces are the most stable and predominantly exposed facets at battery operating potentials, being about 80% dominated by the (0001) surface. [63][64] Moreover, related works by Radin *et al*. [56][63] have shown that facets such as (0001), $(1\bar{1}00)$ and $(11\bar{2}0)$ have similar surface energies and Hummelshøj *et al*.[64], have also shown that surface energies are potential dependent and varies during discharge and charge. At lower current densities surface kinks and steps will control the growth of Li_2O_2. In chapter 4 we will present the effect of CO_2 poisoning on a stepped $(1\bar{1}00)$ Li_2O_2 surface.

A previous theoretical work by Hummelshøj *et al*. [65] reported that steps on a reconstructed $(1\bar{1}00)$ surface could act as nucleation sites at low discharge overpotentials. The oxygen rich (0001) facet will also be exposed, in particular under charging conditions. The role of steps and kinks on the different (0001) terminations is, however, less investigated than on the $(1\bar{1}00)$ surfaces as overpotentials on (0001) are expected to be slightly higher. [64] Apart from own CO_2 poisoning effect studies on the reaction mechanisms on the $(1\bar{1}00)$ Li_2O_2 surface [66], recent computational DFT results for SO_2 adsorption on stepped (0001) and $(1\bar{1}00)$ surfaces does, show preferential bonding to the highly investigated $(1\bar{1}00)$ facet. [67]

3.3. Ionic Conductivity in Li_2O_2

The lithium diffusion studies are modelled using a vacancy mediated approach in which a single Li atom is removed from the $3 \times 3 \times 1$ Li_2O_2 supercell (consists of 72 atoms) and yields a total vacancy concentration [V^0_{Li}] of 2.78 %. Thus, the activation energy of the lithium or vacancy (in the reverse direction) diffusion along the path between relaxed initial and final states is estimated using CI-NEB method as it is described in section (2.4). Revised Perdew-Burke-Ernzehof (RPBE) exchange correlation functional is used in all Li_2O_2 calculations [28]. All ground state energies are determined when Hellmann-Feynman forces were less than 0.03 eV/Å. Atoms in the super cell are free to relax during the optimization. The calculations are performed both at the neutral and -1 compensating back ground charge.

We have conducted six different Li diffusion channels along the three directions within two layers, two diffusion pathways are considered in each direction. These six hops are performed twice using 0 and -1 compensating background charges. Accordingly, four hops in the intralayer direction (in the XY-plane, see Figure 3.4) are considered, namely BE(X) and AD(X) in the X directions and AF(Y) and BG(Y) in the Y directions. In both cases the energy barriers are close to 1 eV. Interestingly, we observe that the hops in the X and Y directions within the same intralayer are overlapping, as can be seen in Figure 3.4. Regarding the interlayer diffusion (in Z direction), there are two possible inequivalent hops, namely AB(Z) and BC(Z).

The estimated barrier at neutral background charge is $E_b = 0.44\ \mathrm{eV}$ and $E_b = 0.36\ \mathrm{eV}$ for the AB(Z) hop and BC(Z) hop, respectively, giving an average $E_b = 0.40\ \mathrm{eV}$. Thus it is clear that V^0_{Li} diffusion has a preferential channel in the Z-direction. The microscopic diffusion channel follows $\mathrm{A} \rightarrow \mathrm{B} \rightarrow \mathrm{C}$ series along the Z-direction with an average rate of $r = 2x10^6 s^{-1}$ and a diffusion coefficient of $\mathrm{D} = 1.5x10^{-9}\ \mathrm{cm}^2/\mathrm{s}$. This relatively small barrier in the Z direction opens the possibility for both V^0_{Li} V^-_{Li} diffusion at ambient conditions (for more details see ref. [68][69]). The results obtained using -1 compensating background charge (charged vacancies), are nearly identical, see Figure 3.4.

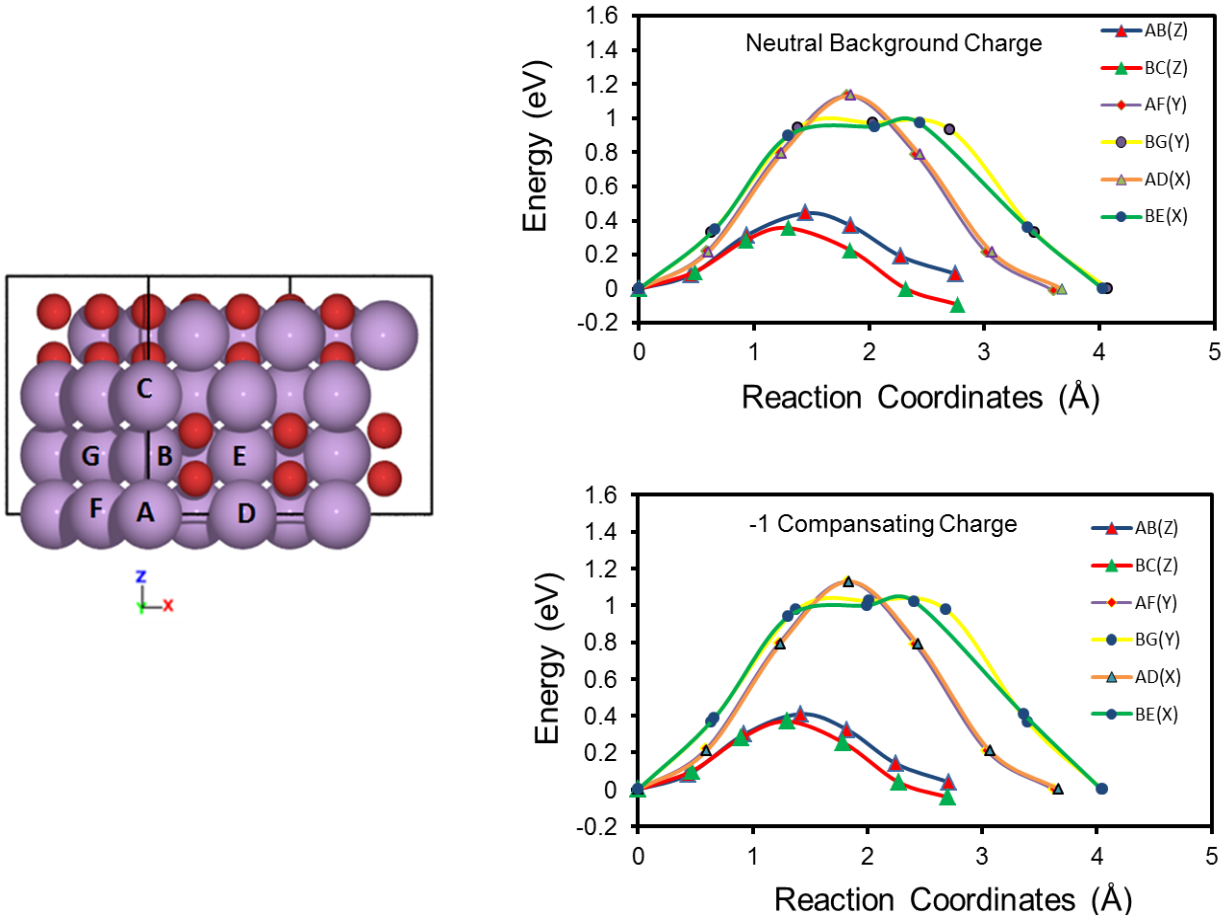

Figure 3.4: The calculated CI-NEB pathways for Li_2O_2 bulk of $3 \times 3 \times 1$ supercell. The migration barriers for the neutral Li-vacancies, V_{Li}^{o}, (upper) and charged Li-vacancies, V_{Li}^{-}, with -1 compensating background charge (lower) in both intralayer and interlayer diffusion channels are almost similar.

3.4. Coherent Transport in Li_2O_2

The coherent electronic transport calculations in Li_2O_2 in the tunneling regime are carried out using the Nonequilibrium Green's function (NEGF) formalism. The calculations are performed using a localized linear combination of atomic orbitals (LCAO) basis set (double-zeta plus polarization quality basis for all atomic species) as implemented in the Atomistix ToolKit (ATK) [37] [25] [38] package, where a central device region (or scattering region) is connected to two semi-infinite leads, which are kept at fixed electronic chemical potentials, μ_L and μ_R, respectively, to simulate an applied bias voltage across the device region given by $V = (\mu_L - \mu_R)/e$. The scattering region contains 16 formula units of Li_2O_2. The semi-infinite leads contain similar species, *i.e.* 8 formula

units of bulk Li_2O_2 as left and right electrodes. The RPBE exchange correlation functional and a $4 \times 6 \times 100$ k-point sampling is used during the NEGF self-consistent loop. In the finite bias calculations, a positive bias is defined as sending electrons from left to right.

It is expected that in the Li_2O_2 structure for bias voltages (negative or positive) around 2.0−2.5 eV (*i.e*. half of the bandgap of Li_2O_2) we will start to see a relative good conductance in Li_2O_2 bulk, see Figure 3.5.

Regarding the presence of vacancies in Li_2O_2 bulk, as shown in Figure 3.3 the DOS of the defect system reveals that the vacancy levels pin the Fermi level of the pristine system. This implies that V_{Li}^{o} vacancies are not going to open new electron tunneling channels in these systems and they are going to have a detrimental effect in the conductivity due to their action as scattering centers.

In order to check the plausibility of these assumptions we perform DFT−NEGF calculations as described in section 2.4. As seen in Figure 3.5 significant current (around ~10 $\mathrm{mA/cm^2}$) begins to rise just around $\pm\, 2.0\,\mathrm{V}$ in pristine Li_2O_2 bulk. Furthermore, V_{Li}^{o} vacancies reduce the current at relevant voltages, by a factor of 2. The V_{Li}^{o} vacancies in Li_2O_2 have a substantial negative effect, on the coherent electronic transport at the oxygen electrode of Li-O_2 batteries.

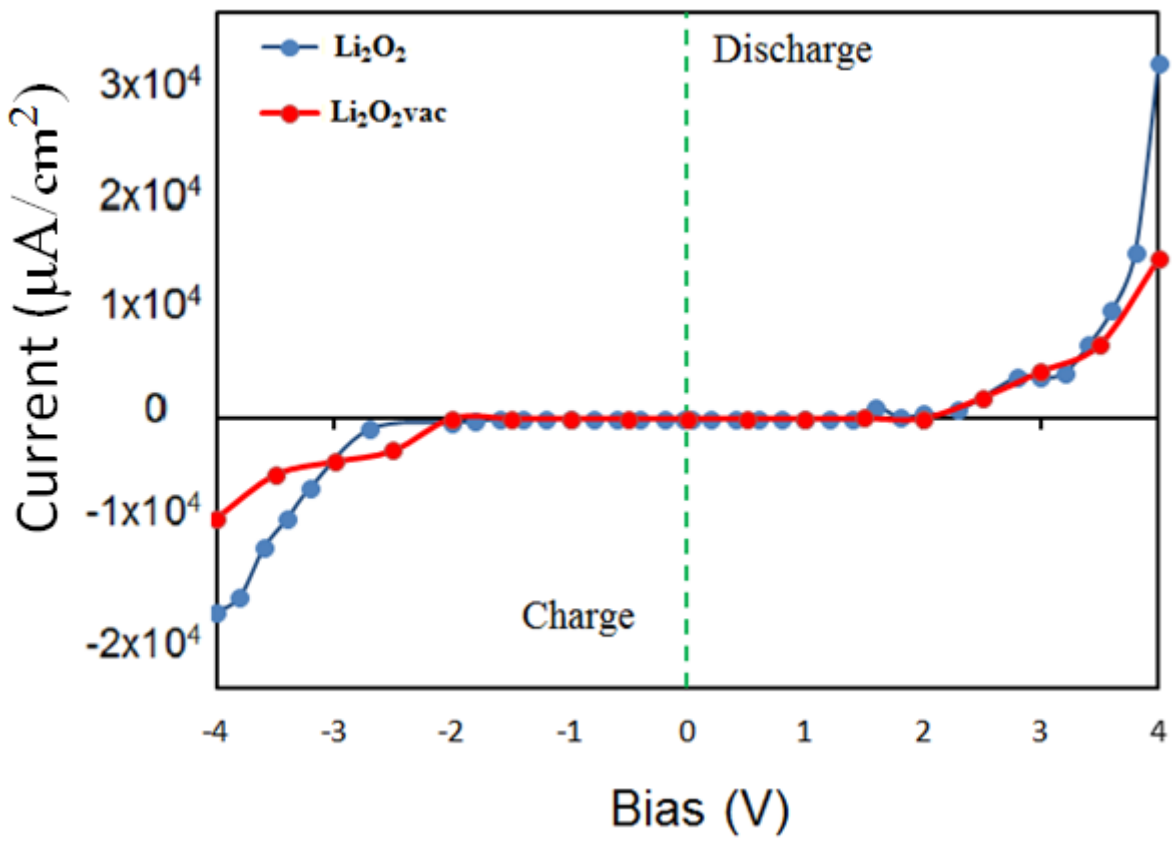

Figure 3.5: Calculated IV curves from ATK using the RPBE exchange correlation functional with k-point sampling $4 \times 6 \times 100$ at electron temperature of 300 K for pristine Li_2O_2 and in the presence of a neutral lithium vacancy.

3.5. Polaronic Conductivity in Li_2O_2

The polaron hops in Li_2O_2 will be discussed in this subsection. Polaronic conduction studies in Li_2O_2 have been performed using the DFT+ U method. It includes hole and electron polaron hops in both intra and interlayer paths. We found that Li_2O_2 bulk can hold hole polarons with sufficiently low migration barriers 0.53 eV (0.14 eV difference from [51] due to supercell size difference) and become an alternative path for electron transport.[51] It has been also found that the material can hold excess electron polarons. However, the migration barriers for electron polarons are much higher than the ones for hole polarons, *i.e.* 1.49 eV. When we consider polaron localization we observe that the hole (excess electron) polaron is localized by shortening (stretching) the bond length of one of the O−O bond from 1.55 to 1.33 Å (2.45 Å), see Figure 3.6. Apart from the geometry distortions we observe in all the cases the appearance of a magnetic moment in the oxyanions, which is another footprint of the hole (excess electron) localization. The localized states are more stable than the delocalized ones (charge dispersed in the crystal) and particularly the electron polaron is found to be strongly localized by > 2.0 eV relative to the delocalized state [51].

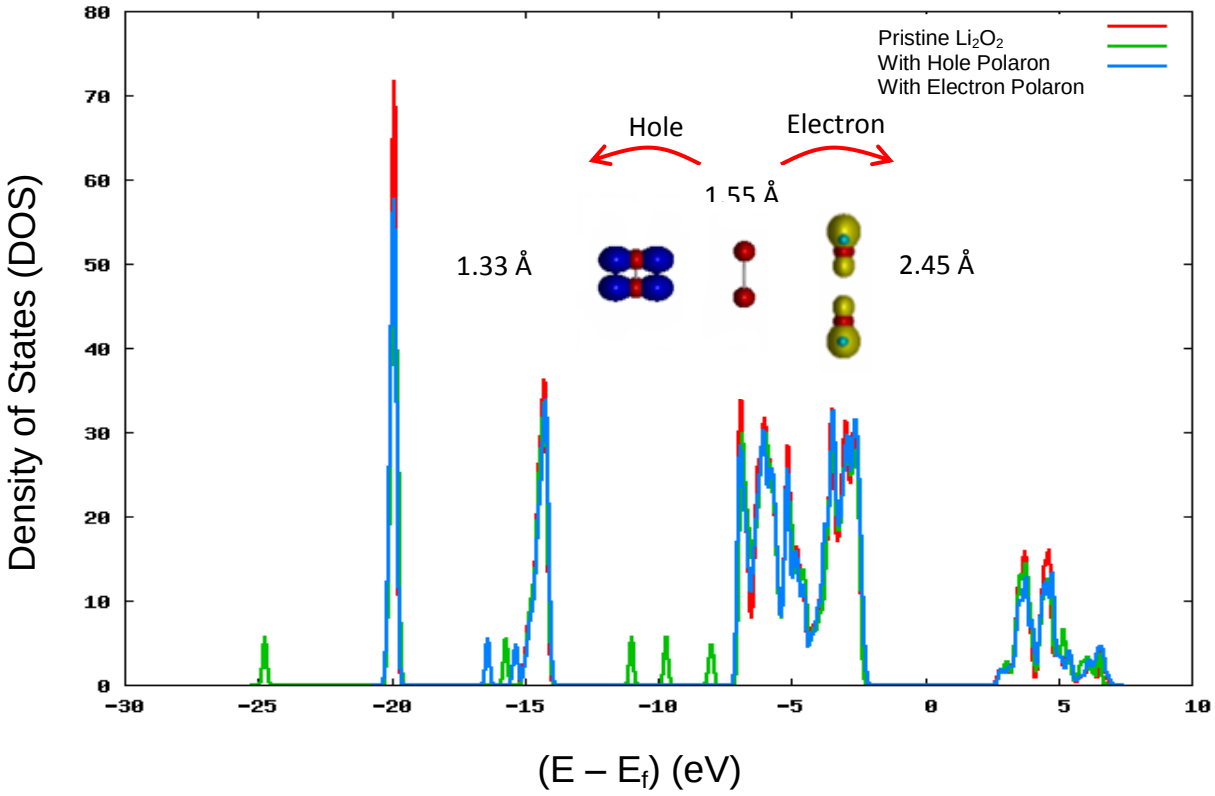

Figure 3.6: DOS of the pristine Li_2O_2 compared with a localized hole and electron polarons on one peroxide anion using DFT+U (at U = 6 eV).

Polaron localization results in some sort of distortion in the peroxide crystal structure of Li_2O_2, *i.e*. a hole localized in a peroxide ion involves a change in the O−O bonding distance of 0.2 Å, while the localization of an excess electron requires stretching the bonding by 0.9 Å. As shown in Figure 3. 7, the barrier for transporting excess electron polarons is 1.41 eV in Li_2O_2 bulk. This implies that the excess electron polaronic transport across Li_2O_2 is an inaccessible channel for electronic transport. The polaron hopping barrier for holes in Li_2O_2 bulk is 0.39 eV.

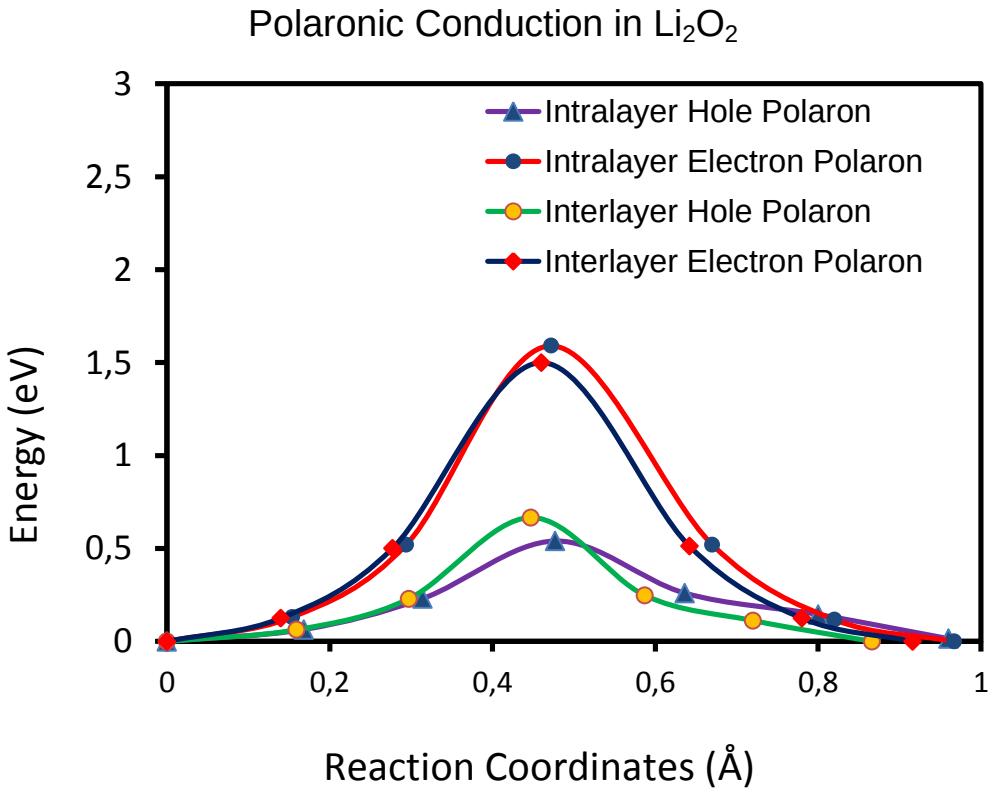

Figure 3.7: Calculated polaron hops in a $3 \times 3 \times 1$ Li_2O_2 supercell along the intralayer and interlayer channels. Energies are obtained from RPBE+U (at U = 6 eV) method.

CHAPTER 4

Li–O_2 / CO_2 Battery

4.1. Introduction

In this chapter we extend the discussions to real Li–O_2 /Air battery technology, it is anticipated to make use of ambient air as an oxygen source using a purification technique. However, few experimental results that have been obtained in ambient conditions have already revealed that, air impurity is one of the main bottlenecks to the development of the Li-O_2 /Air battery technology. At ambient conditions the atmosphere contains an average of ~0.04 % (400 ppm) of carbon dioxide and 1.5–4 % of water vapor, for example at 25 ^{o}C and 50 % humidity the concentration of H_2O in air is ~1.5 %. In fact, these values might vary with location and season.

Currently, almost all the Li–O_2 /Air battery studies are carried out using either pure oxygen gas at 1 atm or in ambient conditions with an oxygen partial pressure of 0.21 atm. For example, Li–O_2 /Air batteries using Ketjenblack carbon-based air electrodes can last for more than a month in ambient conditions offering a specific energy of 362 Whkg^{-1}, considering the entire weight of the battery packaging [70]. In order to fully remove or reduce the amount of water contamination for the battery to operate in ambient air conditions, many types of O_2-permeating membranes have been tested. A hydrophobic-type inorganic material silicalite zeolite and a polymeric material poly(tetrafluoroethylene) (PTFE) membrane were tested and results concluded that the PTFE film supported on a spongy metal sheet offer the highest battery efficiency [71].

In this chapter we will discuss the influence of CO_2 poisoning on both overpotentials and discharge capacities as it appears in paper II. We have combined the DFT calculations with experimental techniques such as galvanostatic and differential electrochemical mass spectrometry (DEMS) measurements. The results revealed that even small amounts of carbon dioxide contamination (< 1 % CO_2) in the feed oxygen gas substantially increase the charging overpotential, which reduce the efficiency of the Li–O_2 /Air battery at large [72][73]. Water vapor contaminations also results in similar efficiency losses. Moreover, in an aqueous $\mathrm{Li-Air}$ battery

the bottleneck issue is the corrosion of the metallic Li anode. The last but not the least is the safety part, hence, the Li foil is explosively reactive with water.[74]

Apart from the air impurities, as much attention is given to the stability of aprotic electrolytes and carbon cathode materials that both play a significant role in limiting the performance of the battery. Many reports give emphasis to the formation of a carbonate species (Li_nCO_3) from parasitic side reactions between Li_2O_2 or LiO_2 and carbon sources such as CO and CO_2 molecules from the atmosphere [72], reactive carbon from the graphite cathode or carbonate derivatives from decomposition of the aprotic electrolytes.

4.2. Carbonate Formation: Cathode and Electrolyte Stability

It has been reported in many publications that various electrolytes decompose by possible intermediates and discharge products such as Li_2O_2 and LiO_2 and e.t.c. In other words the discharge products react either chemically or electrochemically with electrolytes. [15][75] [76]

Younesi, *et al.*, [77][78] reported the degradation of various electrolytes by Li_2O_2 and documented Li_2CO_3 as a decomposition product from aprotic electrolytes. Likewise, McCloskey *et al.,* [50] have shown that small amounts of carbonates that accumulate at the C-Li_2O_2 and Li_2O_2-electrolyte interfaces are responsible for a large potential increase during recharge and a huge decrease in exchange current density. Other various studies on the stability of nonaqueous electrolyte have also been reported. [79-84]

All presented experimental work were performed using a known aprotic electrolyte 1, 2-dimethoxymethane, DME, that contain about 20 ppm of H_2O impurity in 1M lithium bis(trifluoromethylsulfonly)imide salt abbreviated as LiTFSI (99.95 % purity), P50 AvCarb carbon paper cathode and a lithium anode. Both of them are dried for several days at different temperatures prior to mixing. They are purchased from Sigma Aldrich. The choice of the electrolyte, DME, is based on its relative stability compared to other nonaqueous electrolytes studied in the Li-O_2 /Air battery studies. The experimental measurements have been conducted at DTU Energy by Kristian and Jonathan.

4.2.1. Ionic Conduction in Lithium Carbonate **Li_2CO_3**

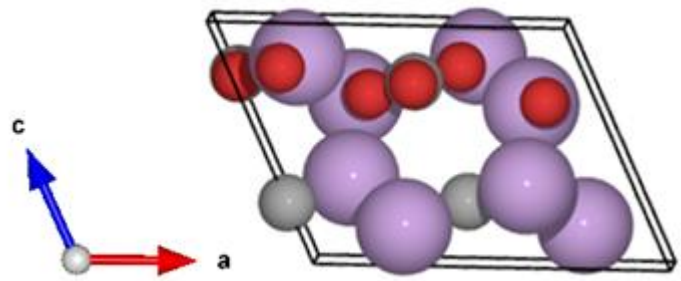

Figure 4.1: The monoclinic Li_2CO_3 crystal structure with space group 15 or *C* 2/*c* consists of 4 formula units per unit cell with lattice parameters a = 8.359 Å, b = 4.973 Å, c = 6.197 Å and β = 114.83°.[115] The planar CO_3^{-2} groups with C-O bond lengths of 1.284, 1.305 and 1.305 Å are surrounded by the sea of Li^+ ions. The Li^+ and CO_3^{-2} groups are oriented alternating on the XY plane. Each Li^+ ion is coordinated with four oxygens to form a tetrahedral structure. Color: Red (Oxygen), Gray (Carbon) and Purple (Lithium).

In this subsection, the details of the Li vacancy diffusion in bulk Li_2CO_3 across various pathways are discussed, see Figure 4.1. Lithium vacancies, V^0_{Li}, diffusion studies are modeled by removing a single Li atom from a supercell followed by internal relaxation. We employ a $2 \times 2 \times 2$ supercell (192 atoms) of bulk Li_2CO_3 with a $1 \times 2 \times 2$ k-point sampling to analyze the effect of neutral and negatively charged vacancies (V^{-1}_{Li}). The total vacancy concentration is found to be 1.6 %.

We have conducted a diffusion studies in five different possible diffusion paths in Li_2CO_3, (see Figure 4.2). As shown in Figure 4.2, the CI-NEB calculations show several minimum energy barriers for the different Li vacancy diffusion channels, *i.e* ~0.2 eV in all the three directions for both neutral and charged Li vacancies. We found that the AD diffusion path is the most plausible low energy barrier channel in the Y direction, while the CE diffusion path is most favorable in the Z direction. For the X direction Li follows a sequence of diffusion paths. For instance, the microscopic diffusion channel along the X direction probably follow AB diffusion path as a first step then followed by BC or AD diffusion path or vice versa ($\mathrm{AD} = \mathrm{BC}$). The average rate (*r*) of Li vacancy diffusion and diffusion coefficient (D) of Li_2CO_3 is estimated using equation (2.15). The corresponding values are equal to $9x10^8 s^{-1}$ and $1.6x10^{-6}\ \mathrm{cm}^2/\mathrm{s}$, respectively.

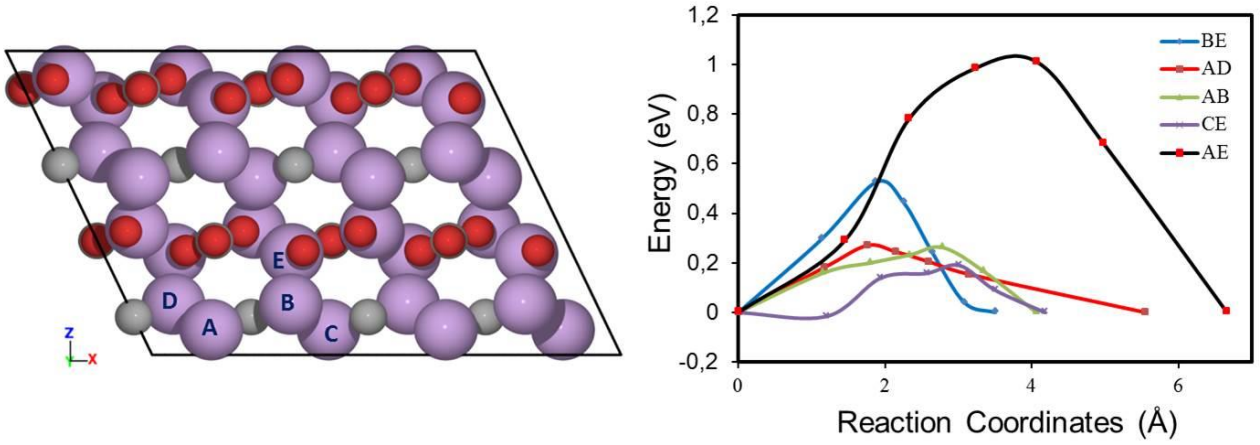

Figure 4.2: Calculated CI-NEB paths for Li vacancy (V^{0}_{Li}) diffusion in bulk Li_2CO_3 along different channels. A minimum energy barrier is obtained about 0.20 eV. Color: Purple (Lithium), Red (Oxygen), Grey (Carbon).

4.3. Air Impurities at the Air Cathode: CO_2 Poisoning

In this subsection, we address the influence of CO_2 contamination on Li_2O_2 growth mechanism, discharge/charge overpotentials and capacity in nonaqueous Li-air batteries using computational tool (DFT) and experimental techniques such as galvanostatic and differential electrochemical mass spectrometer (DEMS) measurements. [66] Among other air contaminants, CO_2 is the most critical subject due to its high solubility in aprotic electrolytes and high reactivity with Li_2O_2 to form an insulating material which oxidizes at higher overpotential, *i.e*. Li_2CO_3. [85][50]

4.3.1. Galvanostatic Dis/charge Results with and without CO_2 Impurity

To investigate the effect of gaseous CO_2, the assembled cells were purged with three different atmospheres: 0/100 CO_2/O_2, 1/99 CO_2/O_2, and 50/50 CO_2/O_2. Three individual batteries were assembled and investigated for each atmosphere and the corresponding results are presented in Figures 4.3 and 4.4. An average data of the three cells is therefore taken at the same atmosphere. The lowest discharge capacity was observed for the 50 % CO_2 cells (blue line in Figure 4.3) and is most likely caused by the high concentration of electrochemically inactive CO_2. A similar effect was observed, by Gowda *et al*. [72] for a pure CO_2 cell, where the cell potential immediately dropped. It should however be noted that Takechi *et al*. [86] observed, quite to the contrary of our

observations, higher discharge capacities up to 70 % CO_2 with respect to pure O_2 cells. Interestingly, a higher discharge capacity was observed for the 1 % CO_2 cells in respect to the pure O_2 cells as can be seen in Figure 4.3 (inset). A possible explanation is the dissolution of Li_2CO_3 species in DME and/or, as also suggested by Gowda *et al*., a change in deposition morphology compared to that deposited in the pure O_2 cells as suggested by Myrdal and Vegge.[67] Such morphological changes could increase the total electrodeposited layer and lead to higher capacities.

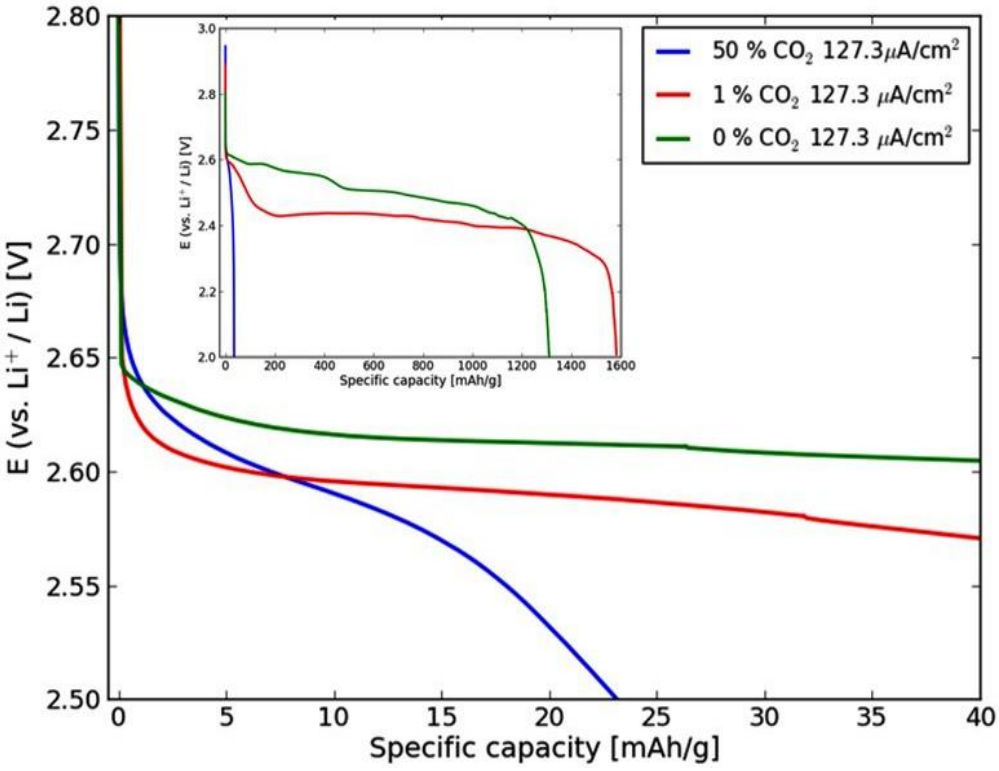

Figure 4.3: Galvanostatic discharge profiles at a current density of 127.3 $\mu A/cm^2$ at three different atmospheres: 50 % CO_2, 1 % CO_2 and 0 % CO_2. Inset shows the increase in discharge capacity in 1 % CO_2.

All CO_2 cells have higher discharge overpotentials compared to cells with pure O_2 at a discharge rate of 127.3 $\mu A/cm^2$, which may be caused by the blocking of the active nucleation sites by solubilized CO_2, forcing the reactions to follow pathways with higher overpotentials. This effect can even be seen at 1 % CO_2, as illustrated on Figure 4.3 above. The charge capacity is very dependent on the CO_2 concentration, with high concentrations limiting charge capacity and thereby cell reversibly, see Figure 4.4.

50 % CO_2 cells reach the lower potential limit (2.0 V) early, at approx. 35 mAh/g, while 1 % CO_2 cells and pure CO_2 cells continue until capacities in the range 1150-1600 mAh/g were reached

depending on current density. The low charge capacity at high CO_2 contaminations should be attributed to the poor Li-CO_2 electrochemistry, also reported by Gowda *et al*. The charging overpotentials are a function of both current density and the level of CO_2 contamination, while there is no significant difference in overpotentials between cells charged at 127.3 and 63.6 $\mu A/cm^2$ for 50 % CO_2 cells, which again can be attributed to the poor Li-CO_2 electrochemistry. At 127.3 $\mu A/cm^2$, there is an increase in overpotential of about 0.43 V and 0.34 V for 1 % CO_2 cells and 0 % CO_2 cells, respectively. The general increase in overpotentials with increasing current density can be explained by the Butler-Volmer model [87], while the larger overpotential for the 1 % CO_2 cells than 0 % CO_2 cells, is expectedly caused by the formation and oxidation of the carbonate like species (Figure 4.8b). A second charge at 63.6 $\mu A/cm^2$ shows identical results for 1 % and 0 % CO_2. This can be ascribed to the evolution of CO_2 observed during the initial charge cycle, where CO_2 is released at 4.5 V, as shown in Figure 4.5, resulting in residual CO_2 in the electrolyte causing blocking of the step sites in subsequent charging experiments.

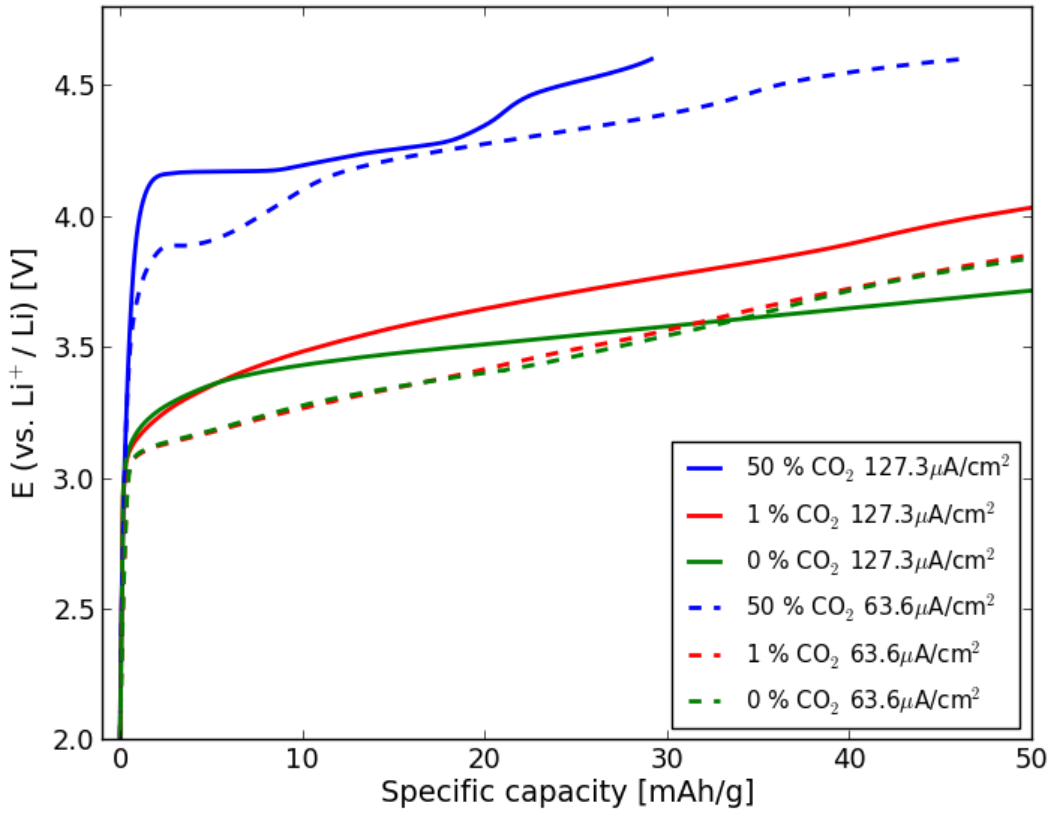

Figure 4.4: Galvanostatic charge profiles at 127.3 (solid) and 63.6 (dotted) $\mu A/cm^2$ at three different atmospheres: 50 % CO_2, 1 % CO_2 and 0 % CO_2.

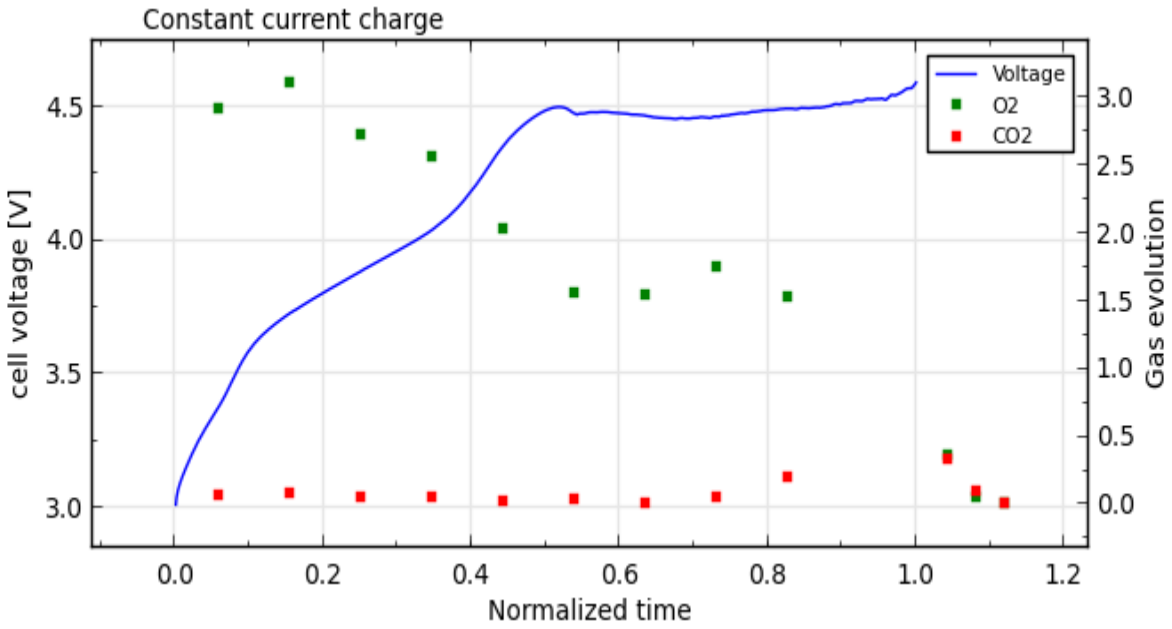

Figure 4.5: Evolution of O_2 and CO_2 as a function of time during a constant current charge following a constant current discharge to 2.0 V. The current of both charge and discharge was 100 $\mu A/cm^2$. The tested cell configuration is Li|DME+1M LiTFSI|P50 carbon paper. The measurement is performed with a differential electrochemical mass spectrometer (DEMS) at DTU Energy by Jonathan.

4.3.2. Gibbs Free Energy Diagram

The computational lithium electrode approach is used in the free energy calculations.[65] Defined as, U = 0, when bulk Li anode and Li ions in solution ($Li^+ + e^-$) are at equilibrium. The free energy change of the reaction is shifted by –neU at an applied bias, U, where n is the number of electrons coming from solution. The ground state energy of O_2 is calculated from the water reference ($E(O_2) = 2E_{DFT}(H_2O) - 2E_{DFT}(H_2) - 2E_{exp}(H_2O)$) unless stated since DFT does not describe the triplet ground state of O_2 correctly.[88] The entropy (-TΔS at STP) used for O_2 and CO_2 in the gas phase are -0.63 and -0.64 eV [89], respectively, while the entropy for solid phases (bulk Li and Li_2O_2) are assumed to be zero when estimating the free energy in Figure 4.9.

4.3.3. CO_2 Adsorption Energies at Various Sites on Stepped $(1\bar{1}00)$ Surface

The stepped $(1\bar{1}00)$ Li_2O_2 surface is modeled as shown in Figure 4.6.

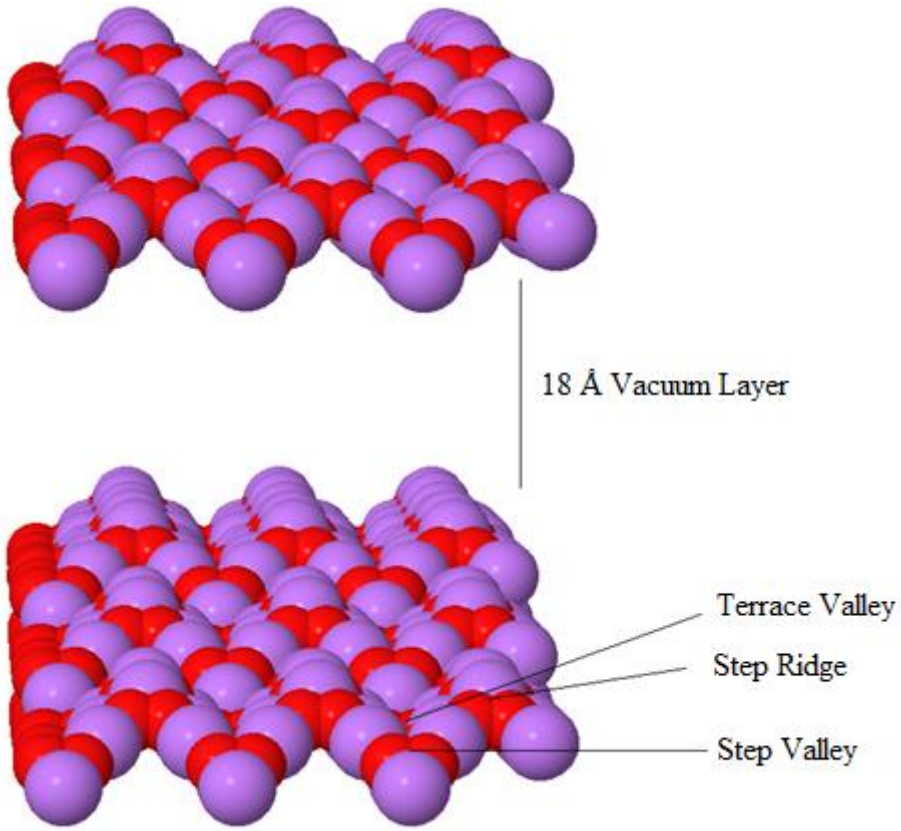

Figure 4.6: The stepped $(1\bar{1}00)$ Li_2O_2 surface with $3 \times 3 \times 2$ super cell consisting of a 56-64 atoms slab with a 18 Å vacuum layer between periodic images along the Z-axis.

Adsorption energies of CO_2 at various nucleation sites such as step and terrace of valley and step of ridge on a stepped $(1\bar{1}00)$ Li_2O_2 surface were determined; see Table 4.1. CO_2 binds preferentially at the step valley site and binds weakly at the step ridge site.

Table 4.1: Adsorption free energies of CO_2 in the gas phase (using entropy of -0.64 eV) at $(1\bar{1}00)$ Li_2O_2 surface.

Species	Sites	Adsorption Energy [eV]
CO_2	Step Valley	-0.73
	Terrace Valley	-0.21
	Step Ridge	-0.02

It is required to desorb CO_2 from the surface prior to re-adsorbing at the step site. However, NEB calculations show that once CO_2 is adsorbed at step valley site, the barrier for desorbing is around 3.0 eV, which is not unlikely to remove, see Figure 4.7.

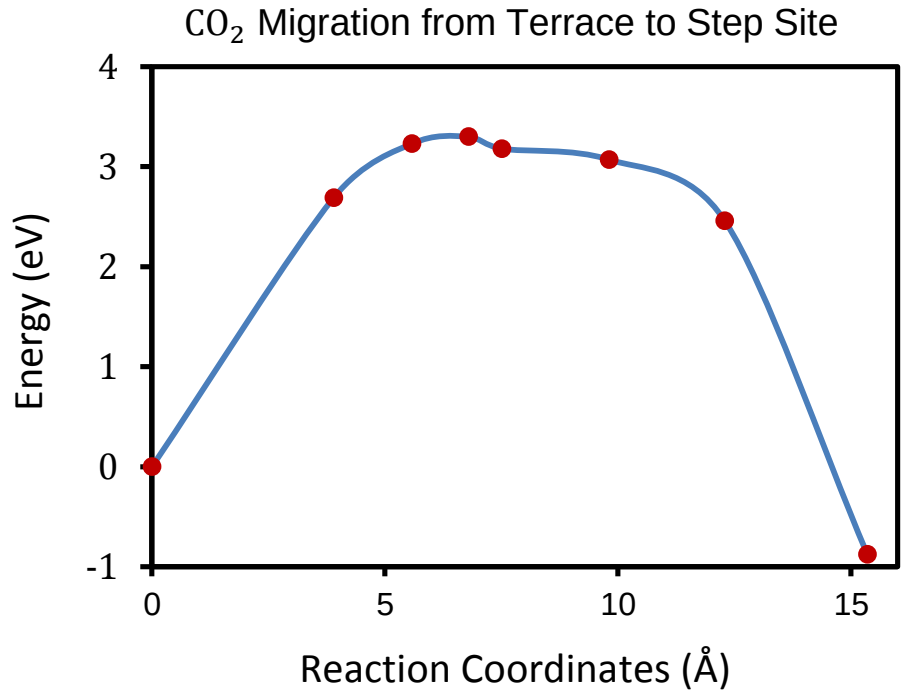

Figure 4.7: Climbing image Nudged elastic band calculations (CI-NEB) for CO_2 migration from less favorable terrace site to more favorable step valley site on stepped $(1\bar{1}00)$ Li_2O_2 surface with energy barrier of ~ 3.0 eV.

4.3.4. Li_2O_2 Reaction Mechanism with and without Trace CO_2 gas

As reported by Siegfried *et al*. [90] and Myrdal *et al*. [67] adsorption of sulfur containing compounds on oxide surfaces could control the electrochemical growth mechanism. Adsorbed species at surfaces can potentially block the nucleation sites, and therefore, alter the growth directions, overpotentials and capacities.

Similarly, Hummelshøj *et al*. [65] also reported that kink and step sites of the stepped $(1\bar{1}00)$ Li_2O_2 surface are favorable nucleation sites for the low overpotential Li_2O_2 growth mechanism. Likewise, we also use the stepped $(1\bar{1}00)$ Li_2O_2 surface to investigate the influence of CO_2 poisoning on the Li_2O_2 growth/ desorption mechanism, Figure 4.8.

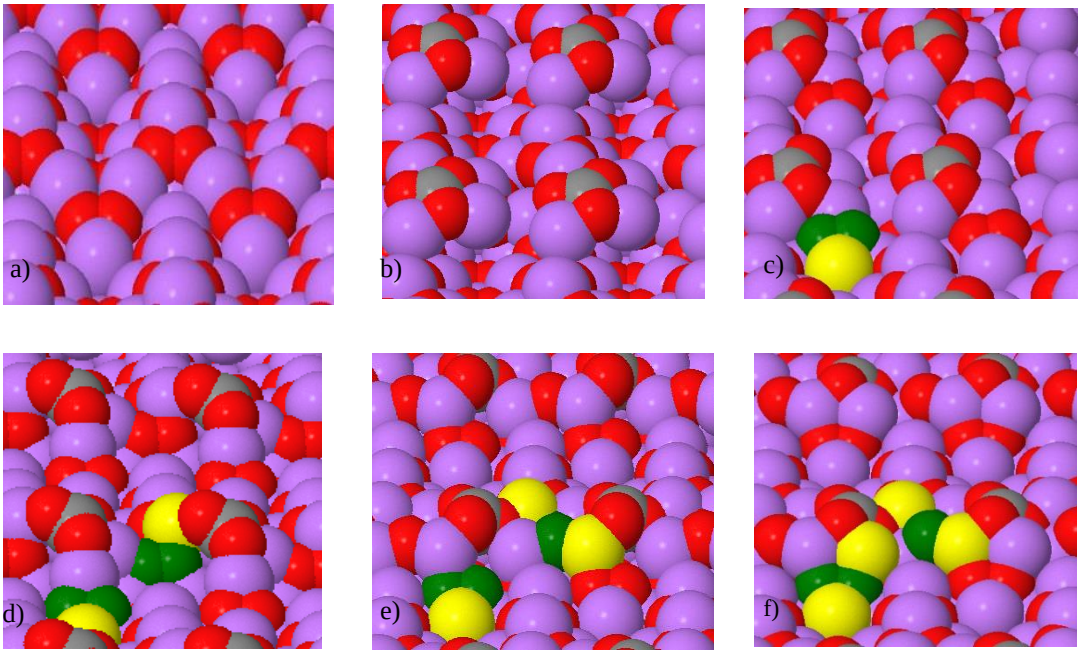

Figure 4.8: Stepped Li_2O_2 $(1\bar{1}00)$ surface before and after adsorption of CO_2 followed by 4 steps of the Li_2O_2 growth pathway during discharge. a) Pure stepped Li_2O_2 surface. b) CO_2 adsorbs to step valley site. c) 1st LiO_2 adsorbs. d) 2nd LiO_2. e) 1st Li. f) 2nd Li adsorbs to the surface completing the growth of 2 Li_2O_2 formula units. Atoms labeled as: gray (Carbon), purple (Lithium) and red (Oxygen). Deposit atoms shown as: yellow (Lithium) and green (Oxygen).

The calculations show a four step Li_2O_2 (two formula units) growth mechanism on the stepped $(1\bar{1}00)$ Li_2O_2 surface with and without CO_2. The first step in the presence of CO_2 is adsorption of

LiO_2 species (Fig 4.8c), and is found to reduce the binding energy by 0.44 V compared to the pure discharge. The next step is the addition of a second LiO_2 species (Fig 4.8d), which is the potential limiting charge step that raises the binding energy by 0.20 V compared to pure Li_2O_2. This is followed by subsequent additions of two Li (Fig 4.8e) and (Fig 4.8f) with relatively small binding energies with respect to a pure discharge. In the pure O_2 discharge mechanism, unlike in the presence of CO_2, addition of the first Li is the limiting charge potential step. The two Li_2O_2 formula units growth at the step surface effectively displaces CO_2 from the step to the less stable terrace site, causing in loss of equilibrium potential by 0.20 V.

Hummelshøj *et al*. have reported that the pure Li_2O_2 growth mechanism follows a four step reaction mechanism, where all reaction steps are electrochemical, similar to what is seen in the presence of CO_2. The equilibrium potential can be obtained as $U_o = -\Delta G/2e$. The effective equilibrium potential on a pure surface becomes 2.73 V (compared to the experimental value, $U_{0,Exp}$ = 2.96 V), while in the presence of CO_2, this is effectively reduced to 2.53 V for the first cycle due to a shift in binding energy of CO_2 from a step valley to terrace site. As a result, discharge at other facets may become active.[64] At neutral bias all reaction steps are downhill, but at an applied potential, the free energy difference for each step is calculated as,

$$\Delta G_{i,u} = \Delta G_i - eU \tag{4.1}$$

The lowest free energy step, $\Delta G_{i,min}$, along the reaction path that first becomes uphill at an applied potential is called the limiting discharge potential, $U_{discharge}$, while the largest free energy step, $\Delta G_{i,max}$, that is last to become downhill for the reversed reaction at an applied potential is called the limited charge potential, U_{charge}, obtained as,

$$U_{discharge} = \min[-\Delta G_i/e] \text{ and } U_{charge} = \max[-\Delta G_i/e] \tag{4.2}$$

In the presence (absence) of CO_2, $U_{discharge}$ = 2.21 V (2.66 V) and U_{charge} = 2.97 V (2.81 V) and the dis/charge overpotentials in the presence (absence) of CO_2 are $\eta_{discharge}$ = 0.31 V (0.07 V) and η_{charge} = 0.44 V (0.08 V). CO_2 poisoning forms Li_2CO_3 -like species that oxidize at high overpotentials.

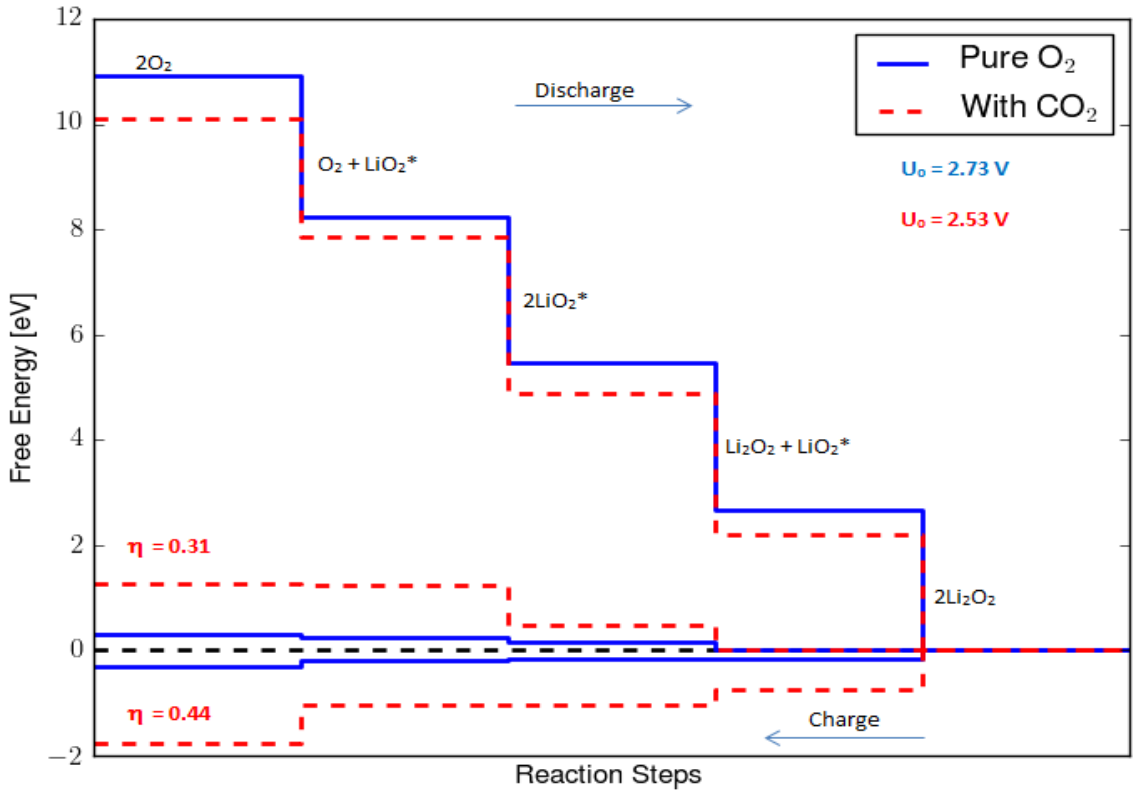

Figure 4.9: Calculated free energy diagrams for a four steps discharge mechanism from stepped $(1\bar{1}00)$ Li_2O_2 surface with and without adsorbed CO_2.

4.4. Catalysis in Li-O_2 /Air Battery

The impacts of various selected catalysts have been surveyed in field of Li-O_2 battery such as Au/C [91], Au/C and Pt/C [92], Pt-Au [93], α-MnO_2 [94], metallic mesoporous pyrochlore [95] and CNT/Co_3O_4 [96]. In the most cases what a catalyst does is to accelerate the degradation of the electrolytes. Some of them are even expensive e.g. gold and platinum. In fact, if the poor electronic conduction and the poor stability of the electrolyte/electrodes was not a problem, there would not be a need for catalysts.

4.5. Cathode-Electrolyte Interfaces (CEI): Li_2O_2@Li_2CO_3 Interface

4.5.1. Introduction

The formation and oxidation of the main discharge product in nonaqueous secondary Li-O_2 batteries, *i.e*. Li_2O_2, has been studied intensively, but less attention has been given to the formation of cathode-electrolyte interfaces (CEI), which could significantly influence the performance of the Li-O_2 /Air batteries.

As already pros and cons associated to the Li-O_2 /Air batteries have been clearly pointed out in chapter 3, one of the areas of interest need to be explored in this technology is an interfacial phenomenal. Numerous complex chemical and electrochemical side-reactions occur at the interfaces in practical nonaqueous Li-O_2 /Air batteries could limit the rechargeability and cyclability. [50] Several kinds of parasitic compounds and interfaces are likely formed between/within the reaction products and cell components in the nonaqueous batteries. The types of interfaces depend on the type of electrodes and electrolytes used in the cell and the reaction conditions. Li_2CO_3 is readily formed at the cathode together with Li_2O_2 when carbonate based electrolytes, *e.g*. ethylene carbonates (EC), are used [77]' [97], but if non-carbonate based electrolytes such as dimethoxyethane (DME) is used, Li_2O_2 is the main discharge product. In the latter case, layers of Li_2CO_3 can also form due to side reaction with the carbon cathode, DME or CO_2 impurities from the air.[48]' [66] The discharge capacity in Li-O_2 batteries is primarily limited by the poor electronic conduction in Li_2O_2 [98] and the since electronic conductivity in Li_2CO_3 is even smaller than that of Li_2O_2, it is critical to determine the effect of such layers.

Experiments performed in carbonate or ether based electrolytes reported the evolution of CO_2 gas when battery recharges at slightly above 3 V and 4 V, mainly comes from the electrolyte decomposition and carbonate deposit at the cathode surface, respectively.[50], [97], [66], [46] It has also been reported in Li-ion battery studies that, Li_2CO_3 is one of the most chemically [99] and mechanically [100] stable species formed at both cathode and anode electrodes. Thus, it is inevitably the formation of the Li_2O_2@Li_2CO_3 interface in the cathode in nonaqueous Li-O_2 /Air batteries at various state of reaction conditions for instance at Li_2O_2@C(graphite) and Li_2O_2@electrolyte interfaces. [50] To summarize, Li_2O_2@Li_2CO_3 interfaces could be formed in different scenarios, *e.g.* a) liquid electrolyte |Li_2CO_3|Li_2O_2| carbon cathode, which may form when carbonate based electrolyte is used or due to the presence of atmospheric CO_2. b) liquid electrolyte |Li_2O_2|Li_2CO_3| carbon cathode, which has been shown to formed due to the reactions between the Li ions and C cathode in the presence of oxygen, and c) liquid electrolyte |Li_2CO_3|Li_2O_2|Li_2CO_3| carbon cathode interfaces [50]. In the present work, we model a generic Li_2O_2@Li_2CO_3 interface, which should be representative for the different scenarios mentioned above, see the Figure 4.10.

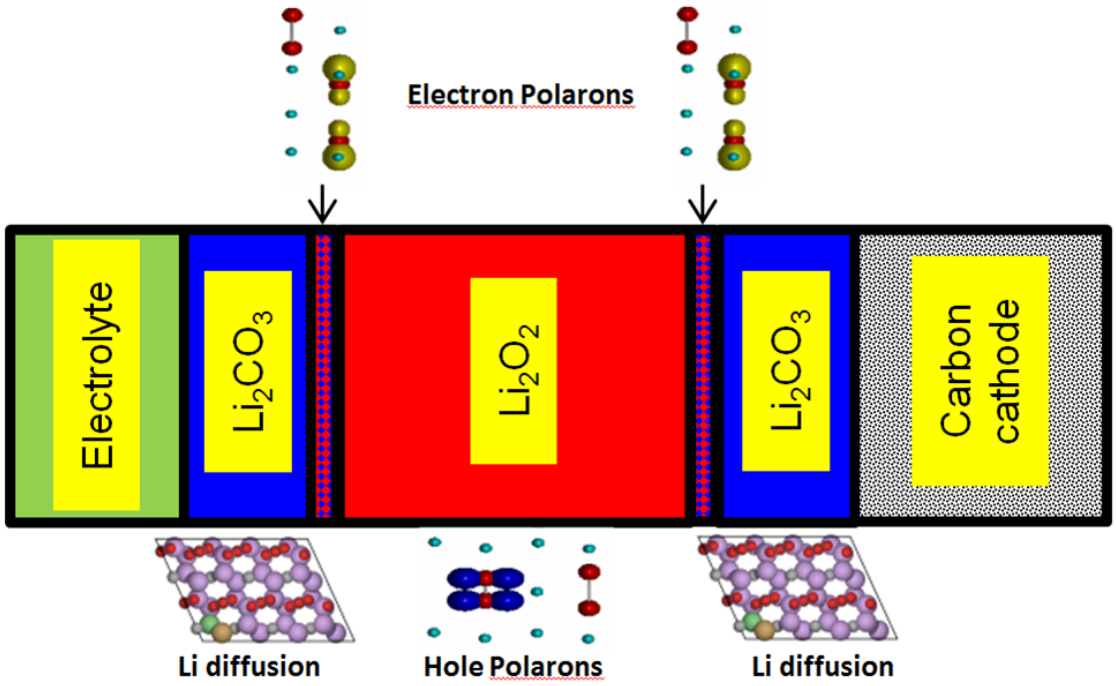

Figure 4.10: Li_2O_2@Li_2CO_3 Interfaces formed at different scenarios in nonaqueous Li-O_2 /Air batteries.

Here, we apply DFT+U and NEGF methods to investigate the role of Li_2O_2@Li_2CO_3 interface layers on the ionic and electronic transport properties at the oxygen electrode. We investigate the

implications of Li_2O_2@Li_2CO_3 interfaces for charge transport, *i.e*. mainly the Lithium diffusion and electronic transport properties in nonaqueous Li-O_2 /Air batteries. [49] Regarding the electronic transport, we study both polaronic and tunneling conduction regimes. We also show that the Li vacancies have a thermodynamic driving force for accumulation at the Li_2O_2 part of the Li_2O_2@Li_2CO_3 interface compared to pristine Li_2O_2. Consequently, we have studied in detail the impact of these Li vacancies on the coherent transport properties at the interface. Lithium vacancies reducing the current by two to three orders of magnitude compared to pristine Li_2O_2. During discharge Li_2O_2@Li_2CO_3 interfaces may, however, provide an alternative in-plane channel for fast electron polaron hopping that could improve the electronic conductivity and ultimately increase the practical capacity in nonaqueous Li-O_2 /Air batteries. In the following subsections we will discuss main findings of the interface studies.

4.5.2. The Interface Setup

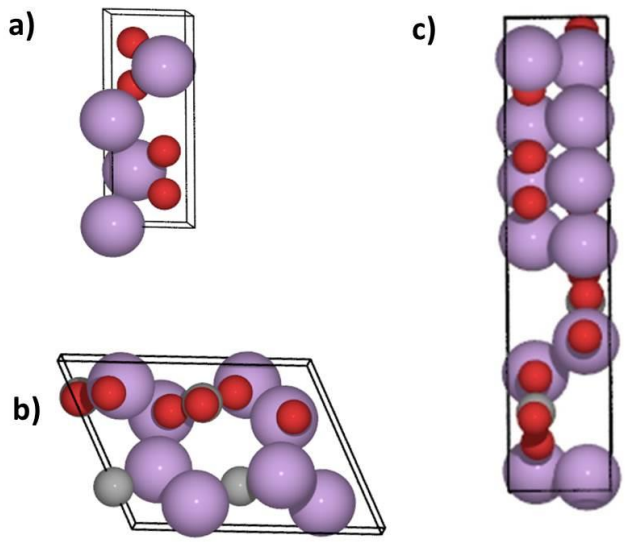

Figure 4.11: (a) Hexagonal Li_2O_2 structure with lattice parameters a = b = 3.187 Å, c = 7.726 Å (space group $P6_3/mmc$). (b) Monoclinic Li_2CO_3 structure with space group 15 (*C*2/*c*) with lattice parameters a = 8.359 Å, b = 4.973 Å, c = 6.197 Å and b = 114.83°. (c) The Li_2O_2@Li_2CO_3 interface, with 4.8 % strains on Li_2O_2.

The Li_2O_2@Li_2CO_3 interface explored in this study is assembled from Li_2CO_3 (adopting a two formula unit cell version of a Li_2CO_3 crystal structure) and Li_2O_2 (adopting a four formula unit cell). The interface is built from a (0001) facet of Li_2O_2 and a (011) facet of Li_2CO_3 with lattice parameters

a = 5.135 Å, b = 6.918 Å, c = 16.165 Å. In both components, oxygen terminated surfaces are used in such a way that the Li and O terminations come together to form the most stable interface. In the Li_2CO_3 part of the interface, the planes of the carbonate groups are aligned parallel to the peroxides along the z-axis. The facets are chosen based on their stability and presence in the discharge products: The (0001) facet is one of the most stable and predominant facets (80 %) on Li_2O_2 around the equilibrium potential during discharge and charge in nonaqueous Li-O_2 /Air batteries, with an abundant portion of the oxygen rich (0001) surface at potentials suitable for charging. [63], [64], [101] Moreover, the Li_2CO_3 (011) surface is one of the low energy facets [102] which has an excellent lattice matching with Li_2O_2 (0001). As it can be seen in Figure 4.11c, the two facets match well and form a stable interface within less than 5 % lattice mismatch (the strain is on Li_2O_2). This constructed interface set-up contains a relatively small number of atoms (the unit cell contains 28 atoms), which makes the calculations tractable, and at the same time provides a reasonable description of the interface. Other calculations could give different results but this one was chosen based on their relative stability, lattice mismatch and size.

4.5.3. Ionic Conduction in the Li_2O_2@Li_2CO_3 Interface

The formation energies of Li vacancies, $V^0_{Li,}$ in Li_2O_2 bulk and Li_2CO_3 bulk are 3.00 eV and 4.20 eV, respectively, whereas the formation energies of V^0_{Li} vacancies at the Li_2O_2@Li_2CO_3 interface are 2.71 eV in the Li_2O_2 part of the interface and 3.24 eV in the Li_2CO_3 part. This means that in both materials, vacancies will accumulate at the Li_2O_2@Li_2CO_3 interface rather than in their respective bulk, see Figure 4.12. The concentration of the Li vacancies should be estimated using the formation energies of the different vacancy species at the working potentials of the battery. [52] We have also calculated that there is no barrier to move V^0_{Li} vacancies from the Li_2CO_3 part of the interface to the Li_2O_2 at a neutral background charge, suggesting that V^0_{Li} vacancies will tend to pile in the latter. This also implies that the presence of the interface will not cause the ionic conductivity to become rate limiting under practical operating conditions in Li-O_2 /Air batteries.

Regarding the Li vacancy migration studies, all the calculations are performed using the Revised Perdew-Burke-Ernzehof (RPBE) exchange correlation functional.

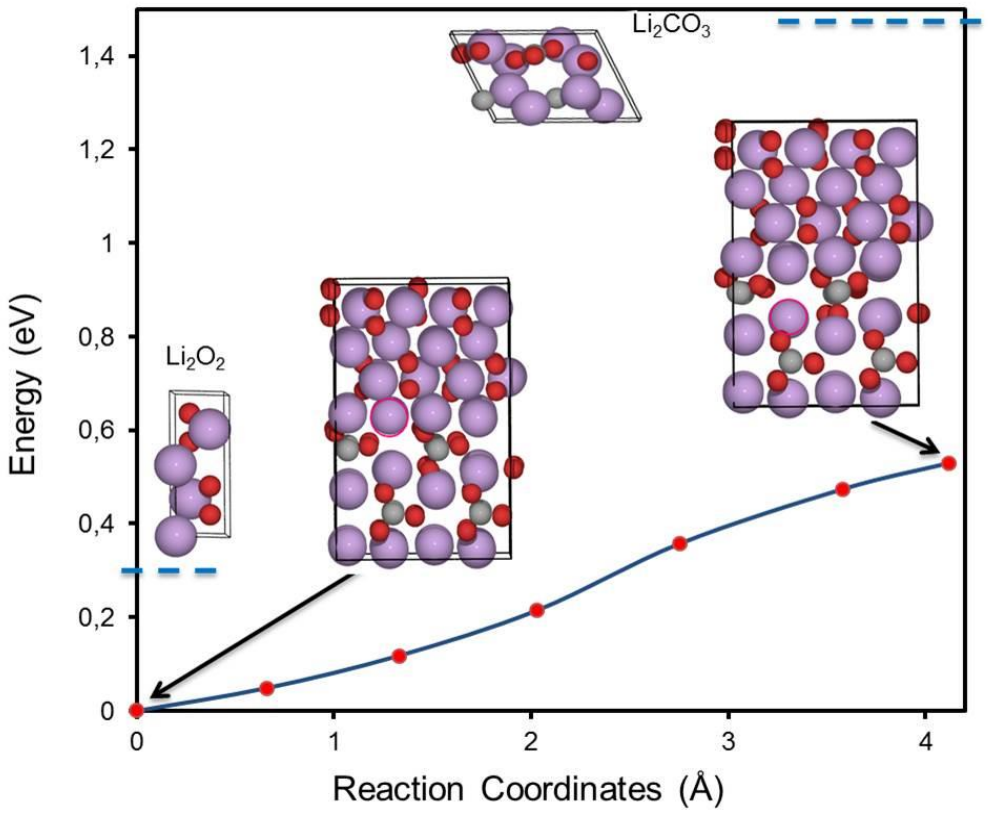

Figure 4.12: NEB calculations for the Li vacancy diffusion barrier at the Li_2O_2 (0001)@Li_2CO_3 (011), interface. The thermodynamic barrier is found to be 0.53 eV going from the peroxide to the carbonate; the blue dashed lines represent the vacancy formation energies of bulk Li_2O_2 (+0.3 eV) and Li_2CO_3 (+ ~1 eV) relative to the interface values.

In order to describe properly the localization of polarons using the general gradient approximation (GGA) functionals, it has previously been reported that it is necessary to introduce Hubbard corrections to the DFT Hamiltonian. Following previous works in our group we use a U = 6 eV Hubbard correction applied on the 2p orbitals of carbon and oxygen atoms.[51]

All ground state energies are determined when Hellmann-Feynman forces is less than 0.03 eV/Å. All the atoms in the supercell are free to relax during the optimization. From the computed E_b , it is possible to obtain the rate (r) and the diffusion coefficient (D) using the relations in equation (2.15) *i.e.* $r = \nu e^{-E_b/k_B T}$ and $\mathrm{D} = a^2 r,$ respectively, where ν is the hopping rate (in this work we use ν =10^{13} s^{-1}) and a is the jump length.

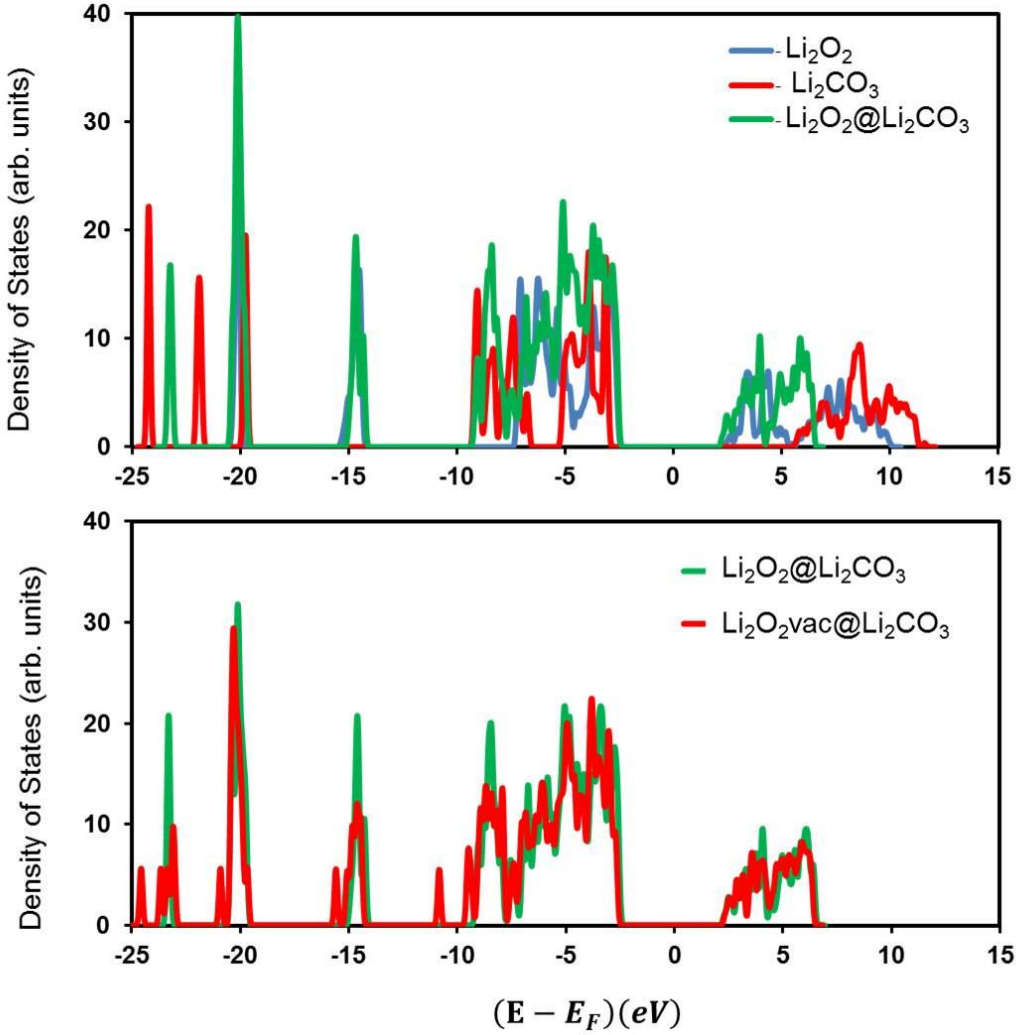

Figure 4.13: The total density of states (DOS) relative to the Fermi energy for (upper) pristine Li_2O_2, Li_2CO_3 and Li_2O_2@Li_2CO_3 interface (bottom) pristine Li_2O_2@Li_2CO_3 and with a defect (neutral Li-vacancy, V_{Li}^{o}) at the peroxide part of the Li_2O_2@Li_2CO_3 interface is obtained using RPBE+U (U = 6 eV)).

The bandgap is also varies depend on the Hubbard's correction (U), as shown in the Figure 4.14 the bandgap increases with U nearly same in both pristine Li_2O_2 and Li_2O_2@Li_2CO_3 interface. Since the origin of the LUMO and HOMO for the Li_2O_2@Li_2CO_3 interface is the Li_2O_2 part of the interface as shown in Figure 4.3.

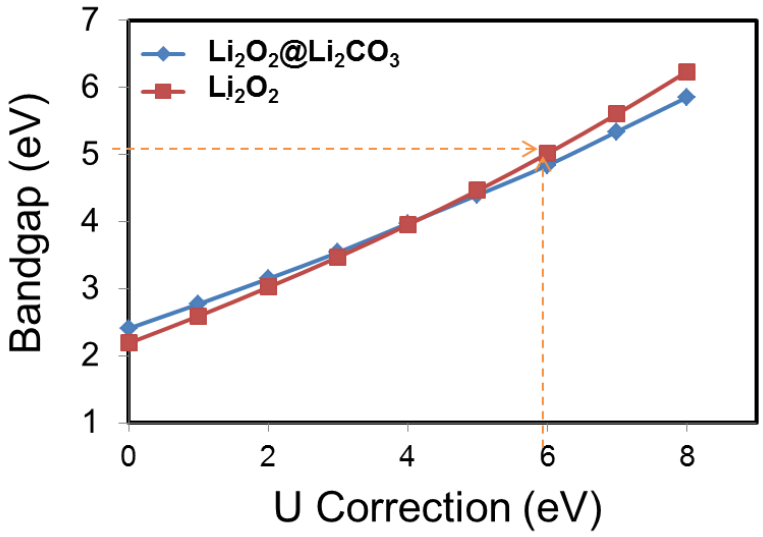

Figure 4.14: Bandgap of bulk pristine Li_2O_2 as a function of Hubbard's correction (U), bandgap increases linearly with U. In the rest of the DFT+U calculations, we use U = 6 eV fits well with G_oW_o results.

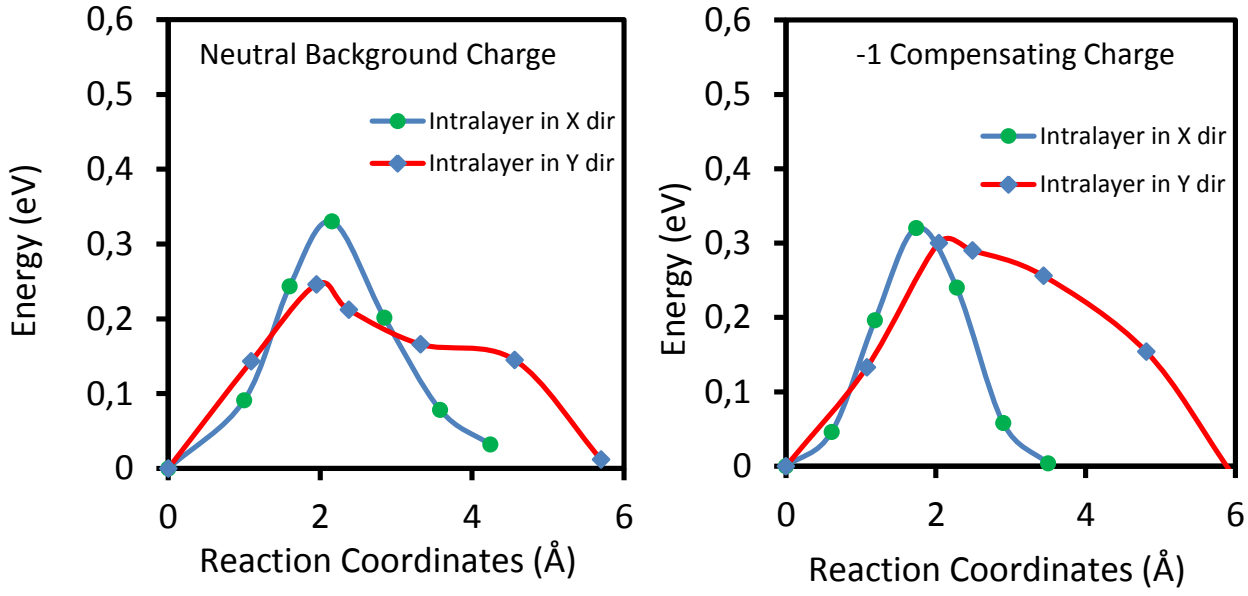

Figure 4.15: NEB calculations for intralayer Li diffusion barrier in the Li_2O_2@Li_2CO_3 interface at a) Neutral b) -1 compensating background charge. Both in-plane channels are within the Li_2O_2 part of the interface. The minimum barrier is found to be ~0.3 eV compared to ~1 eV in pristine Li_2O_2.

As shown in Figure 4.15, too low energy barrier (~ 0.3 eV) is obtained for in-plane lithium diffusion (both at neutral and -1 compensating background charge) in the Li_2O_2 part of the Li_2O_2@Li_2CO_3 interface compared to pristine Li_2O_2 which is about 1 eV. This is mainly due to slight morphology change exhibited at the interface. In Figure 4.11 we have seen that there is no barrier to move V_{Li}^{o} vacancies from the Li_2CO_3 part of the interface to the Li_2O_2 at a neutral background charge, suggesting that V_{Li}^{o} vacancies will tend to pile in the latter. This also implies that the presence of the interface will not cause the ionic conductivity to become rate limiting under practical operating conditions in Li-O_2 /Air batteries.

4.5.4. Coherent Transport in the Li_2O_2@Li_2CO_3 Interface

The coherent electronic transport calculations in the Li_2O_2@Li_2CO_3 interface are carried out using the Nonequilibrium Green's function (NEGF) formalism as implemented in ATK described previously in chapter 2 section 2.5. It has been performed using a LCAO dzp basis set (double-zeta plus polarization). A central device region is connected to two semi-infinite leads, which are kept at fixed electronic chemical potentials, μ_L and μ_R, respectively, to simulate an applied bias voltage across the device region given by $V = (\mu_L - \mu_R)/e$. The scattering region describing the Li_2O_2@Li_2CO_3 interface contains 4 formula units of Li_2CO_3 and 8 formula units of Li_2O_2. The electrode regions, *i.e*. 2 formula units of bulk Li_2CO_3 (left lead) and 4 formula units of Li_2O_2 (right lead), are calculated with the RPBE exchange correlation functional. A $4 \times 6 \times 100$ k-point sampling is used during the NEGF self-consistent loop. In the finite bias calculations, a positive bias is defined as sending electrons from the left to the right, *i.e.* in the case of the interface Li_2CO_3 is the left electrode and Li_2O_2 is the right electrode, see Figure 4.16.

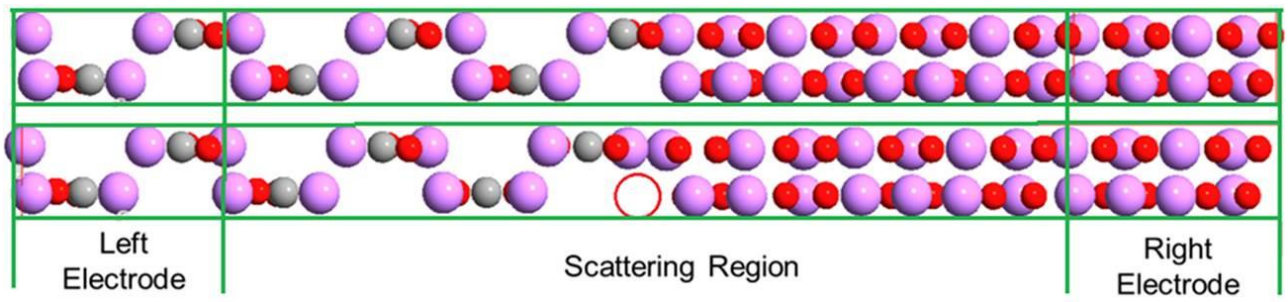

Figure 4.16: Structural setup for the device region for the pristine interface Li_2O_2@Li_2CO_3 (upper), and with a Li-vacancy at the peroxide part of the interface, Li_2O_2vac@Li_2CO_3 (lower).

In order to have a comprehensive understanding of the coherent electron transport at the Li_2O_2@Li_2CO_3 interface it is instructive to examine the density of states (DOS) of Li_2O_2 and Li_2CO_3 bulks and compare them with the one of the interface. In Figure 4.13, we can see that both Li_2O_2 and Li_2CO_3 are both wide bandgap insulators with calculated bandgaps (using RPBE+U functional with U = 6 eV) of 5.03 eV for Li_2O_2 and 8.01 eV for Li_2CO_3. The Li_2O_2@Li_2CO_3 interface shows a 4.82 eV bandgap (very close to the one of pristine Li_2O_2 bulk) and it can be viewed as the superposition of individual DOS of the Li_2O_2 and Li_2CO_3, with no presence of mid-gap interface states. In this situation it is expected that for bias voltages (negative or positive) around 2-2.5 eV (*i.e*. half of the bandgap of Li_2O_2) we will start to see a relatively good conductance in Li_2O_2 bulk. However, for the same bias we will expect a drastic drop in the conductance at the Li_2O_2@Li_2CO_3 interface since there are no Li_2CO_3 levels at these energies.

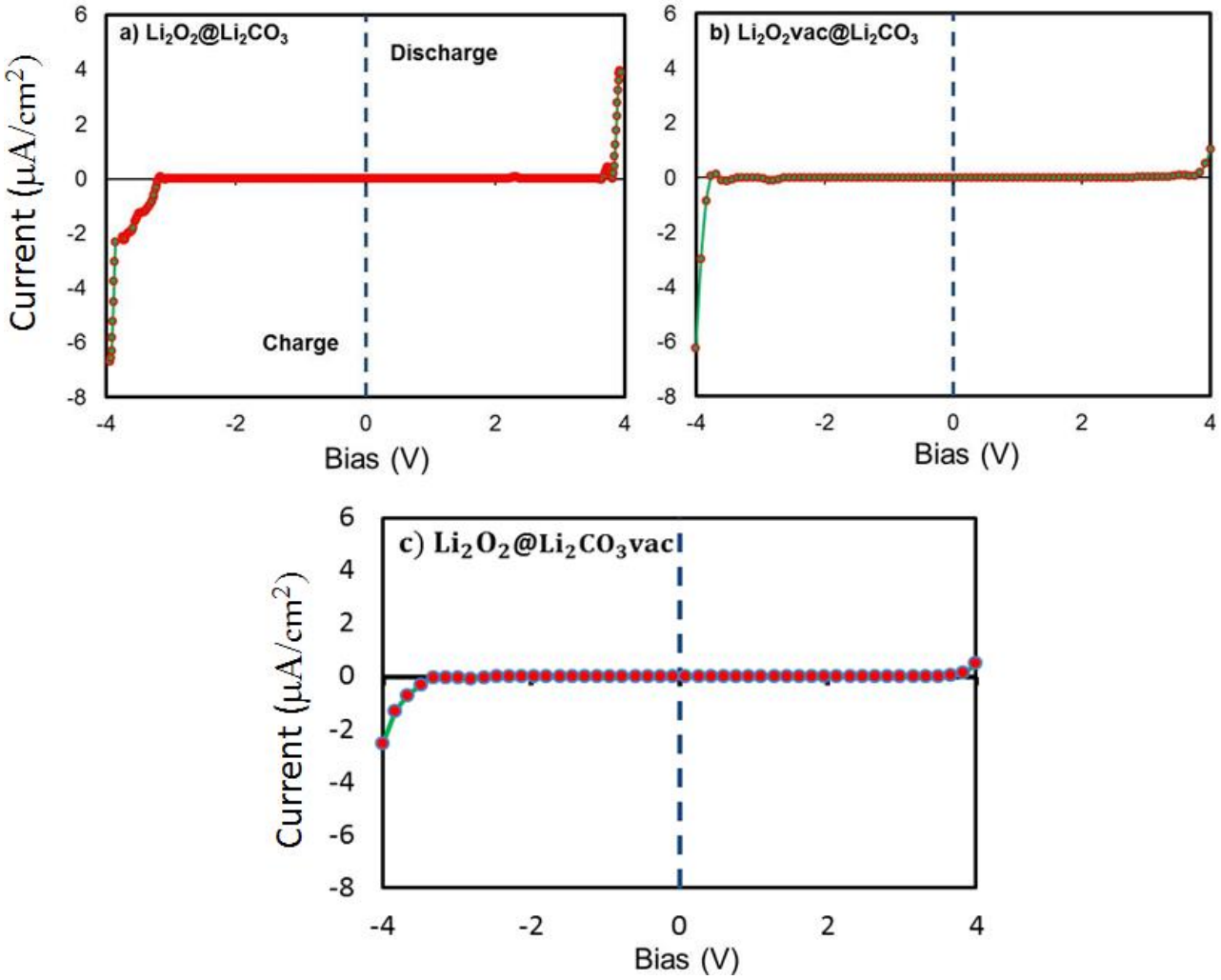

Figure 4.17: Calculated IV curves for a) pristine Li_2O_2@Li_2CO_3 interface. b) and c) in the presence of a neutral Li vacancy at Li_2O_2vac@Li_2CO_3 and Li_2O_2@Li_2CO_3vac interfaces, respectively.

Regarding the presence of vacancies in Li_2O_2 bulk and at the Li_2O_2@Li_2CO_3 interface (vacancies are located at the Li_2O_2 part of the interface, following the results in section 3.3). As the DOS of both Li_2O_2 and Li_2O_2@Li_2CO_3 interface revealed the presence of lithium vacancies pin the Fermi level to the right, see Figure 4.18. This implies that V^0_{Li} vacancies are not going to open new electron tunneling channels in these systems and they are going to have a detrimental effect in the conductivity due to their action as scattering centers.

In order to check the plausibility of these assumptions we perform DFT-NEGF calculations as described in section 2.4. We can see in Figure 3.4a that significant current (around ~10 $\mathrm{mA/cm^2}$) begins to show up just around $\pm$ 2.0 V in pristine Li_2O_2 bulk. However, at the interface current start rising at higher potentials (above $\pm$ 3.8 V, see Figure 4.17a), due to the wider gap of Li_2CO_3, and currents are also reduced three orders of magnitude with respect to the ones in Li_2O_2 bulk. Furthermore V^0_{Li} vacancies reduce the currents at relevant voltages, of both Li_2O_2 bulk and Li_2O_2@Li_2CO_3 interface, by a factor of 2. The vacancy formation energy of the defect interface, when a Li vacancy is created at the carbonate part of the interface, is found to around 3.3 eV. According to NEGFs calculations a Li vacancy at the interface reduces the amount of drawn discharge currents. This even extends to charge currents when the defect (Li vacancy) is seized at carbonate part of the interface, see Figure 4.17c.

Summarizing, we can conclude that the presence of Li_2O_2@Li_2CO_3 interfaces and V^0_{Li} vacancies in Li_2O_2 has a substantial negative effect on the coherent electronic transport at the oxygen electrode of Li-O_2 batteries.

4.5.5. Polaronic Conduction in the Pristine Li_2O_2@Li_2CO_3 Interface

Garcia-Lastra et al. have already reported that both Li_2O_2 and Li_2CO_3 bulks can hold hole polarons with sufficiently low migration barriers (0.39 eV for the former and 0.55 eV for the latter) to become an alternative path for electronic transport.[51] We have also found very similar results for polaron studies in Li_2O_2 bulk, as shown in section 3.5. They also found that both materials can hold excess electron polarons. However, the migration barriers for electron polarons are much higher than the ones of hole polarons (1.408 eV in Li_2O_2 and 1.05 in Li_2CO_3). In this subsection polaronic conduction (for both holes and excess electrons) at the Li_2O_2@Li_2CO_3 interface will be discussed.

Table 4. 2: Energy Difference between Localized (Polaron) and Delocalized States ($\Delta E_{loc\text{-}del}$) in Electronvolts for the Li_2O_2@Li_2CO_3 interface [a].

method	hole polaron in the Li_2O_2 part	hole polaron in the Li_2CO_3 part	electron polaron in the Li_2O_2 part	electron polaron in the Li_2CO_3 part
RPBE	delocalized	delocalized	delocalized	Delocalized
RPBE+U	-1.40	-0,57	-2.57	-2.67

[a]Hole and excess electron are localized at the Li_2O_2 and Li_2CO_3 parts of the interface using RPBE + U (U = 6 eV), as shown in Table 4.2.

When we consider polaron localization at the Li_2O_2 part of the interface we observe that the hole (excess electron) polaron is localized by shortening (stretching) the bond length of one of the O−O peroxide bond from 1.55 to 1.33 Å (2.45 Å). Apart from the geometry distortions we observe the appearance of a magnetic moment in one of the oxyanions, which is another footprint of the hole (excess electron) localization at the Li_2O_2 part of the interface. The polaron localization can also take place at the Li_2CO_3 part of the interface. In this case the hole (excess electron) is localized in one of the carbonate ions which shortens (stretches) its C-O bond lengths from an average of 1.31 Å to an average of 1.23 Å (1.35 Å).These localized states are more stable than the delocalized ones and particularly the electron polaron is found to be strongly localized, *i.e*. by more than 2 eV relative to the delocalized state (see Table 1.1). All these features are very similar to the ones we found for Li_2O_2 and Li_2CO_3 bulks in section 3.5 and 4.2.2, for detail refer[51].

It is interesting to notice that hole polarons are more stable in the Li_2O_2 part of the Li_2O_2@Li_2CO_3 interface by 0.83 eV, whereas the excess electron polarons are more stable in the Li_2CO_3 part by 0.10 eV (see Table 4.2 and Figure 4.16). This is due to the different magnitude of the distortions in the peroxide ions of Li_2O_2, *i.e*. a hole localized in a peroxide ion involves a change in the O−O bonding distance of 0.2 Å, while the localization of an excess electron requires stretching the bonding by 0.9 Å.

Accordingly to the NEB calculations, the energy barriers for the polaronic transport of excess electrons across the interface (see direction z in Figure 4.16) are very similar to the ones observed in Li_2O_2 and Li_2CO_3 bulks. The barrier for transporting excess electron polarons from Li_2O_2 to Li_2CO_3 is 1.39 eV (and 1.48 eV from Li_2CO_3 to Li_2O_2), very close to the Li_2O_2 bulk and Li_2CO_3 bulk. This implies that the excess electron polaronic transport in Li_2O_2, Li_2CO_3 and across Li_2O_2@Li_2CO_3 interfaces (from Carbonate to peroxide part of the interface) is inaccessible channel for electronic transport. The polaron hopping barrier for holes is much more asymmetric: the barrier for the hop from Li_2CO_3 to Li_2O_2 is 0.4 eV (in Li_2O_2 bulk is 0.39 eV [51]), while it is 1.3 eV in the opposite direction. In this scenario we can conclude that Li_2O_2@Li_2CO_3 interfaces act like a diode, which allows hole polaronic transport only from the Li_2CO_3 part of the interface to the Li_2O_2 one.

Regarding the polaronic transport parallel to the Li_2O_2@Li_2CO_3 interface we observe that an alternative channel for electron polaron hopping opens within the peroxide part of the interface (intralayer in the X and Y directions in Figure 4.16) with a low hopping barrier of less than 0.5 eV, providing an improved conduction channel compared to bulk Li_2O_2. The corresponding rates (*r*) in X and Y intralayer electron polaron hopping are found to be $5\mathrm{x}10^{5}\mathrm{s}^{-1}$ and $9\mathrm{x}10^{7}\mathrm{s}^{-1}$ with the diffusion coefficients of $5x10^{-10}\,\mathrm{cm}^2/\mathrm{s}$ and $1x10^{-7}\,\mathrm{cm}^2/\mathrm{s}$, respectively. Unlike what is observed for bulk Li_2O_2, the hole polaron hopping barriers in the Li_2O_2@Li_2CO_3 interface are significantly larger compared to the low barriers reported for Li_2O_2 by Garcia, *et al* [51]. On the other hand, the intralayer hole polaron hopping at the Li_2O_2@Li_2CO_3 interface is quite limited in comparison with that of Li_2O_2 bulk (the barriers at the interface are at least twice larger than in Li_2O_2 bulk).

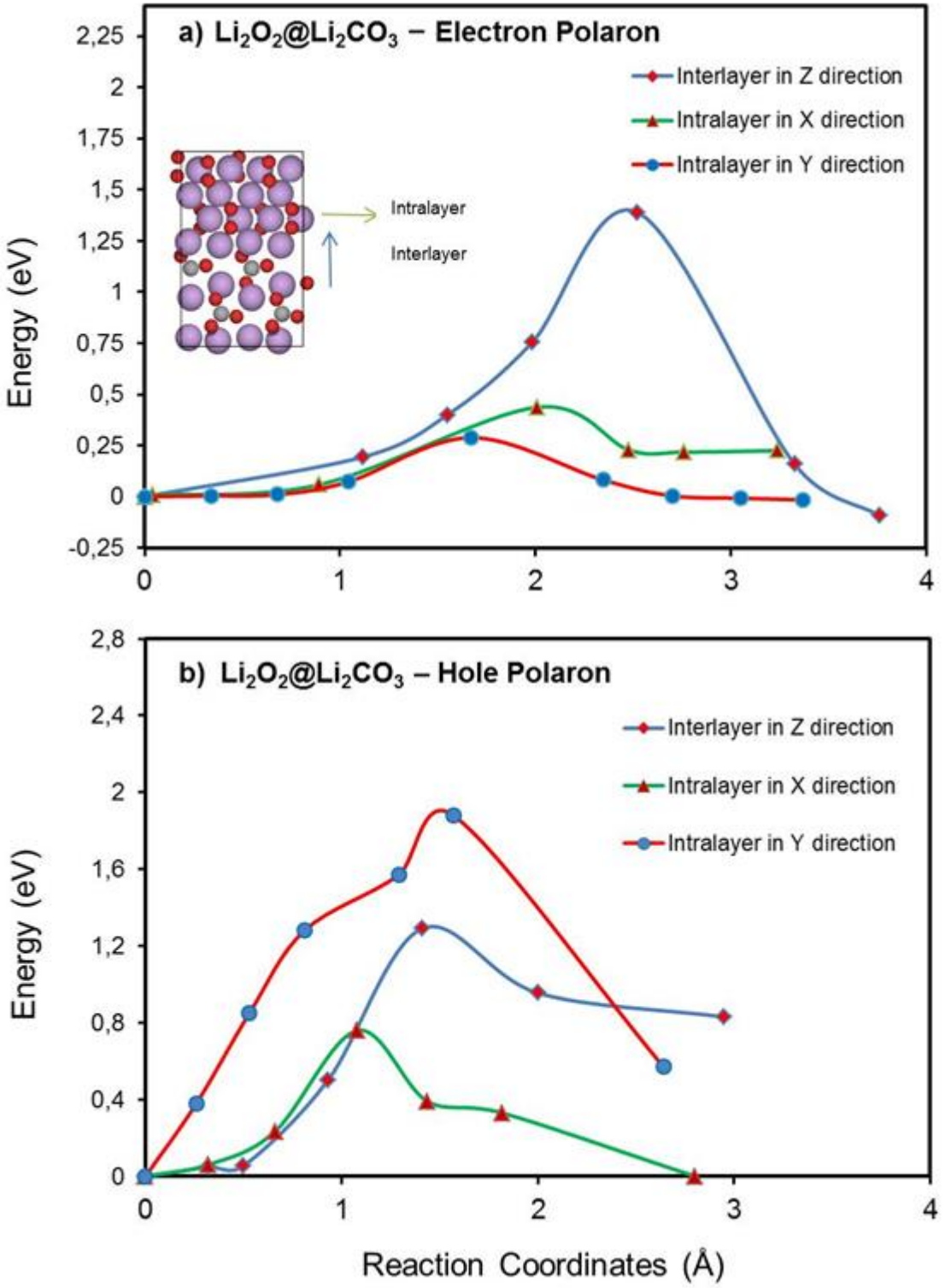

Figure 4.18. Calculated polaron hopping paths using the NEB method along the intralayer in X and Y directions and interlayer along Z direction in a $2 \times 2 \times 1$ Li_2O_2@Li_2CO_3 interface supercell. Energies are obtained from RPBE + U (U = 6 eV) method for a) Electron and b) Hole.

4.6. Summary of Charge Transport and CO_2 Poisoning Studies

The overall plausible charge transport mechanisms in the materials of interest in nonaqueous Li-O_2 batteries are clearly envisioned in Figure 4.10. To summarize only a few most important aspects of charge transport calculations in the bulk (dominant discharge product in ether based electrolytes like DME) in the Li-O_2 batteries revealed that though the Li_2O_2 is a wide bandgap insulator (4.96 eV) it could offer a fast ionic conduction with an activation barrier of 0.40 eV only along interlayer channel (1D diffusion mechanism). An average rate of $r = 2x10^6 s^{-1}$ and a diffusion coefficient of $\mathrm{D} = 1.5x10^{-9}\,\mathrm{cm}^2/\mathrm{s}$ is estimated using equation (2.15). This relatively small barrier opens the possibility for Li ion diffusion at ambient conditions. However, the ionic diffusion along the intralayer in both X and Y directions are found to be limiting the ionic transport (≥ 1.0 eV). Moreover, we have also conducted ionic charge transport studies in one of the dominant side reaction product in Li-O_2 /Air, *i.e.* Li_2CO_3, resulting in several minimum energy barriers for different negative Li vacancy diffusions, *i.e*. ~0.2 eV in all the three directions. Accordingly, the average rate of negative Li vacancy (Li^+ missing) diffusion and diffusion coefficient in Li_2CO_3 are found to be $9x10^8 s^{-1}$ and $1.6x10^{-6}\,\mathrm{cm}^2/\mathrm{s}$, respectively. Regarding the polaron transport across these two materials (Li_2O_2 and Li_2CO_3 bulk) the polaronic transport at room temperature is restricted to hole polarons, whereas electron polarons display very high hopping barriers (> 1.0 eV). Therefore, as a summary of the charge transport investigations in these two materials the plausible charge transport mechanisms are the two defect systems *i.e.* negative lithium vacancy (missing Li^+) and hole polaron (removing an electron).

We have also comprehensively examined the charge transport mechanisms at the cathode-electrolyte interfaces (CEI) in nonaqueous Li-O_2 /Air battery, *i.e.* Li_2O_2@Li_2CO_3 interface on top of the study of charge transport in the bulk of discharge products. Since their roles on charge transport have not been clearly studied earlier nevertheless some experiments reports that various interface layers potentially influence the performance of the battery. We model the interface from (0001) Li_2O_2 facets (the most stable and highly exposed facets) and (011) Li_2CO_3 facet which matches well with the peroxide with < 5% strain (lattice mismatch). The main findings are lithium vacancies accumulate at the peroxide part of this interface and reducing the coherent electron transport by two to three orders of magnitude compared to pristine Li_2O_2 bulk. By contrast, the Li_2O_2@Li_2CO_3 interface improves the ionic conduction. The Li_2O_2@Li_2CO_3 interface show a barrier of < 0.35 eV in all directions unlike that of the one dimensional diffusion in Li_2O_2. Regarding the polaronic transport significant differences are also found in these two scenarios. In Li_2O_2 bulk the

polaronic transport at room temperature is restricted to hole polarons, whereas electron polarons display very high hopping barriers (> 1.0 eV). By contrast, it is possible to have good mobilities for electron polarons at the Li_2O_2@Li_2CO_3 interface. During discharge the Li_2O_2@Li_2CO_3 interfaces may, however, provide an alternative in-plane channel for fast electron polaron hopping that could improve the electronic conductivity and ultimately increase the practical capacity in non-aqueous Li-O_2 batteries (Paper II).

Moreover, the implications of air impurities particularly the influence of CO_2 poisoning on discharge capacity and overpotentials in nonaqueous Li-O_2 /Air batteries were studied in depth both computationally (DFT calculations) and experimentally (using some electroanalytical and spectroscopy techniques) performed at DTU Energy by Kristian and Jonathan. The presence of small concentration of CO_2 gas in nonaqueous Li-O_2 battery results in the formation of Li_2CO_3 like species from the reactions between CO_2 and Li_2O_2 at the cathode surface. To study this computationally we have used the step $(1\bar{1}00)$ Li_2O_2 surface model. The galvanostatic charge-discharge measurements were also studied as shown in paper I. From both DFT results and experimental works we concluded that even low concentration of CO_2 gas effectively blocks the step nucleation site and alters the Li_2O_2 shape due to Li_2CO_3 formation. Moreover, the nudge elastic band calculations showed that once CO_2 is adsorbed on a step valley site, it is effectively unable to diffuse and therefore cause an impact on capacity and overpotentials. The charging processes are strongly influenced by CO_2 poisoning, and exhibits increased overpotentials and increased capacity already at 1 % CO_2. Though, large capacity and overpotentials losses are seen at even higher CO_2 concentrations (Paper I).

CHAPTER 5

Na-O_2 Batteries

5.1 Introduction

In this chapter we will present another newly emerging metal-air battery, *i.e*. Na-O_2 /Air battery. In the last decade, significant efforts have been paid to the development of next generation batteries. In particular, the metal-air batteries (Li-, Na-, Mg-, Al-, Fe- and Zn−O_2 batteries) in either aqueous or non-aqueous (aprotic) electrolytes have gained a lot of attention,[12],[13] e.g. for use in electric vehicles. The cost of commercially available Li-ion batteries is generally too high and the energy storage capacity is too low to solve the increasing demands on batteries for transportation [14]. Metal-air batteries have high theoretical specific energies since the technology, once it is mature, would apply metal as an anode and oxygen gas from air on the cathode side. The reaction products are peroxides and/or superoxides during discharge depending on the experimental conditions and cell components used in the system. The oxygen reduction (ORR) and oxygen evolution reaction (OER) are the two main reactions taking place reversibly during discharge and charging, respectively. However, metal-air battery technologies are limited by a number of drawbacks and challenges, which must be resolved before becoming commercially viable, *i.e.* low accessible capacity (sudden death), poor electronic conductivity and rechargeability, limited chemical and electrochemical stability of electrodes, electrolytes [78], salts [103] and high sensitivity to air impurity-like water and CO_2. [45],[18],[66],[104],[42]

Among the battery systems reported so far, the Li−O_2 couple offers higher equilibrium potential (~2.96 V) and extremely high specific capacity (~3,842 mAh/g), which is comparable to gasoline [15] and nearly an order of magnitude higher than that of current Li-ion batteries [16]. However, in practice non-aqueous Li-O_2 batteries suffer from poor rechargeability and high overpotentials, particularly at charging process. [17] Although the capacity and equilibrium potential is lower, the Na−O_2 battery technology displays some advantages over the Li−O_2 battery and other similar batteries. The non-aqueous secondary Na−O_2 battery operates at low dis/charge overpotentials (< 200 mV) even at higher current densities (0.2 mA/cm^2) and yields high electrical energy efficiency

(90 %), which is consistently observed for many cycles.[105],[20],[19]. The theoretical specific capacity of the Na–O_2 battery is ~1,500 mAh/g [19] when NaO_2 deposited on carbon nanotubes. This is lower compared to the Li–O_2, but still higher than the existing Li-ion batteries; at least twice the Li-ion batteries, which is about half of the state of the art Li–O_2 battery specific capacity. If, however, Na_2O_2 can be formed reversibly, it would be possible to increase the specific capacity to ~2,800 mAh/g. [106]

Among the battery systems reported so far, the Li–O_2 couple offer higher equilibrium potential (~2.96 V) and extremely high specific capacity (~3842 mAh/g), which is comparable to gasoline [15] and nearly an order of magnitude higher than that of current Li-ion batteries [16]. However, in practice nonaqueous Li-O_2 batteries suffer from poor rechargeability and high overpotential particularly at the charging process. Although the capacity and equilibrium potential is lower, the Na–O_2 battery technology displays some advantages over the Li–O_2 battery and other similar batteries. The nonaqueous rechargeable Na–O_2 battery operates at low dis/charge overpotentials (< 200 mV) even at higher current densities (0.2 mA/cm^2) and yield high electrical energy efficiency (90 %), which is consistently observed for many cycles.[105],[20],[19]. The theoretical specific capacity the Na–O_2 battery is about 1500 mAh/g [19] when NaO_2 is grown on carbon nanotubes which is lower compared to the Li–O_2 but still higher than the existing Li-ion batteries, at least twice the Li-ion batteries, which is about half of the state of the art Li–O_2 battery specific capacity. If, however, Na_2O_2 can be formed reversibly, it would be possible to increase the specific capacity to 2800 mAh/g. [106]

Hartmann *et al*. [20],[107] and McCloskey *et al*. [108] have reported sodium superoxide (NaO_2) as the dominant reaction product. Whereas, Kim *et al.* [106] have reported sodium peroxide (Na_2O_2) as dominant discharge product instead. Poor rechargeability (< 10 cycles) and high charging overpotential (> 1.3 V) is exhibited when Na_2O_2 is formed at the cathode at room temperature, which is also similar to the challenges observed in Li–O_2 system. However, sufficiently low dis/charge overpotentials and interestingly high rechargeability are observed when NaO_2 is formed [19].

Scanning electron microscopy (SEM) image have revealed that highly ordered cubic NaO_2 is grown at the carbon cathode surface. [20],[108],[107] A recent computational study by Ceder *et al.* reports that NaO_2 is more stable at the nanoscale level (up to about 5 nm), whereas bulk Na_2O_2 is thermodynamically stable at standard conditions (in agreement with experimental observations). For electrochemical growth during battery discharge, the size of the NaO_2 particles is, however, found in the micrometer size (1-50 micro meters). [20] The size of the particle cannot be explained

from the effect of the differences in surface energy, nor the effect of e.g. oxygen partial pressure or temperature, which may lead to the formation of larger NaO_2 particles (up to 20 nm based on the calculations by Ceder *et al*. It is therefore clear that NaO_2 formation is not only kinetically but also thermodynamically favored in an increased oxygen partial pressure even at higher temperatures and lead to a higher scale growth (up to 20 nm). [109]

The equation for non-aqueous Na–O_2 cathode electrochemistry using, e.g. ether based electrolytes like diglyme is shown below [108].

$$\mathrm{Na^+ + e^- + O_2 \leftrightarrow NaO_2}, \qquad \mathrm{E^0 = 2.27\ V, Vs\ Na/Na^+}$$

According to a previous report by Kang *et al.,* [110] flat low index surfaces of NaO_2 are activated by a chemical barrier up to 0.8 V. Moreover, according to HSE Hybrid functional calculations the bandgap of NaO_2 is found to be as low as 1.11 eV [110]. Siegel *et al*. [111] however, reported that GW calculations revealed wide bandgap of 5.30 eV and 6.65 eV for NaO_2 and Na_2O_2, respectively. Nevertheless, a 1.3 eV experimental bandgap is previously reported for KO_2 (similar to NaO_2) [112].

In this study, reaction pathways on some selected stepped model surfaces *i.e*., (001) and (100) for NaO_2 and $(1\bar{1}00)$ for Na_2O_2 is investigated. We will discuss overpotentials and free energies of the reaction mechanisms as a function of temperature. Hence, the step surfaces are likely to give accessible barriers and favorable nucleation sites for minimum overpotentials, as it has been reported in case of Li–O_2 [64]. Furthermore, in this chapter we will discuss the charge carrier transport in NaO_2 and Na_2O_2.

5.2 Crystal Structures and Computational Models

Similarly, here present fundamental investigations at the DFT-level using PBE. The study is conducted in the materials of interest in the Na–O_2 battery, *i.e.* NaO_2 and Na_2O_2. The face-centered cubic NaO_2 structure space group of $Pa\bar{3}$ with a lattice constant of 5.523 Å (Figure 5.1b) [110] is used to build the supercell model to study the NaO_2 growth/depletion mechanism on stepped (001) and (100) surfaces of NaO_2. The supercell consists of 60-72 atoms. The vacuum layer between periodic images along the Z-axis is 20 Å. All presented calculations are spin-polarized with an initial magnetic moment values of 0.5 located in each O atom in NaO_2. The k-points are sampled with a $2 \times 4 \times 1$ Monkhorst-Pack mesh. For the ionic diffusion studies in NaO_2 is conducted in a $3 \times 3 \times 3$ supercell. Regarding the Na_2O_2 surface reaction mechanism studies,

due to the computational complexity (3 formula units per unit cell) in describing stepped surfaces of Na_2O_2, the highly similar and well-studied stepped $(1\bar{1}00)$ surface model of Li_2O_2 (space group $P6_3/mmc$) is adopted instead for Na_2O_2 reaction mechanism studies on the stepped surface. The stepped $(1\bar{1}00)$ Na_2O_2 surface with a super cell consisting of a 56-64 atoms slab with a 18 Å vacuum layer between periodic images along the z-axis is used to study the reaction mechanism. The k-points are sampled with a (4,4,1) Monkhorst-Pack mesh and 0.18 Å grid point spacing is used. Atomic energy optimization calculations are performed until all forces are less than 0.03 eV/Å. For ionic diffusion studies a $2 \times 2 \times 2$ supercell of a hexagonal Na_2O_2 structure space group of $P\bar{6}2m$ with lattice constants of a = 6.39 Å, b = 6.39 Å and c = 4.6 Å is used.

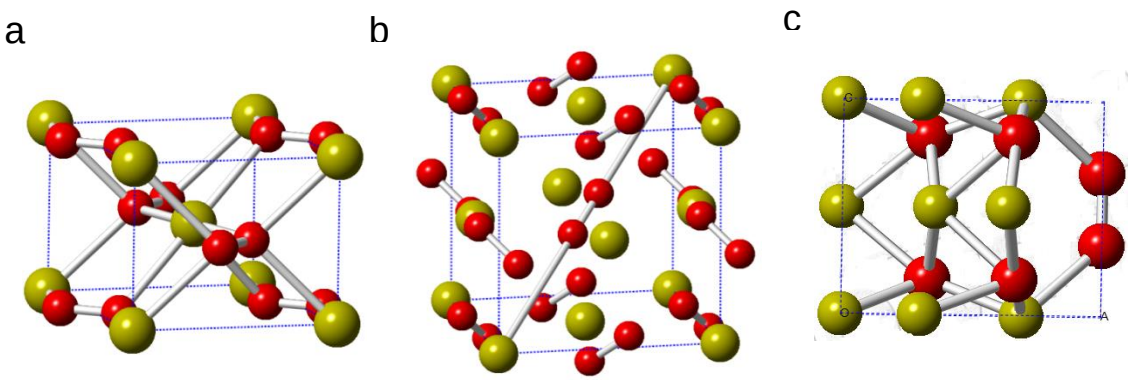

Figure 5.1: Figure 2: a) *Pnnm* NaO_2 orthorhombic structure with lattice constant a = 4.26 Å, b = 5.44 Å, c = 3.36 Å. b) Face-centered cube $Pa\bar{3}$ NaO_2 structure (Pyrite) with lattice constant a = 5.523 Å. c) Hexagonal Na_2O_2 structure space group of $P\bar{6}2m$ with lattice constants of a = 6.39 Å, b = 6.39 Å and c = 4.6 Å. Color: Grey (Sodium), Red (Oxygen).

It should be noted that this significant discrepancy is obtained using higher-level computational methods like HSE and GW. This illustrates the computational complexity of the Na-O_2 system, which in part, is due to the computational challenges in describing the thermodynamics of reactions involving superoxide vs. peroxide species and to the high temperature phase of NaO_2 ($Pa\bar{3}$) being dynamically stabilized relative to the orthorhombic low temperature phase (*Pnnm*) by procession of misaligned superoxide species (see Figure 5.1). Such effects and energetics are generally not accounted for in DFT or higher-level calculations, making it highly challenging to describe the relative stability of NaO_2 vs. Na_2O_2 at finite temperatures. In the following, we describe a comparatively simple GGA-level computational approach using metal chloride reference energies and entropic contributions, which yields excellent agreement with experimental observations.

To evaluate the accuracy of the calculations, bulk enthalpies of formation are compared with experiment [89] as seen in Table 1. The calculated formation enthalpies are converted to free energies at standard conditions (ΔH_{form} -> ΔG_{form}) using experimental entropies [89] and the equilibrium potential calculated. As an alternative to using experimental entropies, we predict the equilibrium potentials with the approximation that the temperature dependence can be described solely considering the translational and rotational degrees of freedom of O_2(g). As superoxide ions are known to rotate easily in the NaO_2 pyrite phase at room temperature, rotational degrees of freedom will to a good approximation cancel for NaO_2. This is not the case for NaO_2, where the orientation of peroxide ions is well defined at relevant temperatures. The approximation has obvious flaws, e.g. will it not be able to capture the low temperature structural changes of NaO_2 due to differences in the rotational degrees of freedom of superoxide ions in different phases. It does, however, have the advantage of being very simple to calculate with standard thermodynamics. Comparison with experiment also proves the simple assumption to be reasonable (see Figure 5.2). It can also be seen that the experimental data for NaO_2 at 0 K is identical to the calculational result for the *Pnnm* structure.

‘

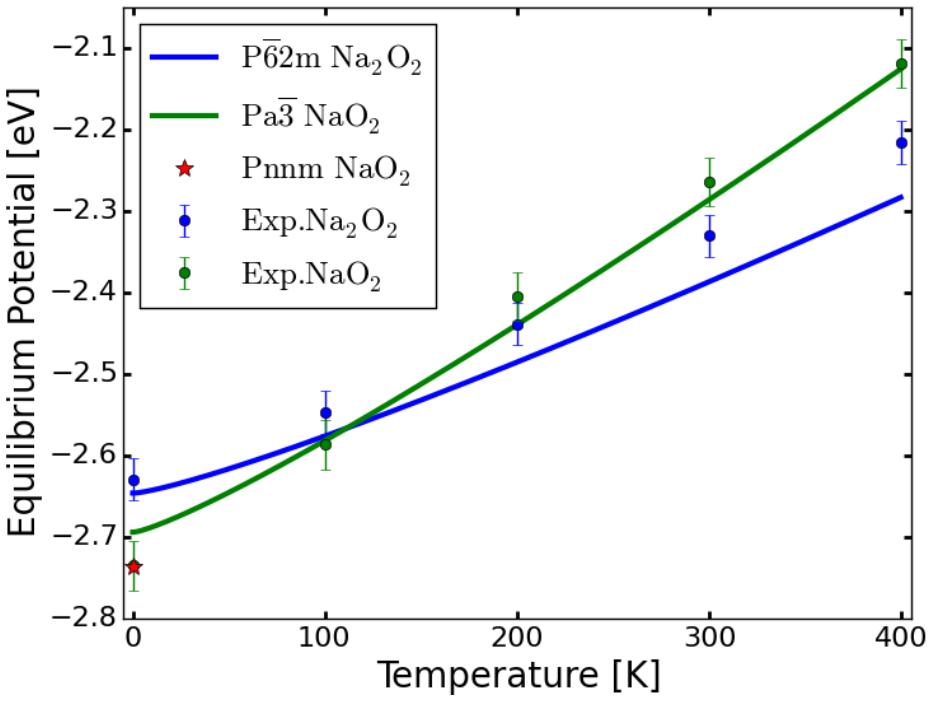

Figure 5.2: DFT-based equilibrium potentials predicted with the approximation that the temperature dependence is only due to the translational and rotational degrees of freedom for O_2(g). This simple approximation is in good alignment with experimental data and reproduces relatively small free energy differences between Na_2O_2 and NaO_2.

As seen in Table 5.1, the difference in equilibrium potential for NaO_2 and Na_2O_2 at standard conditions is less than 0.1 eV, for purely experimental results, calculated enthalpies with experimental entropies, and purely theoretical calculations with approximated entropies. This indicates that required overpotentials in electrochemical reactions to Na_2O_2 and NaO_2 could be decisive for the product formation.

Table 5.1: Calculations for Na_2O_2 and the pyrite phase of NaO_2 are compared with experimental values [89] in parentheses. Equilibrium potentials are calculated both using experimental entropies and with the approximation that all temperature dependence is due to translational and rotational degrees of freedom of O_2(g).

	$\Delta_f H°$ (eV)	Equil. Pot. (eV) (experimental ΔS)	Equil. Pot. (eV) (approximation)
$\mathbf{Pa\bar{3}\ NaO_2}$	**-2.74 (-2.71)**	**-2.30 (-2.27)**	**-2.29 (-2.27)**
$\mathbf{P\bar{6}2m\ Na_2O_2}$	**-5.29 (-5.32)**	**-2.39 (-2.33)**	**-2.39 (-2.33)**

In general, the NaCl-correction scheme has improved the understanding of this system and similarly why only including the translational O_2 contributions is a simple and reasonable way to estimate the temperature dependence of the NaO_2 to Na_2O_2 transition.

5.4 Reaction Mechanism Studies on NaO_2 and Na_2O_2 Step Surfaces

For the free energy calculations, we calculate the translational contributions to the entropy and enthalpy (through the heat capacity) for O_2 in the gas phase at STP and the difference in the rotational contribution between Na_2O_2 and NaO_2/O_2, where the O_2^{2-} species are constrained whereas the O_2^- and O_2(g) species are effectively free rotors at STP. To a first approximation, we only include these contributions, since the vibrational properties of O_2(g), O_2^- and O_2^{2-} are very similar and expected to cancel, and the rotational properties of O_2(g) and O_2^- ions are equally similar and expected to cancel.

The computational sodium electrode approach is used in the free energy calculations, analogous to the lithium electrode approach used for Li-Air batteries.[65],[88] Defined as, $U = 0$, when bulk Na anode and Na ions in solution ($Na^+ + e^-$) are at equilibrium. The free energy change of the reaction

is shifted by $-neU$ at an applied bias, where n is the number of electrons. From Hummelshøj *et al*. reports kinks and step surfaces are favorable nucleation sites for low overpotential reaction mechanisms. [64]

At neutral bias all reaction steps are downhill, but at an applied potential, the free energy difference changes for each step calculated from equation (4.1).

The limiting discharge potential ($\mathrm{U_{discharge}}$) is the lowest free energy step, $\Delta \mathrm{G_{min}}$, along the reaction path which becomes uphill at an applied potential. Likewise, the largest free energy step, $\Delta G_{i,max,}$ that is last to become downhill for the reversed reaction at an applied potential called limited charge potential ($\mathrm{U_{charge}}$) obtained from equation (4.2). The calculated effective equilibrium potential can be obtained as $\mathrm{U_o} = -\Delta \mathrm{G}/ne$. All reaction steps are downhill at neutral bias, however at an applied potential, the free energy difference changes for each step calculated from equation (1), where n is the number of electrons.

Systematic errors in description of superoxides, peroxides and monoxides have previously been documented by various groups and accounted for in various ways [64],[109],[113]. Here, we adopt the approach of Christensen *et al*.[113] using NaCl as reference to obtain the metallic Na energy. In line with Christensen *et al*.[113] an energy correction is applied to O_2(g), which is notoriously difficult to describe correct with DFT. With the used computational code the optimal energy correction of O_2(g) is -0.33 eV. The used approach is chosen as it reduces the systematic errors significantly, while allowing consistent calculation of surfaces with various oxide species present required for studying reactions in Na-O_2 batteries.

5.4.1 NaO_2 Growth/desorption Mechanisms on Selected Step Surfaces

The four steps NaO_2 growth/depletion is investigated on stepped (001) and (100) $\mathrm{NaO_2}$ surface. The method does not include specific effects of the electrolyte or possible kinetic barriers. DFT calculations can estimate the preferred pathways for the dis/charge mechanisms comparing the energies of the adsorbed species at every single step. The stepped surface is constructed manually from the bulk crystal in a specific direction in such a way that four sodium superoxide species are added (removed) at the step site for the complete pathways of growth (depletion).

In general, NaO_2 growth/depletion mechanisms on the step NaO_2 surfaces follows a four step mechanism; each step comprises of either Na* or NaO_2* species (electrochemical steps) or O_2

species (chemical step) and both are taken in to account to generate all possible pathways. Among which, the most thermodynamically favorable path with the low overpotential is selected. Thus, as shown in Figure 5.3a and Figure 5.4, the first step for (001) step surface is adsorption of the first NaO_2 on bottom left site, which is the limiting discharge potential (2.39 V) step and is followed by adsorption of the second NaO_2 species to the bottom right site with the binding energy of 2.57 V, the third and the fourth NaO_2 species are adsorbed by 2.63 V and 2.71 V, respectively, see Table 5.2. The fourth step is the limiting charge potential step and the growth mechanism is completed by forming 4 sodium superoxide species. The charging or desorption process follows the same reaction steps applied in reverse order (right to left), see Figure 5.3.

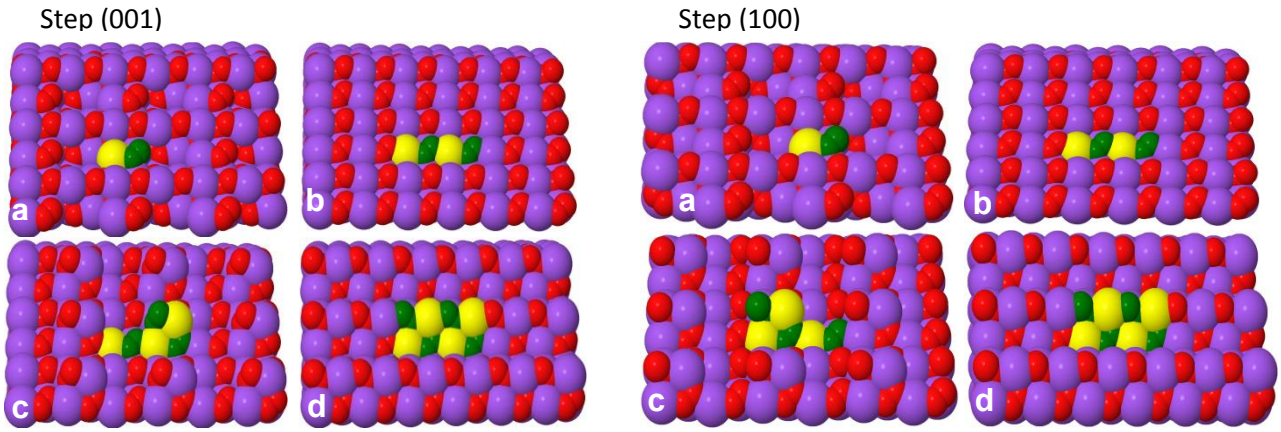

Figure 5.3: A 4 step growth/desorption mechanism on the step surface (001) and (100) of NaO_2. a) and b) NaO_2 adsorbs to the bottom site. c) and d) 2 NaO_2 adsorbs to the top site to complete the 4 formula units NaO_2 reaction mechanism. Color: Na purple and O red. Deposit atoms: Na yellow and O green.

Table 5.2: (Dis)/charge potentials and overpotentials (in V) estimated for NaO_2 growth/depletion mechanism studies on (001) and (100) step surfaces. Metallic Na energy is obtained from NaCl reference [113].

	Step (001)	Step (100)
$\mathbf{U_o}$	**2.57**	**2.56**
$\mathbf{U_{discharge}}$	**2.39**	**2.32**
$\mathbf{U_{charge}}$	**2.71**	**2.85**
$\mathbf{\eta_{discharge}}$	**0.18**	**0.28**
$\mathbf{\eta_{charge}}$	**0.14**	**0.28**

The growth/depletion mechanisms studies on the stepped NaO_2 surface revealed that the fundamental overpotentials in both discharge and charge processes are very low, which also has been experimentally observed [108]. Fundamentally, the overpotential in Li_2O_2 is also very low but experimentally different depending on the experimental conditions e.g. current density and parasitic chemistry.

Thus, the limiting discharge (charge) potential for the (001) stepped surface calculated using GGA is found to be 2.39 V (2.71 V) and the calculated effective equilibrium potential is 2.57 V (compared to the experimental value, $U_{0,Exp}$ = 2.27 V) leads discharge (charge) overpotential of 0.18 V (0.14 V) for the growth (depletion) mechanism, see Figure 5.4. The growth/desorption mechanisms studies on the stepped NaO_2 surface revealed that the fundamental overpotentials in both discharge and charge processes are very low which also has been experimentally observed [108]. Fundamentally, the overpotential in Li_2O_2 is also very low but experimentally different depending on the experimental conditions e.g. current density and parasitic chemistry. [64]

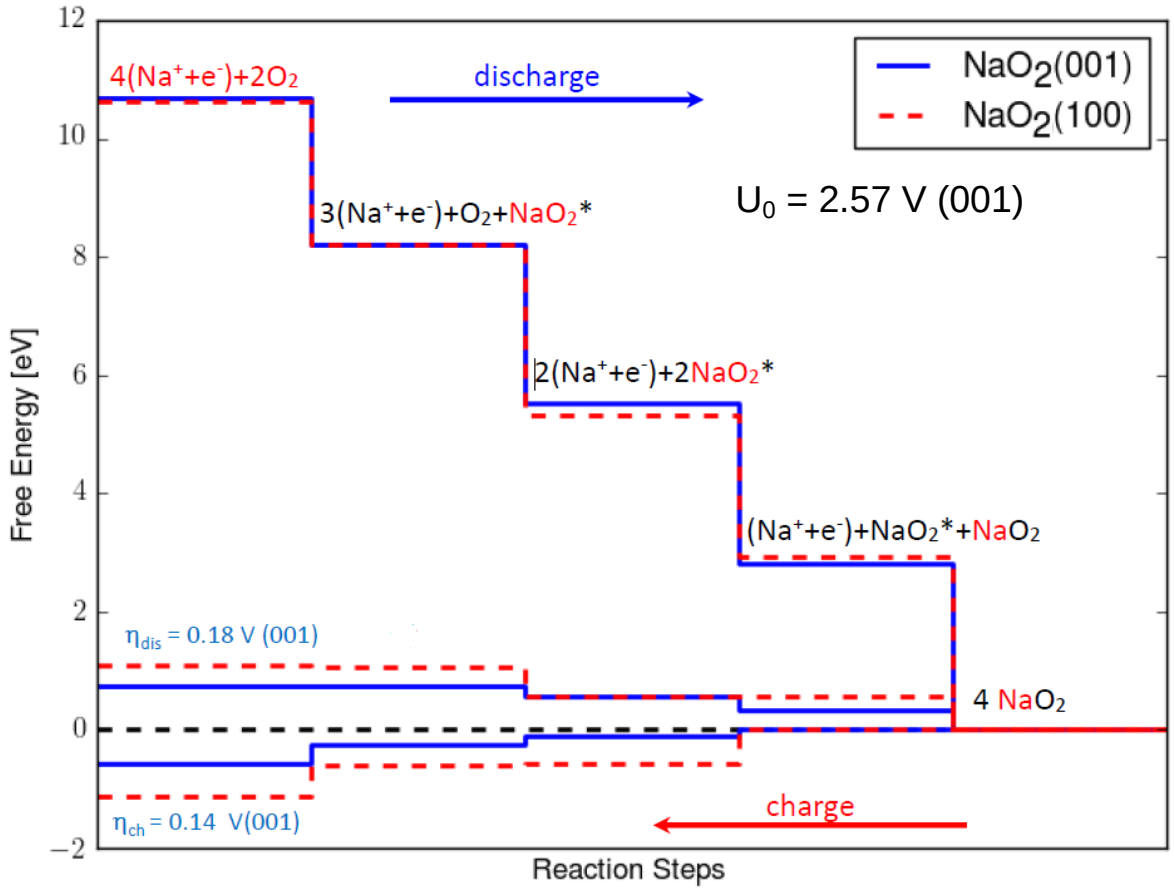

Figure 5.4: The calculated free energy diagram for NaO_2 growth/desorption mechanisms on stepped (001) and (100) NaO_2 surfaces using PBE.

Pathways involving a purely thermochemical step for O_2 ab/desorption are all found to be inactive due to high activation energy. The NaO_2 growth/depletion mechanism studies revealed a low overpotential path consists of four steps addition or removal of NaO_2 species electrochemically. The bulk equilibrium potential is in a good agreement with the experimental value of 2.27 V.

The NaO_2 growth/desorption mechanism studies revealed a low overpotential path consists of four electrochemical steps addition or removal of NaO_2 species. Pathways involving a purely thermodynamic step for O_2 ab/desorption are all found to be inactive due to high overpotentials. The bulk equilibrium potential is in a good agreement with the experimental value of 2.27 V however the surface equilibrium potential is off by 0.3 V compared to the bulk, it could be due to a variation in O-O bond length and magnetic moment at the surface and in bulk.

5.4.2 Na_2O_2 Growth/Desorption Mechanisms on $(1\bar{1}00)$ Step Surface

The free energy diagram in Figure 5.6 show four steps growth mechanism consists of two formula units of Na_2O_2 growth mechanism on the step $(1\bar{1}00)$ Na_2O_2 surface (from a to d). The first step adsorption of NaO_2* species (Fig. 5.5a) adsorbs with the binding energy by 1.89 V which is the potential limiting step for discharge. The next step is the addition of Na* species (Fig. 5.5b) adsorbed with the binding energy of 2.02 V. This is again followed by additions of NaO_2* and Na* respectively with the binding energies of 2.69 V and 2.15 V (the third step is potential limiting step for charge) (Fig. 5.5c and d). The full growth mechanism is accomplished with the two formula units of Na_2O_2 growth at the step surface with equilibrium potential of 2.19 V. The charging process follows the reverse order.

Previous work by Hummelshøj *et al*. [65] have reported that the pure Li_2O_2 growth mechanism follows 4 steps reaction mechanism, where all reaction steps are electrochemical. The equilibrium potential can be obtained as $U_0 = -\Delta G/2e$. The equilibrium potential of bulk Na_2O_2 is found to be 2.39 which is in good agreement with the experimental value of 2.33 V.

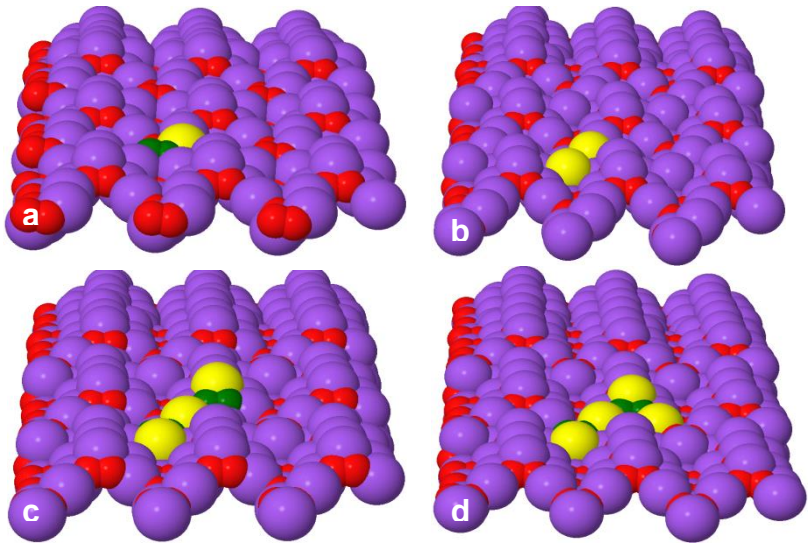

Figure 5.3: Figure 5: Reaction mechanism studies on stepped Na_2O_2 $(1\bar{1}00)$ surface follows 4 steps Na_2O_2 growth pathways during discharge. a) First NaO_2 adsorbs. d) Second NaO_2. c) First Li. f) Second Na adsorbs to the surface completing growth of 2 formula units of Na_2O_2. Atoms labeled as: Na purple and O red. Deposit atoms shown as: Na yellow and O green.

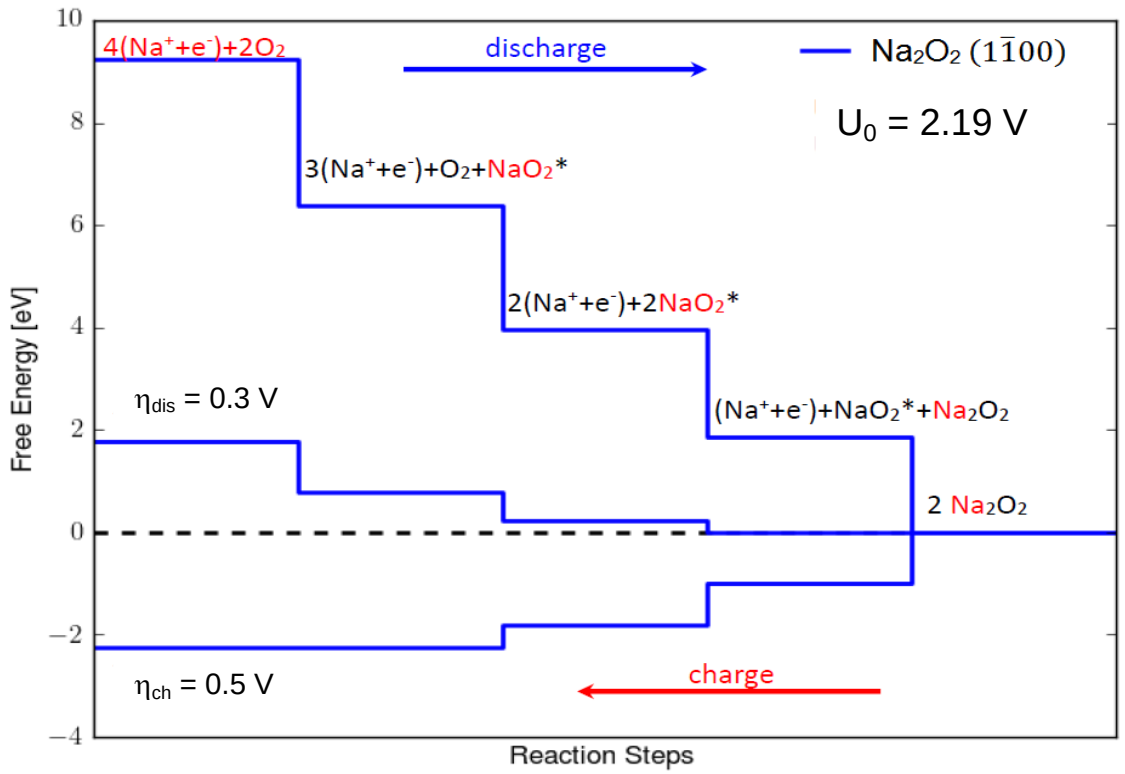

Figure 5.6: Calculated free energy diagrams for a four steps discharge mechanism from stepped $(1\bar{1}00)$ Na_2O_2 surface. The sodium metallic energy is obtained from NaCl reference.

A four steps reaction mechanism on stepped $(1\bar{1}00)$ Na_2O_2 surface were studied using DFT calculations. The Na_2O_2 growth mechanism consists of four electrochemical steps. The discharge occurs as described in Figure 5.5 and 5.6, among various paths the minimum low overpotential path resulting in discharge (charge) potential of 1.80 V (2.69 V) and overpotentials of 0.3 V (0.5 V). The preferred growth mechanism follows the following subsequent adsorption steps NaO_2*, Na*, NaO_2* and Na* respectively to form 2 formula units of Na_2O_2 at the step surface to complete the growth (* refers to surface adsorption). Here, the charging process follows the same reaction steps as discharging but in reverse (from d-a in Figure 5.5 and right to left in Figure 5.6). Pathways involving a purely thermochemical step for O_2 ab/desorption are all found to be inactive due to high overpotential. In general, the DFT calculations and few experimental results show that, the Na_2O_2 reaction mechanism has high overpotentials compared to low overpotential paths in NaO_2 formation.

5.5 Ionic Conduction in NaO_2

Activation energies for the dominant charge carrier in NaO_2, *i.e.* negative sodium vacancy (missing Na^+), were evaluated. We apply the vacancy mediated ionic charge carrier transport using -1 compensating back ground charge. As shown in Figure 5.8, results revealed that the sodium ion diffusion can take place at low activation energy barrier close to ~0.4 eV for intralayer diffusion channels and ~0.6 eV of activation barrier is estimated for interlayer diffusion pathway. The microscopic diffusion mechanism along the intralayer directions diffuse through the face center (follow zigzag pathways). Thus, the microscopic diffusion channel follows $\mathrm{A} \rightarrow \mathrm{C} \rightarrow \mathrm{X}$ series along the X- and $\mathrm{A} \rightarrow \mathrm{C} \rightarrow \mathrm{Y}$ in the Y-directions. Regarding the interlayer diffusion (in Z direction), the minimum interlayer diffusion barrier AZ(Z) path is about 0.58 eV. For the detail charge carrier transport in NaO_2 and Na_2O_2, refer [111].

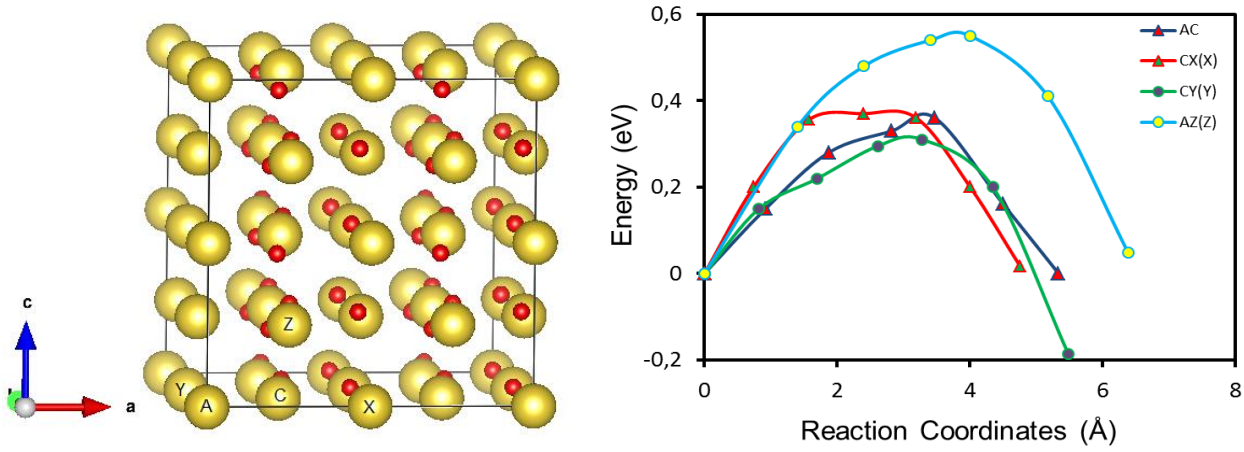

Figure 5.4: Na ion diffusion activation barrier along X, Y and Z directions in NaO_2 estimated using NEB method in PBE functional at -1 compensating background charge. The minimum activation energy barrier is found to be 0.40 eV and 0.58 eV along the intra and interlayer diffusion channels, respectively.

We can conclude that sodium ion diffusion in NaO_2 has a preferential channel along the intralayer channels, and this relatively small barrier could open the possibility of ionic conduction at ambient conditions. Thus, the ionic charge carrier transport in NaO_2 is not limiting.

5.6 Ionic Conduction in Na_2O_2

In order to investigate the dominant charge carrier transport (Na^+) in Na-O_2 battery we have used the $2 \times 2 \times 2$ supercell of hexagonal Na_2O_2 which consists of a total of 96 atoms and yields a total vacancy concentration [$V_{Li}^{'}$] of 2 %. The activation energy of the Na^+ diffusion along all the three directions are estimated using the climbing image nudge elastic band method as it is described in section (2.3). The calculations are performed introducing -1 compensating back ground charge. Accordingly, as shown in Figure 5.9 the interlayer diffusion channel OZ (Z) is the minimum energy barrier, note that similar behavior is observed in the case of Li_2O_2. Along the intralayer in X direction the activation barrier id found to be ~1.0 eV, thus it is inaccessible at ambient conditions. However, unlike to that of Li_2O_2 where intralayer ionic conduction is limiting, in Na_2O_2 we found a minimum barrier along the intralayer in Y direction; see the OY (Y) path which is less than 0.5 eV. Therefore, we can conclude that ionic diffusion in Na_2O_2 is also not the limiting process like that of in NaO_2.

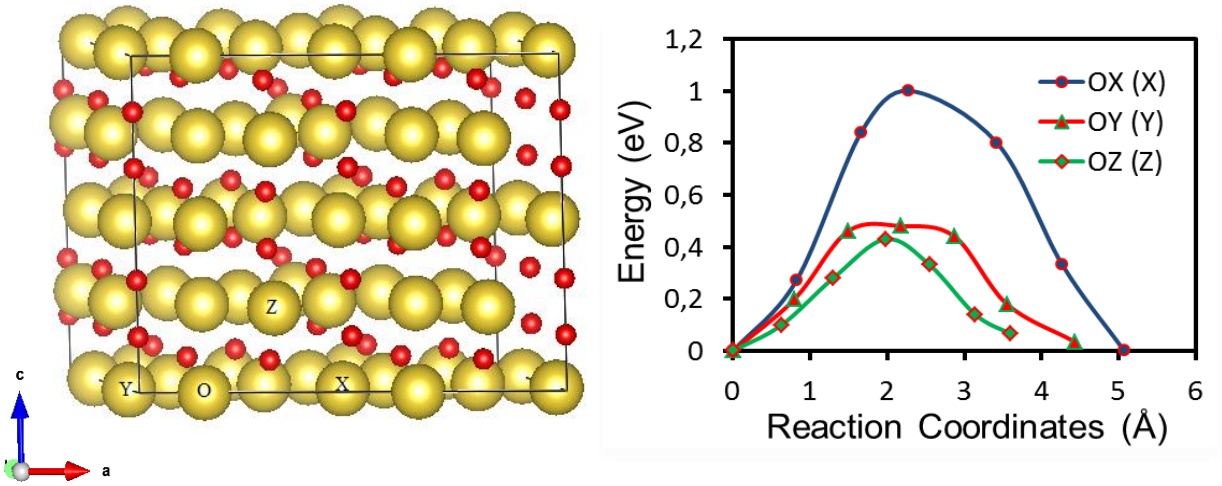

Figure 5.5: Na ion diffusion paths in Na_2O_2 obtained using PBE. The minimum energy barrier estimated along the X, Y and Z directions are ~ 1.0, 0.5 and 0. 4 eV, respectively.

5.7 Polaronic Conduction in Na_2O_2

We have used DFT+U method to investigate the polaron conduction in Na_2O_2 Hole polaron is localized at one of the O-O bond of the peroxide where the bond length is reduced by 0.22 Å (from 1.56 Å to 1.33 Å). Likewise, the excess electron is localized by stretching the bond length from 1.56 Å to 2.45 Å. In both cases localization involve an entire geometry distortion apart from change in bond length of one of the peroxide ion. The total magnetic moment that appeared in a single oxyanions is 1 in both hole and electron. The localized states are more stable than that of the delocalized ones particularly the excess electron polaron offer strong stability over the delocalized states.We have found that Na_2O_2 can hold excess electron polarons. However, the migration barriers for electron polarons are higher than the ones of hole polarons 1.5 eV.

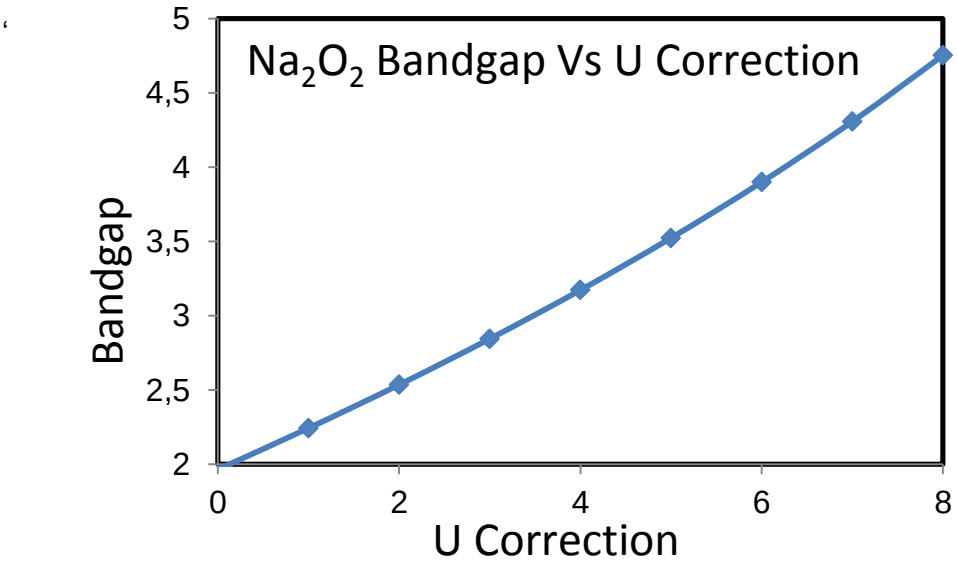

Figure 5.6: The DFT (Kohn-Sham) bandgap of bulk **Na_2O_2** as a function of Hubbard's correction (U), the U value opens the bandgap above 4 eV is beyond U = 6 eV.

Polaronic conduction in Na_2O_2 is also studied and will be discussed in this section. Intralayer and interlayer hops for both electron and hole polarons studies are explored. In many cases, Na_2O_2 exhibits almost similar properties as Li_2O_2. It displays low hole polaron hopping barriers and significantly high excess electron hopping barrier. Thus, hole polaron transport mechanism in Na_2O_2 could be an alternative path for fast electronic transport. Almost similar results are recently reported by Yang *et al,* [111].

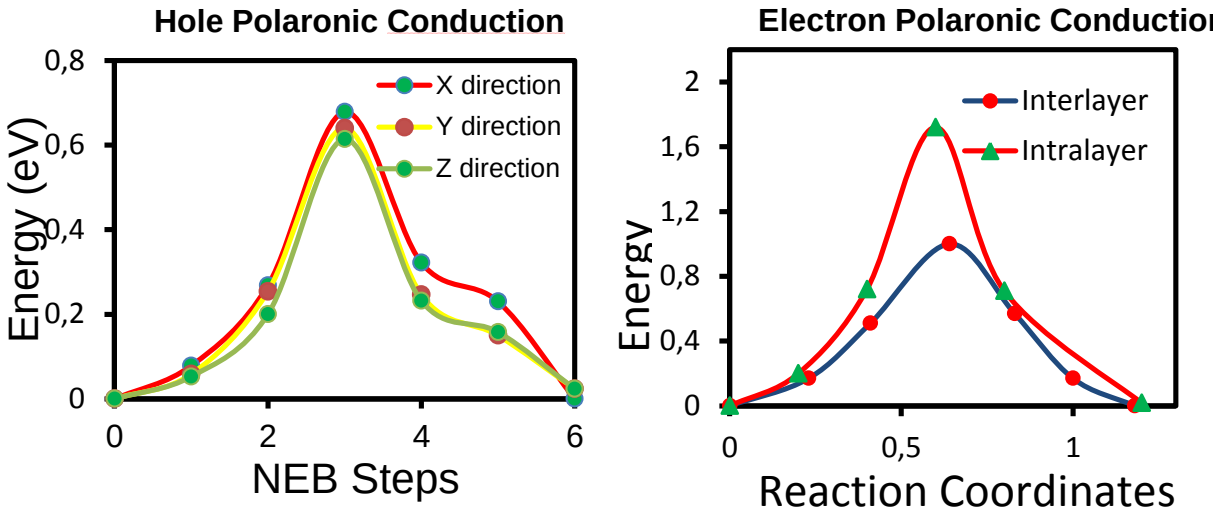

Figure 5.7: Hole and Electron polaron hopping in Na_2O_2 using PBE+U (at U = 6 eV).

5.8 Summary of Na-O_2 Studies

In this section I would like to summarize the main outcomes of the reaction mechanism studies on some selected step surfaces, as well as charge transport in NaO_2 and Na_2O_2. We have presented the fundamental investigation in the materials of Na–O_2 system. This technology holds great potential as a low cost and high energy density battery. To summarize the DFT calculations, equilibrium potentials and free energies as a function of temperature for different phases of NaO_2 and Na_2O_2, using an improved metal chloride correction scheme, showing cubic $Pa\bar{3}$ NaO_2 to be the thermodynamically preferred discharge product up to 223 K, after which Na_2O_2 is thermodynamically preferred. Regarding the charge transport studies in NaO_2 and Na_2O_2 bulk, we found that the negative sodium (Na^+ missing) transport is taking place at an accessible energy barrier at the battery operation conditions (< 0.5 eV). Moreover, hole polaron hops are also taking place at low energy barrier in Na_2O_2.

Furthermore, the reaction mechanism studies on stable step surfaces $(1\bar{1}00)$ facet in Na_2O_2 and (001) and (100) facets in NaO_2 showing low overpotentials for NaO_2 formation (< 0.2 V) and high discharge (charge) overpotentials of 0.3 V(0.5 V) for Na_2O_2, which is excellent agreement with experiments. These findings provide the first kinetic explanation for why NaO_2 is the main discharge product in Na-O_2 batteries under normal operating conditions (Paper III).

CHAPTER 6

Summary and Outlook

In previous chapters I have presented the results of my research during the last three years. The three topics covered in the thesis were presented separately in different chapters. A summary of the main findings is included at the end of each chapter. Here I will not repeat the summaries, but I will outline what I consider to be the highlights. A brief outlook of the thesis is included at the end.

6.1 Summary of the main results

During my Ph.D. thesis, I have carried out theoretical investigations based on DFT calculations about the growth mechanisms and charge transport processes in the discharge product materials of Li-O_2 and Na-O_2 batteries. The main outcome of this work can be summarized as follows:

1. It was shown that the detailed understanding of charge transport across the Li_2O_2@Li_2CO_3 interfaces can shed new light on the limited performance of aprotic Li-O_2 batteries. Our calculation pointed out that Li vacancies are prone to trapping at the peroxide part of interface based on the relative vacancy formation energies. This leads to substantial reduction in the coherent transport. Remarkably, low electron polaron hopping barriers are found in the plane of the interface which does not exist in the bulk of either Li_2O_2 not Li_2CO_3.
2. We explained the impact of carbonate species originating from reactions between CO_2 and Li_2O_2 at the cathode of Li-air batteries on the overpotentials of the battery. It was shown that, even at low concentrations, CO_2 effectively blocks the step nucleation site and alters the Li_2O_2 shape due to Li_2CO_3 formation. The calculations showed that once CO_2 is adsorbed on a step valley site, it is effectively unable to diffuse and hinders the Li_2O_2 growth mechanism, reducing the capacity and increasing the overpotentials of the battery. This effect, predicted from DFT calculations, was confirmed experimentally, already at 1 % CO_2 concentration in the air.

3. Using an improved metal chloride correction scheme, we calculated cubic NaO_2 to be the thermodynamically preferred discharge product in Na-O_2 batteries up to 223 K, after which Na_2O_2 is thermodynamically preferred. Despite of this, the experimentally observed discharge product at room temperature is NaO_2. We showed that this is due to the kinetics of the formation processes of Na_2O_2 which exhibits overpotentials above 0.5 V, while for NaO_2 the overpotentials are smaller than 0.2 V.

6.2 Outlook

From these summarized calculations we can envisage some future lines of work, both from the modeling and experimental point of view. Here I have gathered five ideas at this respect:

1. Our prediction of good electron polaron conductivities at Li_2O_2@Li_2CO_3 interfaces could lead to the experimental design of nanostructured cathodes with graphene nanopillars to improve the capacity of Li-O_2 batteries. In these structure it would be possible to alternate between electrochemical discharge (leading to Li_2O_2 formation), and short rest periods allowing some level of chemical degradation to form Li_2CO_3 inclusions. This should allow the formation of a sufficient number of Li_2O_2@Li_2CO_3 interfaces capable of supplying the required electronic conduction to fill the space between the nanopillars.
2. The poisoning of other species different that of CO_2, e.g. nitrogen or water from the air, could also have an impact on the overpotential and capacity of the Li-O_2 battery. Thus, it would recommend carrying out DFT calculations about the interaction of Li_2O_2 surfaces with these new species.
3. Many of the calculations performed in this thesis rely on DFT+U method. Typically the U value in the DFT+U approximation is chosen in such a way that the experimental bandgap of material is reproduced. However, the experimental data about bandgaps of superoxides and peroxides of alkali ions is scarce or inexistent. In many cases bandgaps from high-level calculations, e.g. GW calculations, is taken as a reference. However, the GW techniques results, although much more accurate than conventional DFT results, do not always agree with the experimental figures. For this reason it would be very valuable to conduct photoemission and inverse photoemission experiments on these materials in order to get their bandgaps.

4. There is a significant amount of theoretical studies about Li-O_2 batteries in the literature, while there are only a few of Na-O_2 batteries. Thus, there are still several aspects of NaO_2 and Na_2O_2 materials in which DFT simulations could help to shed light on. Here I give one example: We mentioned in chapter 5 that superoxide ions in NaO_2 are freely rotating in the high-temperature pyrite phase. However, these rotations affect to the electronic properties of the material (*i.e.* bandgap or diffusion barriers for polarons) is a question that remains open.
5. A natural continuation of this work would be to investigate other interfaces that occur both at the anode and cathode sides of the battery. Ideally these new investigations should combine computational studies and experiments. From the computational point of view it would be recommendable to use methods such as Montecarlo simulations to study the interaction between the electrolyte and the discharge products.

Bibliography

[1] R. Jones, “Energy Poverty: How to make modern energy access universal?,” *Spec. early excerpt World Energy Outlook*, no. September, p. 52, 2010.

[2] T. Foley, K. Thornton, R. Hinrichs-rahlwes, S. Sawyer, M. Sander, R. Taylor, S. Teske, H. Lehmann, M. Alers, and D. Hales, *Renewables 2015 global status report*. 2015.

[3] Sfoe, “Energy Strategy 2050,” *Http://Www.Bfe.Admin.Ch/Themen/00526/00527/*, no. February, 2014.

[4] Ipcc, “Summary for Policy Makers,” *Clim. Chang. 2014 Impacts, Adapt. Vulnerability - Contrib. Work. Gr. II to Fifth Assess. Rep.*, pp. 1–32, 2014.

[5] IEA, “Energy and climate change,” 2015.

[6] Ipcc, “Summary for Policymakers,” *Ipcc Wgiii Ar5*, pp. 1–33, 2014.

[7] B. Nykvist and M. Nilsson, “Rapidly falling costs of battery packs for electric vehicles,” *Nat. Clim. Chang.*, vol. 5, no. April, pp. 329–332, 2015.

[8] M. S. Whittingham, *Chemistry of intercalation compounds: Metal guests in chalcogenide hosts*, vol. 12, no. 1. 1978.

[9] F. O. R. Batteries, O. F. High, and E. Density, “LixCoO2 (0<x≤1): a new cathode material for batteries of high energy density,” *Solid State Ionics*, vol. 4, pp. 171–174, 1981.

[10] M. M. Thackeray, C. Wolverton, and E. D. Isaacs, “Electrical energy storage for transportation—approaching the limits of, and going beyond, lithium-ion batteries,” *Energy Environ. Sci.*, vol. 5, no. 7, p. 7854, 2012.

[11] P. G. Bruce, S. A. Freunberger, L. J. Hardwick, and J. M. Tarascon, “Li–O2 and Li–S batteries with high energy storage,” *Nat. Mater.*, vol. 11, no. December 2011, pp. 19–30, 2012.

[12] J.-S. Lee, S. Tai Kim, R. Cao, N.-S. Choi, M. Liu, K. T. Lee, and J. Cho, “Metal-Air Batteries with High Energy Density: Li-Air versus Zn-Air,” *Adv. Energy Mater.*, vol. 1, no. 1, pp. 34–50, Jan. 2011.

[13] M. S. Whittingham, *Metal-Air Batteries: A Reality Check. Meeting Abstract*. 2012, p. 1099.

[14] D. Linden and T. B. Reddy, *HANDBOOK OF BATTERIES*. .

[15] M. Balaish, A. Kraytsberg, and Y. Ein-Eli, “A critical review on lithium-air battery electrolytes.,” *Phys. Chem. Chem. Phys.*, vol. 16, pp. 2801–2822, Feb. 2014.

[16] M. Armand and J. M. Tarascon, “Building better batteries,” *Nature*, vol. 451, pp. 652–657, Feb. 2008.

[17] J. Hojberg, K. B. Knudsen, J. Hjelm, and T. Vegge, “Reactions and SEI Formation during Charging of Li-O2 Cells,” *ECS Electrochem. Lett.*, vol. 4, pp. A63–A66, 2015.

[18] A. C. Luntz and B. D. Mccloskey, “Nonaqueous Li − Air Batteries : A Status Report,” 2013.

[19] N. Zhao, C. Li, and X. Guo, “Long-life Na-O_2 batteries with high energy efficiency enabled by electrochemically splitting NaO_2 at a low overpotential.,” *Phys. Chem. Chem. Phys.*, vol. 16, no. 29, pp. 15646–52, Aug. 2014.

[20] P. Hartmann, C. L. Bender, M. Vračar, A. K. Dürr, A. Garsuch, J. Janek, and P. Adelhelm, “A rechargeable room-temperature sodium superoxide (NaO2) battery.,” *Nat. Mater.*, vol. 12, no. 3, pp. 228–32, Mar. 2013.

[21] P. Hohenberg and W. Kohn, “Inhomogeneous electron gas,” *Phys. Rev. B*, vol. 136, no. 3B, pp. B864–B871, 1964.

[22] W. Kohn and L. J. Sham, “Self-Consistent Equation Including Exchange and Correlation Effects,” *Phys. Rev.*, vol. 140, p. A 1133–A 1138, 1965.

[23] S. L. Dudarev, S. Y. Savrasov, C. J. Humphreys, and a. P. Sutton, “Electron-energy-loss spectra and the structural stability of nickel oxide: An LSDA+U study,” *Phys. Rev. B*, vol. 57, no. 3, pp. 1505–1509, 1998.

[24] J. Enkovaara, C. Rostgaard, J. J. Mortensen, J. Chen, M. Dułak, L. Ferrighi, J. Gavnholt, C. Glinsvad, V. Haikola, H. a Hansen, H. H. Kristoffersen, M. Kuisma, a H. Larsen, L. Lehtovaara, M. Ljungberg, O. Lopez-Acevedo, P. G. Moses, J. Ojanen, T. Olsen, V. Petzold, N. a Romero, J. Stausholm-Møller, M. Strange, G. a Tritsaris, M. Vanin, M. Walter, B. Hammer, H. Häkkinen, G. K. H. Madsen, R. M. Nieminen, J. K. Nørskov, M. Puska, T. T. Rantala, J. Schiøtz, K. S. Thygesen, and K. W. Jacobsen, “Electronic structure calculations with GPAW: a real-space implementation of the projector augmented-wave method.,” *J. Phys. Condens. Matter*, vol. 22, p. 253202, Jun. 2010.

[25] M. Brandbyge, J.-L. Mozos, P. Ordejón, J. Taylor, and K. Stokbro, “Density-functional method for nonequilibrium electron transport,” *Phys. Rev. B*, vol. 65, p. 165401, Mar. 2002.

[26] M. Ernzerhof and G. E. Scuseria, “Perspective on ‘Inhomogeneous electron gas,’” *Theor. Chem. Acc.*, vol. 103, pp. 259–262, Feb. 2000.

[27] D. M. Ceperley and B. J. Alder, “Ground state of the electron gas by a stochastic method,” *Phys. Rev. Lett.*, vol. 45, no. 7, pp. 566–569, 1980.

[28] J. P. Perdew and A. Zunger, “Self-interaction correlation to density-functional approximations for many-electron systems,” *Phys. Rev. B*, vol. 23, no. 10, pp. 5048–5079, 1981.

[29] S. H. Vosko, L. Wilk, and M. Nusair, “Accurate spin-dependent electron liquid correlation energies for local spin density calculations: a critical analysis,” *Can. J. Phys.*, vol. 58, no. 8, pp. 1200–1211, 1980.

[30] J. Perdew, J. Chevary, S. Vosko, K. Jackson, M. Pederson, D. Singh, and C. Fiolhais, “Erratum: Atoms, molecules, solids, and surfaces: Applications of the generalized gradient approximation for exchange and correlation,” *Phys. Rev. B*, vol. 48, no. 7, pp. 4978–4978, 1993.

[31] J. P. Perdew, K. Burke, M. Ernzerhof, D. of Physics, and N. O. L. 70118 J. Quantum Theory Group Tulane University, “Generalized Gradient Approximation Made Simple,” *Phys. Rev. Lett.*, vol. 77, no. 18, pp. 3865–3868, 1996.

[32] B. Hammer, L. Hansen, and J. Nørskov, “Improved adsorption energetics within density-functional theory using revised Perdew-Burke-Ernzerhof functionals,” *Phys. Rev. B*, vol. 59, pp. 7413–7421, Mar. 1999.

[33] T. Vegge, T. Rasmussen, T. Leffers, O. Pedersen, and K. Jacobsen, “Determination of the of rate cross slip of screw dislocations,” *Phys. Rev. Lett.*, vol. 85, pp. 3866–3869, Oct. 2000.

[34] H. Jonsson, G. Mills, and K. W. Jacobsen, “Nudged elastic band method for finding minimum energy paths of transitions,” in *Classical and Quantum Dynamics in Condensed Phase Simulations (edited by B. J. Berne, G. Ciccotti, D. F. Coker (World Scientific, Singapore, 1998)*, pp. 385–404.

[35] G. Henkelman and H. Jonsson, “Improved tangent estimate in the nudged elastic band method for finding minimum energy paths and saddle points,” *J. Chem. Phys.*, vol. 113, pp. 9978–9985, 2000.

[36] B. P. U. Graeme Henkelman Hannes Jonsson, “ A climbing image Nudge elastic band methos for finding saddle points and minimum energy paths,” *J. Chem. Phys.*, vol. 113, no. 113, 2000.

[37] Atomistix ToolKit version 2014.1, QuantumWise A/S (www.quantumwise.com).

[38] J. M. Soler, E. Artacho, J. D. Gale, A. Garcia, J. Junquera, P. Ordejon, and D. Sanchez-Portal, “The SIESTA method for ab initio order-N materials simulation,” *J. Phys. Condens. Matter*, vol. 14, pp. 2745–2779, 2002.

[39] J. J. Mortensen, L. B. Hansen, and K. W. Jacobsen, “A real-space grid implementation of the Projector Augmented Wave method,” *Phys. Rev. B*, vol. 71, p. 035109, Nov. 2005.

[40] P. E. Blochl, “Projected augmented-wave method,” *Phys. Rev. B*, vol. 50, pp. 17953–17979, 1994.

[41] S. R. Bahn and K. W. Jaconsen, “An Object-Oriented Scripting Interface to a Legacy Electronic Strcture Code,” *Comput. Sci. Eng.*, vol. 4, pp. 56–66, 2002.

[42] J. M. Tarascon and M. Armand, “Issues and challenges facing rechargeable lithium batteries.,” *Nature*, vol. 414, pp. 359–67, Nov. 2001.

[43] K. M. Abraham, Z. Jiang, and J. E. Soc, “A Polymer Electrolyte − Based Rechargeable Lithium / Oxygen Battery TECHNICAL PAPERS ELECTROCHEMICAL SCIENCE AND TECHNOLOGY A Polymer Electrolyte-Based Rechargeable lithium / Oxygen Battery,” vol. 143, no. 1, pp. 1–5, 1996.

[44] T. Ogasawara, A. Débart, M. Holzapfel, P. Novák, and P. G. Bruce, “Rechargeable LI_2O_2 electrode for lithium batteries.,” *J. Am. Chem. Soc.*, vol. 128, pp. 1390–3933, Feb. 2006.

[45] G. Girishkumar, B. McCloskey, a. C. Luntz, S. Swanson, and W. Wilcke, “Lithium−Air Battery: Promise and Challenges,” *J. Phys. Chem. Lett.*, vol. 1, no. 14, pp. 2193–2203, Jul. 2010.

[46] P. Albertus, G. Girishkumar, B. McCloskey, R. S. Sánchez-Carrera, B. Kozinsky, J. Christensen, and A. C. Luntz, “Identifying Capacity Limitations in the Li/Oxygen Battery Using Experiments and Modeling,” *J. Electrochem. Soc.*, vol. 158, pp. A343–A351, 2011.

[47] J. M. Garcia-Lastra, J. D. Bass, and K. S. Thygesen, “Communication: Strong excitonic and vibronic effects determine the optical properties of Li_2O_2,” *J. Chem. Phys.*, vol. 135, no. 12, pp. 3–7, 2011.

[48] V. Viswanathan, K. S. Thygesen, J. S. Hummelshøj, J. K. Nørskov, G. Girishkumar, B. D. McCloskey, and A. C. Luntz, “Electrical conductivity in Li_2O_2 and its role in determining capacity limitations in non-aqueous Li-O_2 batteries,” *J. Chem. Phys.*, vol. 135, p. 214704, Dec. 2011.

[49] J. Chen, J. S. Hummelshøj, K. S. Thygesen, J. S. G. Myrdal, J. K. Nørskov, and T. Vegge, “The role of transition metal interfaces on the electronic transport in lithium–air batteries,” *Catal. Today*, vol. 165, pp. 2–9, May 2011.

[50] B. D. Mccloskey, A. Speidel, R. Scheffler, D. C. Miller, V. Viswanathan, J. S. Hummelshøj, J. K. Nørskov, and A. C. Luntz, “Twin Problems of Interfacial Carbonate Formation in Nonaqueous,” *J. Phys. Chem. Lett.*, vol. 3, pp. 997–1001, 2012.

[51] J. M. Garcia-Lastra, J. S. G. Myrdal, R. Christensen, K. S. Thygesen, and T. Vegge, “DFT+U Study of Polaronic Conduction in Li2O2 and Li2CO3 : Implications for Li–Air Batteries,” *J. Phys. Chem. C*, vol. 117, pp. 5568–5577, Mar. 2013.

[52] J. B. Varley, V. Viswanathan, J. K. Nørskov, and a. C. Luntz, “Lithium and oxygen vacancies and their role in Li_2O_2 charge transport in Li–O_2 batteries,” *Energy Environ. Sci.*, vol. 7, pp. 720–727, 2014.

[53] A. C. Luntz, V. Viswanathan, J. Voss, J. B. Varley, and A. Speidel, “Tunneling and Polaron Charge Transport through Li_2O_2 in Li−O_2 Batteries,” pp. 2–7, 2013.

[54] M. D. Radin, C. W. Monroe, and D. J. Siegel, “How Dopants Can Enhance Charge Transport in Li_2O_2,” *Chem. Mater.*, vol. 27, no. 3, pp. 839–847, 2015.

[55] V. Timoshevskii, Z. Feng, and K. Bevan, “Improving Li_2O_2 conductance via polaron preemption : an ab initio study of Si doping,” 1800.

[56] M. D. Radin, J. F. Rodriguez, F. Tian, and D. J. Siegel, “Lithium peroxide surfaces are metallic, while lithium oxide surfaces are not.,” *J. Am. Chem. Soc.*, vol. 134, no. 2, pp. 1093–1103, Jan. 2012.

[57] B. D. McCloskey, R. Scheffler, A. Speidel, G. Girishkumar, and A. C. Luntz, “On the mechanism of nonaqueous Li-O_2 electrochemistry on C and its kinetic overpotentials: Some implications for Li-air batteries,” *J. Phys. Chem. C*, vol. 116, no. 45, pp. 23897–23905, 2012.

[58] C. O. Laoire, S. Mukerjee, K. M. Abraham, E. J. Plichta, and M. a. Hendrickson, “Elucidating the mechanism of oxygen reduction for lithium-air battery applications,” *J. Phys. Chem. C*, vol. 113, no. 46, pp. 20127–20134, 2009.

[59] Z. Peng, S. a. Freunberger, L. J. Hardwick, Y. Chen, V. Giordani, F. Bardé, P. Novák, D. Graham, J. M. Tarascon, and P. G. Bruce, “Oxygen reactions in a non-aqueous Li+ electrolyte,” *Angew. Chemie - Int. Ed.*, vol. 50, no. 28, pp. 6351–6355, 2011.

[60] L. G. Cota and P. De La Mora, “On the structure of lithium peroxide, Li_2O_2,” *Acta Crystallogr.*, vol. B61, pp. 133–136, 2005.

[61] M. . Nadler and C. P. Kempter, “Lithium,” *Anal. Chem.*, vol. 31, no. 12, pp. 2109–2109, 1959.

[62] A. Liu, A. Quong, J. Freericks, E. Nicol, and E. Jones, “Structural phase stability and electron-phonon coupling in lithium,” *Phys. Rev. B*, vol. 59, no. 6, pp. 4028–4035, 1999.

[63] M. D. Radin, F. Tian, and D. J. Siegel, “Electronic structure of Li_2O_2{0001} surfaces,” *J. Mater. Sci.*, vol. 47, pp. 7564–7570, May 2012.

[64] J. S. Hummelshøj, a C. Luntz, and J. K. Nørskov, “Theoretical evidence for low kinetic overpotentials in Li-O_2 electrochemistry.,” *J. Chem. Phys.*, vol. 138, p. 034703, Jan. 2013.

[65] J. S. Hummelshøj, J. Blomqvist, S. Datta, T. Vegge, J. Rossmeisl, K. S. Thygesen, a C. Luntz, K. W. Jacobsen, and J. K. Nørskov, “Communications: Elementary oxygen electrode reactions in the aprotic Li-air battery.,” *J. Chem. Phys.*, vol. 132, no. 7, p. 071101, Feb. 2010.

[66] Y. S. Mekonnen, K. B. Knudsen, J. S. G. Mýrdal, R. Younesi, J. Højberg, J. Hjelm, P. Norby, and T. Vegge, “Communication: The influence of CO2 poisoning on overvoltages and discharge capacity in non-aqueous Li-Air batteries,” *J. Chem. Phys.*, vol. 140, p. 121101, Mar. 2014.

[67] J. S. G. Mýrdal and T. Vegge, “Selective poisoning of Li–air batteries for increased discharge capacity,” *RSC Adv.*, vol. 4, no. 30, p. 15671, 2014.

[68] M. D. Radin and D. J. Siegel, “Charge transport in lithium peroxide: relevance for rechargeable metal–air batteries,” *Energy Environ. Sci.*, vol. 6, pp. 2370–2379, 2013.

[69] Y. S. Mekonnen, J. M. Garcia-Lastra, J. S. Hummelshøj, C. Jin, and T. Vegge, “Role of Li_2O_2 @Li_2CO_3 Interfaces on Charge Transport in Non-Aqueous Li-Air Batteries,” *J. Phys. Chem. C*, vol. 119, no. 32, pp. 18066–18073, 2015.

[70] J.-G. Zhang, D. Wang, W. Xu, J. Xiao, and R. E. Williford, “Ambient operation of Li/Air batteries,” *J. Power Sources*, vol. 195, no. 13, pp. 4332–4337, Jul. 2010.

[71] J. Zhang, W. Xu, X. Li, and W. Liu, “Air Dehydration Membranes for Nonaqueous Lithium–Air Batteries,” *J. Electrochem. Soc.*, vol. 157, no. 8, p. A940, 2010.

[72] S. R. Gowda, A. Brunet, and B. D. Mccloskey, “Implications of CO_2 Contamination in Rechargeable Nonaqueous Li −,” pp. 2–5, 2013.

[73] B. D. Mccloskey, R. Sche, A. Speidel, G. Girishkumar, and A. C. Luntz, “On the Mechanism of Nonaqueous Li−O_2 Electrochemistry on C and Its Kinetic Overpotentials : Some Implications for Li−Air Batteries,” *J. Phys. Chem. C*, 2012.

[74] E. L. Littauer and K. C. Tsai, “Corrosion of Lithium in Alkaline Solution,” *Electrochem. Sci. Technol.*, vol. 124, pp. 850–855, 1977.

[75] L. O. L. Crystallization, R. Black, S. H. Oh, J. Lee, T. Yim, B. Adams, and L. F. Nazar, “Screening for Superoxide Reactivity in Li-O 2 Batteries : Effect on,” 2012.

[76] R. Black, B. Adams, and L. F. Nazar, “Non-Aqueous and Hybrid Li-O_2 Batteries,” *Adv. Energy Mater.*, vol. 2, no. 7, pp. 801–815, Jul. 2012.

[77] R. Younesi, M. Hahlin, F. Bjorefors, P. Johansson, and K. Edstrom, “Li−O_2 Battery Degradation by Lithium Peroxide (Li2O2): A Model Study,” *Chem. Mater.*, 2013.

[78] R. Younesi, P. Norby, and T. Vegge, “A New Look at the Stability of Dimethyl Sulfoxide and Acetonitrile in Li-O_2 Batteries,” *ECS Electrochem. Lett.*, vol. 3, no. 3, pp. A15–A18, 2014.

[79] Y. Chen, S. A. Freunberger, Z. Peng, F. Barde, and P. G. Bruce, “Li−O_2 Battery with a Dimethylformamide Electrolyte,” pp. 2–7, 2012.

[80] J. Lu and K. Amine, “Recent Research Progress on Non-aqueous Lithium-Air Batteries from Argonne National Laboratory,” *Energies*, vol. 6, no. 11, pp. 6016–6044, Nov. 2013.

[81] J. Read, “Characterization of the Lithium/Oxygen Organic Electrolyte Battery,” *J. Electrochem. Soc.*, vol. 149, no. 9, p. A1190, 2002.

[82] J. Read, “Ether-Based Electrolytes for the Lithium/Oxygen Organic Electrolyte Battery,” *J. Electrochem. Soc.*, vol. 153, no. 1, p. A96, 2006.

[83] H.-D. Lim, K.-Y. Park, H. Gwon, J. Hong, H. Kim, and K. Kang, “The potential for long-term operation of a lithium-oxygen battery using a non-carbonate-based electrolyte.,” *Chem. Commun. (Camb).*, vol. 48, no. 67, pp. 8374–6, Aug. 2012.

[84] C. O. Laoire, S. Mukerjee, E. J. Plichta, M. a. Hendrickson, and K. M. Abraham, “Rechargeable Lithium/TEGDME-LiPF[sub 6]/O[sub 2] Battery,” *J. Electrochem. Soc.*, vol. 158, no. 3, p. A302, 2011.

[85] H.-K. Lim, H.-D. Lim, K.-Y. Park, D.-H. Seo, H. Gwon, J. Hong, W. a Goddard, H. Kim, and K. Kang, “Toward a lithium-‘air’ battery: the effect of CO2 on the chemistry of a lithium-oxygen cell.,” *J. Am. Chem. Soc.*, vol. 135, no. 26, pp. 9733–42, Jul. 2013.

[86] K. Takechi, T. Shiga, and T. Asaoka, “A Li-O_2/CO_2 battery.,” *Chem. Commun. (Camb).*, vol. 47, no. 12, pp. 3463–3465, 2011.

[87] V. Viswanathan, A. Speidel, S. Gowda, and A. C. Luntz, "Li−O_2 Kinetic Overpotentials: Tafel Plots from Experiment and First- Principles Theory," 2013.

[88] J. K. Nørskov, J. Rossmeisl, A. Logadottir, L. Lindqvist, D.- Lyngby, and H. Jo, "Origin of the Overpotential for Oxygen Reduction at a Fuel-Cell Cathode," pp. 17886–17892, 2004.

[89] Chase, M. W.; National Institute of, S.; Technology, NIST-JANAF thermochemical tables. American Chemical Society; American Institute of Physics for the National Institute of Standards and Technology: [Washington, D.C.]; Woodbury. N.Y. 1998

[90] M. J. Siegfried and K.-S. Choi, "Electrochemical Crystallization of Cuprous Oxide with Systematic Shape Evolution," *Adv. Mat.*, vol. 16, no. 19, pp. 1743–1746, Oct. 2004.

[91] Y.-C. Lu, D. G. Kwabi, K. P. C. Yao, J. R. Harding, J. Zhou, L. Zuin, and Y. Shao-Horn, "The discharge rate capability of rechargeable Li–O_2 batteries," *Energy Environ. Sci.*, vol. 4, no. 8, pp. 2999–3007, 2011.

[92] Y.-C. Lu, H. a. Gasteiger, M. C. Parent, V. Chiloyan, and Y. Shao-Horn, "The Influence of Catalysts on Discharge and Charge Voltages of Rechargeable Li–Oxygen Batteries," *Electrochem. Solid-State Lett.*, vol. 13, no. 6, p. A69, 2010.

[93] Y.-C. Lu, Z. Xu, H. a Gasteiger, S. Chen, K. Hamad-Schifferli, and Y. Shao-Horn, "Platinum-gold nanoparticles: a highly active bifunctional electrocatalyst for rechargeable lithium-air batteries.," *J. Am. Chem. Soc.*, vol. 132, no. 35, pp. 12170–1, Sep. 2010.

[94] A. Débart, A. J. Paterson, J. Bao, and P. G. Bruce, "α-MnO_2 Nanowires: A Catalyst for the O2 Electrode in Rechargeable Lithium Batteries," *Angew. Chemie*, vol. 120, no. 24, pp. 4597–4600, 2008.

[95] S. H. Oh, R. Black, E. Pomerantseva, J.-H. Lee, and L. F. Nazar, "Synthesis of a metallic mesoporous pyrochlore as a catalyst for lithium–O_2 batteries.," *Nature chemistry*, vol. 4, no. 12. Nature Publishing Group, pp. 1004–10, Dec-2012.

[96] T. H. Yoon and Y. J. Park, "Carbon nanotube/Co_3O_4 composite for air electrode of lithium-air battery.," *Nanoscale Res. Lett.*, vol. 7, no. 1, p. 28, Jan. 2012.

[97] W. Xu, J. Hu, M. H. Engelhard, S. A. Towne, J. S. Hardy, J. Xiao, J. Feng, M. Y. Hu, J. Zhang, F. Ding, M. E. Gross, and J.-G. Zhang, "The stability of organic solvents and carbon electrode in nonaqueous Li-O_2 batteries," *J. Power Sources*, vol. 215, pp. 240–247, Oct. 2012.

[98] J. Højberg, B. D. McCloskey, J. Hjelm, T. Vegge, K. Johansen, P. Norby, and A. C. Luntz, "An Electrochemical Impedance Spectroscopy Investigation of the Overpotentials in Li–O_2 Batteries," *ACS Appl. Mater. Interfaces*, vol. 7, pp. 4039–4047, 2015.

[99] S. Shi, Y. Qi, H. Li, and L. G. Hector, "Defect Thermodynamics and Diffusion Mechanisms in Li_2CO_3 and Implications for the Solid Electrolyte Interphase in Li-Ion Batteries," *J. Phys. Chem. C*, 2013.

[100] P. F. Fracassi, M. L. Klein, and R. G. Della Valle, “Lattice dynamics of ionic molecular crystals in the rigid ion approximation, phases II and III of sodium superoxide ’,” *Canada J. Phys.*, 1984.

[101] Y. Mo, S. P. Ong, and G. Ceder, “First-principles study of the oxygen evolution reaction of lithium peroxide in the lithium-air battery,” *Phys. Rev. B - Condens. Matter Mater. Phys.*, vol. 84, p. 205446, 2011.

[102] M. Bruno and M. Prencipe, “Ab initio quantum-mechanical modeling of the (001), and (110) surfaces of zabuyelite (Li_2CO_3),” *Surf. Sci.*, vol. 601, pp. 3012–3019, Jul. 2007.

[103] R. Younesi, G. M. Veith, P. Johansson, K. Edström, and T. Vegge, “Lithium salts for advanced lithium batteries: Li–metal, Li–O_2 , and Li–S,” *Energy Environ. Sci.*, vol. 8, no. 7, pp. 1905–1922, 2015.

[104] S. Yang and H. Knickle, “Design and analysis of aluminum / air battery system for electric vehicles,” vol. 112, pp. 162–173, 2002.

[105] S. K. Das, S. Lau, and L. a. Archer, “Sodium–oxygen batteries: a new class of metal–air batteries,” *J. Mater. Chem. A*, 2014.

[106] J. Kim, H.-D. Lim, H. Gwon, and K. Kang, “Sodium-oxygen batteries with alkyl-carbonate and ether based electrolytes.,” *Phys. Chem. Chem. Phys.*, vol. 15, no. 10, pp. 3623–9, Mar. 2013.

[107] P. Hartmann, C. L. Bender, J. Sann, A. K. Dürr, M. Jansen, J. Janek, and P. Adelhelm, “A comprehensive study on the cell chemistry of the sodium superoxide (NaO2) battery.,” *Phys. Chem. Chem. Phys.*, vol. 15, no. 28, pp. 11661–72, Jul. 2013.

[108] B. D. Mccloskey, J. M. Garcia, and A. C. Luntz, “Chemical and Electrochemical Di ff erences in Nonaqueous Li−O_2 and Na−O_2 Batteries,” pp. 2–7, 2014.

[109] S. Kang, Y. Mo, S. P. Ong, and G. Ceder, “Nanoscale stabilization of sodium oxides: implications for Na-O2 batteries.,” *Nano Lett.*, vol. 14, no. 2, pp. 1016–20, Feb. 2014.

[110] B. Lee, D.-H. Seo, H.-D. Lim, I. Park, K.-Y. Park, J. Kim, and K. Kang, “First-Principles Study of the Reaction Mechanism in Sodium–Oxygen Batteries,” *Chem. Mater.*, vol. 26, no. 2, pp. 1048–1055, Jan. 2014.

[111] S. Yang and D. J. Siegel, “Intrinsic Conductivity in Sodium-air Battery Discharge Phases: Sodium Superoxide vs. Sodium Peroxide,” *Chem. Mater.*, p. 150508165039003, 2015.

[112] A. U. Khan and S. D. Mahanti, “Collective electron effects of O_2^- in potassium superoxide,” *J. Chem. Phys.*, vol. 63, no. 6, p. 2271, 1975.

[113] R. Christensen, J. S. Hummelshøj, H. a. Hansen, and T. Vegge, “Reducing Systematic Errors in Oxide Species with Density Functional Theory Calculations,” *J. Phys. Chem. C*, vol. 119, no. 31, pp. 17596–17601, 2015.

[114] D. Sheppard, R. Terrell, and G. Henkelman, “Optimization methods for finding minimum energy paths,” *J. Chem. Phys.*, vol. 128, no. 13, pp. 1–10, 2008.

[115] J. Mizusaki, H. Tagawa, K. Saito, K. Uchida, and M. Tezuka, “Lithium carbonate as a solid electrolyte,” *Solid State Ionics*, vol. 53–56, pp. 791–797, 1992.

List of Papers

Paper I

The Influence of CO_2 Poisoning on Overpotentials and Discharge Capacity in Nonaqueous Li-Air Batteries

Yedilfana S. Mekonnen, Kristian B. Knudsen, Jon S. G. Mýrdal, Reza Younesi, Jonathan Højberg, Johan Hjelm, Poul Norby, Tejs Vegge

The Journal of Chemical Physics **140**, 121101 (2014); doi: 10.1063/1.4869212

Paper II

Role of Li_2O_2@Li_2CO_3 Interfaces on Charge Transport in Nonaqueous Li-Air Batteries

Yedilfana S. Mekonnen, Juan M. Garcia-Lastra, Jens S. Hummelshøj, Chengjun Jin, Tejs Vegge

The Journal of Physical Chemical C 2015, 119 (32), 18066-18073 DOI: 10.1021/acs.jpcc.5b04432

Paper III

Thermodynamic and Kinetic Limitation of Sodium Peroxide and Formation of Sodium Superoxide in Na-O_2 Batteries (*to be submitted*)

Yedilfana S. Mekonnen, Rune Christensen, Juan M. Garcia-Lastra, Tejs Vegge

Paper I

The Influence of CO_2 Poisoning on Overpotentials and Discharge Capacity in Nonaqueous Li-Air Batteries

Yedilfana S. Mekonnen, Kristian B. Knudsen, Jon S. G. Mýrdal, Reza Younesi, Jonathan Højberg, Johan Hjelm, Poul Norby, Tejs Vegge

The Journal of Chemical Physics **140**, 121101 (2014); doi: 10.1063/1.4869212

28 March 2014 Volume 140 Number 12

AIP | The Journal of Chemical Physics

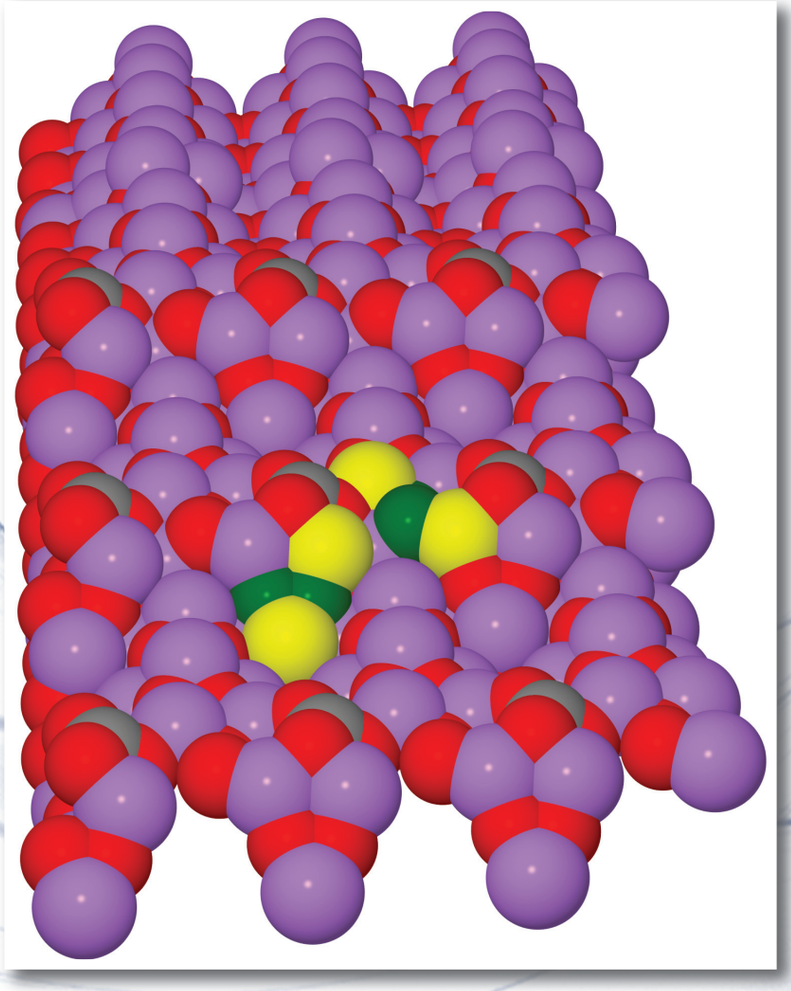

jcp.aip.org

Communication: The influence of CO2 poisoning on overvoltages and discharge capacity in non-aqueous Li-Air batteries

Yedilfana S. Mekonnen, Kristian B. Knudsen, Jon S. G. Mýrdal, Reza Younesi, Jonathan Højberg, Johan Hjelm, Poul Norby, and Tejs Vegge

Citation: The Journal of Chemical Physics **140**, 121101 (2014); doi: 10.1063/1.4869212
View online: http://dx.doi.org/10.1063/1.4869212
View Table of Contents: http://scitation.aip.org/content/aip/journal/jcp/140/12?ver=pdfcov
Published by the AIP Publishing

Communication: The influence of CO_2 poisoning on overvoltages and discharge capacity in non-aqueous Li-Air batteries

Yedilfana S. Mekonnen,[1,2] Kristian B. Knudsen,[1] Jon S. G. Mýrdal,[1] Reza Younesi,[1] Jonathan Højberg,[1] Johan Hjelm,[1] Poul Norby,[1] and Tejs Vegge[1,a)]
[1]*Department of Energy Conversion and Storage, Technical University of Denmark, Frederiksborgvej 399, DK-4000 Roskilde, Denmark*
[2]*Center for Atomic-scale Materials Design, Technical University of Denmark, DK-2800 Lyngby, Denmark*

(Received 31 January 2014; accepted 11 March 2014; published online 24 March 2014)

The effects of Li_2CO_3 like species originating from reactions between CO_2 and Li_2O_2 at the cathode of non-aqueous Li-air batteries were studied by density functional theory (DFT) and galvanostatic charge-discharge measurements. Adsorption energies of CO_2 at various nucleation sites on a stepped $(1\bar{1}00)$ Li_2O_2 surface were determined and even a low concentration of CO_2 effectively blocks the step nucleation site and alters the Li_2O_2 shape due to Li_2CO_3 formation. Nudged elastic band calculations show that once CO_2 is adsorbed on a step valley site, it is effectively unable to diffuse and impacts the Li_2O_2 growth mechanism, capacity, and overvoltages. The charging processes are strongly influenced by CO_2 contamination, and exhibit increased overvoltages and increased capacity, as a result of poisoning of nucleation sites: this effect is predicted from DFT calculations and observed experimentally already at 1% CO_2. Large capacity losses and overvoltages are seen at higher CO_2 concentrations. © *2014 AIP Publishing LLC*. [http://dx.doi.org/10.1063/1.4869212]

I. INTRODUCTION

As energy storage needs are growing rapidly, there is also an increase in research into high energy density materials for energy storage. Significant attention has been given to metal-air batteries, particularly Li-air batteries, as future environmentally friendly high energy density storage for vehicles, where the capacity offered by existing Li-ion technology is too low to solve the increasing demands on batteries.[1] The Li-O_2 couple is particularly attractive and could have ∼5–10 times greater specific energies than currently available Li-ion batteries, though there are severe scientific and technical challenges that need to be addressed.[2,3] Such as a clear understanding of the Li_2O_2 growth mechanisms, transport processes, interfacial phenomena, air impurities, and stability of the key components are vital parts of non-aqueous rechargeable Li-air cell research.[4]

As first reported by Abraham and Jiang in 1996, the Li-O_2 battery with aprotic solvent is shown to be rechargeable, when Li_2O_2 is formed during discharge at the cathode.[5] Detailed understanding of the Li_2O_2 growth mechanism is important to solve the problem associated with the practical limitations of the battery. Previous theoretical works by Hummelshøj *et al.*[6] and Radin *et al.*[7,8] showed that steps on a reconstructed $(1\bar{1}00)$surface could act as nucleation sites for low discharge overvoltage and facets such as (0001), $(1\bar{1}00)$, and $(11\bar{2}0)$ have similar surface energies. Hummelshøj *et al.*[9] have also shown that surfaces are potential dependent and vary during discharge and charge. According to G_0W_0 calculations, both Li_2O_2 and Li_2CO_3 are insulating materials with wide band gap of 4.9 and 8.8 eV, respectively.[10–12] Therefore, as these materials deposit at the cathode surface during discharge they will limit the electronic conduction and lead to sudden death during discharge within 5–10 nm thick Li_2O_2 deposits.[13,14] However, recent DFT calculations found that hole and electron polaronic transports at the surface and in bulk Li_2O_2 and Li_2CO_3 can take place. Using a PBE+U (Hubbard-corrected Perdew–Burke–Ernzerhof) exchange correlation functional, Garcia-Lastra *et al.*[11] revealed that the hole polarons have higher mobility than electron polarons and Li_2CO_3 exhibits lower conduction than Li_2O_2. Recent works by Luntz *et al.* have shown that hole tunneling should dominate and polaronic transport is only expected to be significant in Li_2O_2 at elevated temperatures and low current densities.[15,16]

Li_2CO_3 like crystalline species are formed by parasitic side reactions between the Li_2O_2 or LiO_2 and carbon sources from air impurities such as CO and CO_2 gases,[17] the graphite itself, or the decomposition of aprotic electrolytes. Younesi *et al.*[18,34] reported the degradation of various electrolytes by Li_2O_2 and documented Li_2CO_3 as a decomposition product from aprotic electrolytes. Likewise, McCloskey *et al.*[3] have shown that carbonates accumulate at the C-Li_2O_2 and Li_2O_2-electrolyte interfaces and are responsible for a large potential increase during recharge and a huge decrease in exchange current density. This makes growth of Li_2O_2 on Li_2CO_3 an equally important process to investigate, but this is beyond the scope of this communication. As reported by Siegfried *et al.*[19] and Myrdal and Vegge[20] adsorption of sulfur containing compounds on oxide surfaces could also control the electrochemical growth mechanism. Adsorbed species at surfaces can potentially block the nucleation sites, and therefore, alter the growth directions, overvoltages, and capacities.

In this communication, we address the influence of CO_2 contamination on the Li_2O_2 growth mechanism, discharge/charge overvoltages, and capacity in non-aqueous

a)E-mail: teve@dtu.dk

TABLE I. Adsorption energies of CO_2 in the gas phase at $(1\bar{1}00)$ Li_2O_2 surface.

Species	Sites	Adsorption energy (eV)
CO_2	Step valley	−0.73
	Terrace valley	−0.21
	Step ridge	−0.02

Li-air batteries using density functional theory (DFT) and galvanostatic measurements. Among other air contaminants, CO_2 is the most critical subject due to its high solubility in aprotic electrolytes and high reactivity with Li_2O_2 to form an insulating material Li_2CO_3.

II. COMPUTATIONAL RESULTS AND ANALYSIS

DFT[21–23] as implemented in the GPAW (grid-based projector-augmented wave method) code[24] is used to perform the presented calculations through the atomic simulation environment (ASE).[25] GPAW is built on real space grids and non-valence electrons are described by PAW (projector augmented-wave method).[26,27] Electron exchange and correlation is approximated by the revised Perdew–Burke–Ernzerhof (RPBE) functional.[28] The stepped $(1\bar{1}00)$ Li_2O_2 surface with a super cell consisting of a 56–64 atoms slab with a 18 Å vacuum layer between periodic images along the z-axis, see Fig. S1 in the supplementary material.[35] Since the oxygen rich (0001) facet will also be exposed, in particular under charging conditions,[9] and subsequent investigations should be performed to analyze the detailed mechanisms of CO_2 bonding to this facet. Recent computational DFT results for SO_2 adsorption on stepped (0001) and $(1\bar{1}00)$ surfaces do, however, show preferential bonding to the $(1\bar{1}00)$ facets,[20] which is investigated here. The k-points are sampled with a (4,4,1) Monkhorst-Pack mesh and 0.15 grid points is used. Atomic energy optimization calculations are performed until all forces are less than 0.01 eV/Å. Energy barriers are calculated by the climbing image nudged elastic band (CINEB) method.[29–31]

Adsorption energies of CO_2 at various nucleation sites on a stepped $(1\bar{1}00)$ Li_2O_2 surface were determined, see Table I. CO_2 binds preferentially at the step valley site and weakly binds at the step ridge site. NEB calculations show that once CO_2 is adsorbed at step valley site, it is bound by barriers upwards of 3 eV, see Fig. S2 in the supplementary material,[35] since the CO_2 molecule is required to desorb from the surface prior to re-adsorbing at the step site. The detailed nature of a conversion of adsorbed CO_2 to Li_2CO_3 warrants further investigations, but we find the adsorption of a single CO_2 molecule forms a $Li_{\sim 3}CO_3$-type complex (Fig. 1(b)), which could act as a nucleation site for further growth of Li_2CO_3.

The computational lithium electrode approach is used in the free energy calculations.[6,32] Defined as, U = 0, when bulk Li anode and Li ions in solution ($Li^+ + e^-$) are at equilibrium. The free energy change of the reaction is shifted by $-neU$ at an applied bias, where n is the number of transferred electrons; other assumptions are listed in the supplementary material.[35] As reported by Hummelshøj *et al.*, kinks and steps sites of the stepped $(1\bar{1}00)$ Li_2O_2 surface are favorable nucleation sites for a low overvoltage Li_2O_2 growth mechanism. The influence of CO_2 poisoning on the Li_2O_2 growth mechanism is studied while CO_2 is already adsorbed at step valley site (Fig. 1(b)).

The free energy diagram in Fig. 2 shows a four steps, two formula units Li_2O_2 growth mechanism on the stepped $(1\bar{1}00)$ Li_2O_2 surface with and without CO_2. The first step in the presence of CO_2 is adsorption of LiO_2 species (Fig. 1(c)), and which reduces the binding energy by 0.44 V compared to the pure discharge. The next step is the addition of a second LiO_2 species (Fig. 1(d)), which is the potential limiting charge step that raises the binding energy by 0.20 V compared to pure Li_2O_2. This is followed by subsequent additions of two Li (Figs. 1(e) and 1(f)) with relatively small binding energies with respect to a pure discharge. In the pure O_2 discharge mechanism, unlike in the presence of CO_2, addition of the first Li is the limiting charge potential step. The $2Li_2O_2$ growth at the step surface effectively displaces CO_2 from the step to the less stable terrace site.

Hummelshøj *et al.* have reported that the pure Li_2O_2 growth mechanism follows a 4 steps reaction mechanism, where all reaction steps are electrochemical, similar to what is seen in the presence of CO_2. The equilibrium potential can be obtained as $U_0 = -\Delta G/2e$. The effective equilibrium potential on a pure surface becomes 2.73 V (experimental value, $U_{0,Exp} = 2.85$ V), while in the presence of CO_2, this is effectively reduced to 2.53 V for the first cycle due to the shift in binding energy of CO_2 from a step valley to terrace site. As a result, discharge at other facets may become activate.[9] At neutral bias all reaction steps are downhill, but at an applied potential, the free energy difference changes for each step calculated as

$$\Delta G_{i,U} = \Delta G_i - eU. \quad (1)$$

The lowest free energy step, $\Delta G_{i,min}$, along the reaction path becomes uphill first at an applied potential called limited discharge potential, $U_{discharge}$, while the largest free energy step, $\Delta G_{i,max}$, that is last to become downhill for the reversed reaction at an applied potential called limited charge potential, U_{charge}, obtained as

$$U_{discharge} = \min[-\Delta G_i/e] \text{ and } U_{charge} = \max[-\Delta G_i/e]. \quad (2)$$

In the presence (absence) of a single CO_2 molecule, this discharge occurs as described in Fig. 1, resulting in $U_{discharge}$ = 2.21 V (2.66 V), and U_{charge} = 2.97 V (2.81 V) and the discharge and charge overvoltages in the presence (absence) of CO_2 are $\eta_{discharge} = 0.31$ V (0.07 V), and $\eta_{charge} = 0.44$ V (0.08 V). The calculated 0.44 V overvoltage for charge corresponds to low CO_2 concentrations, where only a single CO_2 molecule is adsorbed on the Li_2O_2 step forming a $Li_{\sim 3}CO_3$ type complex (see Fig. 1). Here, the charging process follows the same reaction steps as the discharge, but in reverse (from right to left in Fig. 2), i.e., the first two steps are desorption of two Li and followed by desorption of 2 LiO_2 species: in total desorbing 2 Li_2O_2 units from the surface and returning to the configuration in Fig. 1(b). Quantitative agreement with

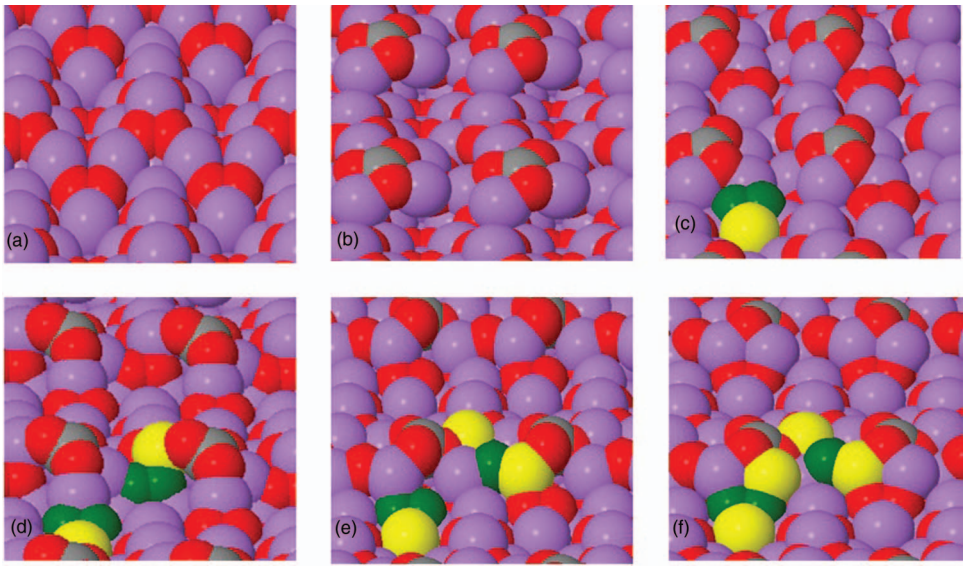

FIG. 1. Stepped Li_2O_2 ($1\bar{1}00$) surface before and after adsorption of CO_2 and 4 steps Li_2O_2 growth pathways during discharge. (a) Pure stepped Li_2O_2 surface. (b) CO_2 adsorbs to step valley site forming a $Li_{\sim 3}CO_3$ type complex. (c) 1st LiO_2 adsorbs. (d) 2nd LiO_2 adsorbs. (e) 1st Li. (f) 2nd Li adsorbs to the surface completing growth of 2 Li_2O_2 formula units. Atoms labeled as: C (gray), Li (purple), and O (red). Deposited atoms shown as: Li (yellow) and O (green).

experimental overvoltages can therefore only be expected for low concentrations of CO_2 (e.g., 1%). For higher CO_2 concentrations, the formation of crystalline Li_2CO_3 would be expected, resulting in significantly larger overvoltages.[3]

III. EXPERIMENTAL RESULTS AND ANALYSIS

Li-air batteries were constructed using a Swagelok design and assembled inside an Ar-filled glovebox ($\leq$3 ppm O_2 and H_2O). Each battery contained a 200 μl 1 M LiTFSI (99.95%, Sigma-Aldrich) and 1,2-dimethoxymethane, DME, (H_2O < 20 ppm, BASF) electrolyte. Cathodes consisted of P50 AvCarb carbon paper (Fuel cell store), which were sonicated using 2-propanol (99.5%, Sigma-Aldrich) and acetone ($\geq$99.8%, Sigma-Aldrich), introduced into a glovebox where they were rinsed with DME before drying in vacuum at 80 °C for 12 h. Cathodes were supported by a 316 steel mesh. A

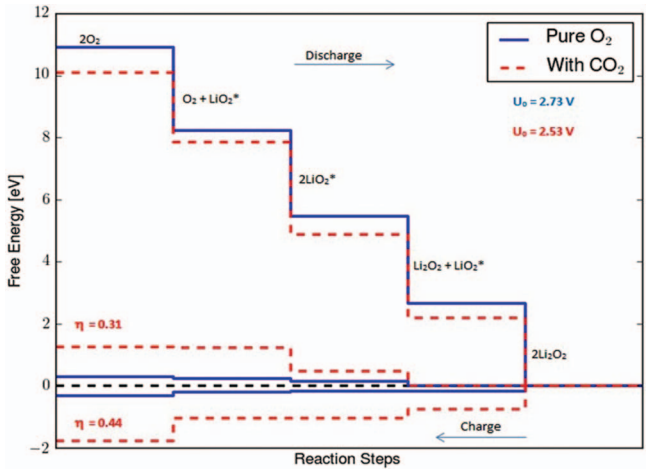

FIG. 2. Calculated free energy diagrams for a four steps discharge mechanism on a stepped ($1\bar{1}00$)Li_2O_2 surface with and without adsorbed CO_2.

10 mm diameter lithium foil (99.9%, Sigma-Aldrich) was used as anode. Two Celgard separators 2500 (Celgard) were placed in between the two electrodes. The separators were sonicated in EtOH (99.9%, Sigma-Aldrich), transferred to a glovebox, and rinsed with DME before drying in vacuum at 80 °C for 12 h. Experiments were performed using a Bio-Logic VMP3 Multichannel galvanostat (Bio-Logic, Claix, France). Batteries were operated in two galvanostatic modes: First, at 100 μA (127.3 μA/cm^2) where cells were discharged to 2 V and charged to 4.6 V vs. Li^+/Li. Second, at 50 μA (63.6 μA/cm^2) using the same potential limits.

To investigate the effect of gaseous CO_2, the assembled cells were purged with three different atmospheres: 0/100 CO_2/O_2, 1/99 CO_2/O_2, and 50/50 CO_2/O_2. Three individual batteries were assembled and investigated for each atmosphere and each curve presented in Figs. 3 and 4 is therefore an average of three cells with the equal atmosphere as shown in Fig. S3 in the supplementary material.[35] The lowest discharge capacity was observed for the 50% CO_2 cells and is likely caused by the high concentration of electrochemically inactive CO_2. A similar effect was observed, by Gowda *et al.*[17] for a pure CO_2 cell, where the cell potential immediately dropped. It should however be noted that Takechi *et al.*[33] observed, quite to the contrary of our observations, higher discharge capacities up to 70% CO_2 with respect to pure O_2 cells. Interestingly, a higher discharge capacity was observed for the 1% CO_2 cells in respect to the pure O_2 cells as shown in Fig. 3 (inset). A possible explanation is the dissolution of Li_2CO_3 species in DME and/or, as also suggested by Gowda *et al.*, or a change in deposition morphology compared to that deposited in the pure O_2 cells as suggested by Myrdal and Vegge.[20] Such morphological changes could increase the total electrodeposited layer and lead to higher capacities.

All CO_2 cells have higher discharge overvoltages compared to cells with pure O_2 at a discharge rate of 127.3 μA/cm^2, which may be caused by the blocking of the

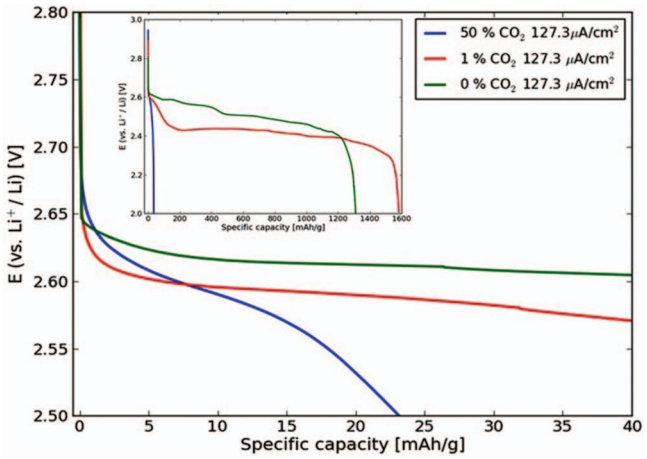

FIG. 3. Galvanostatic discharge profiles at 127.3 μA/cm^2 discharge at three different atmospheres: 50% CO_2, 1% CO_2, and 0% CO_2. Inset shows the increase in discharge capacity in 1% CO_2.

active nucleation sites by solubilized CO_2, forcing the reactions to follow pathways with higher overvoltages. This effect can even be seen at 1% CO_2, as illustrated in Fig. 3 above. The charge capacity, as seen in Fig. 4 and Fig. S4 in the supplementary material,[35] is very dependent on the CO_2 concentration, with high concentrations limiting charge capacity and thereby the cell reversibly. The 50% CO_2 cells reach the lower potential limit (2.0 V) early, at approximately 35 mAh/g, while 1% CO_2 cells and pure O_2 cells continued until capacities in the range 1150–1600 mAh/g were reached depending on current density. The low charge capacity at high CO_2 contaminations should be attributed to the poor Li-CO_2 electrochemistry, also reported by Gowda *et al.* The charging overvoltages are a function of both current density and the level of CO_2 contamination. While there is no significant difference in overvoltages between cells charge at 127.3 and 63.6 μA/cm^2 for 50% CO_2 cells, which again can be attributed to the poor Li-CO_2 electrochemistry. At 127.3 μA/cm^2, there is an increase in overvoltage of about 0.4 and 0.3 V for 1% CO_2 cells and 0% CO_2 cells, respectively. The general increase in overvoltages with increasing current density can be explained

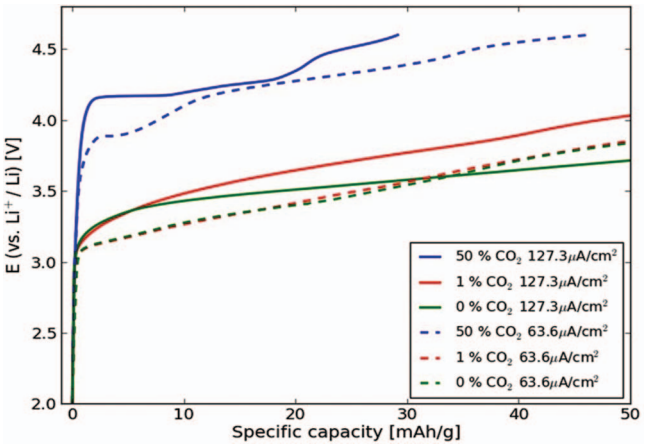

FIG. 4. Galvanostatic charge profiles at 127.3 (solid) and 63.6 (dotted) μA/cm^2 at three different atmospheres: 50% CO_2, 1% CO_2, and 0% CO_2.

by the Butler-Volmer model, while the larger overvoltage for the 1% CO_2 cells than 0% CO_2 cells is expectedly caused by the formation and oxidation of the carbonate like species (Fig. 1(b)). A second charge at 63.6 μA/cm^2 shows identical results for 1% and 0% CO_2. This can be ascribed to the evolution of CO_2 observed during the initial charge cycle, where CO_2 is released at 4.5 V, as shown in Fig. S5 in the supplementary material,[35] resulting in residual CO_2 in the electrolyte causing blocking of the step sites in subsequent charging experiments.

IV. CONCLUSIONS

Influences of CO_2 poisoning at a stepped (1$\bar{1}$00) Li_2O_2 surface in non-aqueous Li-air battery were studied using DFT calculations and cells were characterized by electrochemical charge-discharge measurements. CO_2 preferentially binds at step valley site at the Li_2O_2 surface and the Li_2O_2 growth mechanism consists of four electrochemical steps, following the same sequence for both pure and contaminated systems. Accordingly, the first step of the growth mechanism is the adsorption of two LiO_2 species and followed by addition of two Li to form 2 Li_2O_2 at the cathode surface. For charge in the low CO_2 limit, a similar reaction will occur, but in reverse order.

Low concentrations of CO_2 (1%) effectively block the surface-active nucleation sites and alter the shape and growth directions of Li_2O_2 on the surface; resulting in an increased capacity of the battery at the expense of an increase in the overvoltage in the presence of CO_2. A similar behavior is seen in pure oxygen following charging to 4.5 V, resulting from decomposition reactions. The effective discharge potential is reduced by 0.20 V on a stepped (1$\bar{1}$00) Li_2O_2 surface, shifting the reaction to alternate nucleation sites. In general, the DFT calculations and experimental results show that the recharging process is strongly influenced by CO_2 contamination, and exhibits significantly increased charging overvoltage, which is observed already with 1% CO_2 contamination, while at 50% CO_2 a large capacity loss is also seen.

ACKNOWLEDGMENTS

The authors acknowledge support of this work from the ReLiable project (Project No. 11-116792) funded by the Danish Council for Strategic Research Programme Commission on Sustainable Energy and Environment.

[1]D. Linden and T. Reddy, *Hand Book of Batteries*, 3rd ed. (McGraw Hill, New York, 2001).
[2]T. Ogasawara, A. Débart, M. Holzapfel, P. Novák, and P. G. Bruce, J. Am. Chem. Soc. **128**, 1390 (2006).
[3]B. D. McCloskey, A. Speidel, R. Scheffler, D. C. Miller, V. Viswanathan, J. S. Hummelshøj, J. K. Nørskov, and A. C. Luntz, J. Phys. Chem. Lett. **3**, 997 (2012).
[4]G. Girishkumar, B. D. McCloskey, A. C. Luntz, S. Swanson, and W. Wilcke, J. Phys. Chem. Lett. **1**, 2193 (2010).
[5]K. M. Abraham and Z. Jiang, J. Electrochem. Soc. **143**, 1 (1996).
[6]J. S. Hummelshøj, J. Blomqvist, S. Datta, T. Vegge, J. Rossmeisl, K. S. Thygesen, A. C. Luntz, K. W. Jacobsen, and J. K. Nørskov, J. Chem. Phys. **132**, 071101 (2010).
[7]M. D. Radin, J. F. Rodriguez, F. Tian, and D. J. Siegel, J. Am. Chem. Soc. **134**, 1093 (2011).

[8]M. D. Radin, F. Tian, and D. J. Siegel, J. Mat. Sci. **47**, 7564 (2012).
[9]J. S. Hummelshøj, A. C. Luntz, and J. K. Nørskov, J. Chem. Phys. **138**, 034703 (2013).
[10]P. Albertus, G. Girishkumar, B. D. McCloskey, R. S. Sanchez-Carrera, B. Kozinsky, J. Christensen, and A. C. Luntz, J. Electrochem. Soc. **158**(3), A343 (2011).
[11]J. M. Garcia-Lastra, J. S. G. Myrdal, K. S. Thygesen, and T. Vegge, J. Phys. Chem. C **117**, 5568 (2013).
[12]J. M. Garcia-Lastra, J. D. Bass, and K. S. Thygesen, J. Chem. Phys. **135**, 121101 (2011).
[13]V. Viswanathan, K. S. Thygesen, J. S. Hummelshøj, J. K. Nørskov, G. Girishkumar, B. D. McCloskey, and A. C. Luntz, J. Chem. Phys. **135**, 214704 (2011).
[14]J. Chen, J. S. Hummelshøj, K. S. Thygesen, J. S. G. Myrdal, J. K. Nørskov, and T. Vegge, Catal. Today **165**, 2 (2011).
[15]J. B. Varley, V. Viswanathan, J. K. Nørskov, and A. C. Luntz, Energy Environ. Sci. **7**, 720 (2014).
[16]A. C. Luntz, V. Viswanathan, J. Voss, J. B. Varley, J. K. Nørskov, R. Scheffler, and A. Speidel, J. Phys. Chem. Lett. **4**, 3494 (2013).
[17]S. R. Gowda, A. Brunet, G. M. Wallraff, and B. D. McCloskey, J. Phys. Chem. Lett. **4**, 276 (2013).
[18]R. Younesi, M. Hahlin, F. Björefors, P. Johansson, and K. Edström, Chem. Mater. **25**, 77 (2013).
[19]M. J. Siegfried and K. S. Choi, Adv. Mat. **16**, 1743 (2004).
[20]J. S. G. Myrdal and T. Vegge, "DFT study of selective poisoning of Li-Air batteries for increased discharge capacity," RSC Adv. (to be published).
[21]P. Hohenberg and W. Kohn, Phys. Rev. **136**, B864 (1964).
[22]W. Kohn and L. Sham, Phys. Rev. **140**, A1133 (1965).
[23]J. J. Mortensen, L. B. Hansen, and K. W. Jacobsen, Phys. Rev. B **71**, 035109 (2005).
[24]J. Enkovaara, C. Rostgaard, J. J. Mortensen, J. Chen, M. Dulak, L. Ferrighi, J. Gavnholt, C. Glinsvad, V. Haikola, H. A. Hansen, H. H. Kristoffersen, M. Kuisma, A. H. Larsen, L. Lehtovaara, M. Ljungberg, O. Lopez-Acevedo, P. G. Moses, J. Ojanen, T. Olsen, V. Petzold, N. A. Romero, J. Stausholm-Moller, M. Strange, G. A. Tritsaris, M. Vanin, M. Walter, B. Hammer, H. Hakkinen, G. K. H. Madsen, R. M. Nieminen, J. K. Nørskov, M. Puska, T. T. Rantala, J. Schiøtz, K. S. Thygesen, and K. W. Jacobsen, J. Phys. Condens. Matter **22**, 253202 (2010).
[25]S. R. Bahn and K. W. Jacobsen, Comput. Sci. Eng. **4**, 56 (2002).
[26]P. E. Blöchl, Phys. Rev. **50**, 17953 (1994).
[27]P. E. Blöchl, C. J. Först, and J. Schimpl, Bull. Mater. Sci. **26**, 33 (2003).
[28]B. Hammer, L. B. Hansen, and J. K. Nørskov, Phys. Rev. B **59**, 7413 (1999).
[29]H. Jonsson, G. Mills, and K. W. Jacobsen, *Classical and Quantum Dynamics in Condensed Phase Systems*, edited by B. J. Berne, G. Cicotti, and D. F. Coker (World Scientific, 1998).
[30]G. Henkelman and H. Jónsson, J. Chem. Phys. **113**, 9978 (2000).
[31]G. Henkelman, B. Uberuaga, and H. A. Jónsson, J. Chem. Phys. **113**, 9901 (2000).
[32]J. K. Nørskov, J. Rossmeisl, A. Logadottir, L. Lindqvist, J. R. Kitchin, T. Bligaard, and H. Jonsson, J. Phys. Chem. B **108**, 17886 (2004).
[33]K. Takechi, T. Shiga, and T. Asaoka, Chem. Commun. **47**, 3463 (2011).
[34]R. Younesi, P. Norby, and T. Vegge, ECS Electrochem. Lett. **3**, A15 (2014).
[35]See supplementary material at http://dx.doi.org/10.1063/1.4869212 for Figs. S1–S5.

Supporting Information

The Influence of CO_2 Poisoning on Overvoltages and Discharge Capacity in Non-aqueous Li-Air Batteries

Yedilfana S. Mekonnen[1,2], Kristian B. Knudsen[1], Jon S. G. Mýrdal[1,2], Reza Younesi[1], Jonathan Højberg[1], Johan Hjelm[1], Poul Norby[1], Tejs Vegge[1,2,a]

[1]*Department of Energy Conversion and Storage, Technical University of Denmark, Frederiksborgvej 399, DK-4000 Roskilde, Denmark.*

[2]*Center for Atomic-scale Materials Design and Department of Physics, Technical University of Denmark, DK-2800 Lyngby, Denmark*

[a]Corresponding Author E-mail: teve@dtu.dk

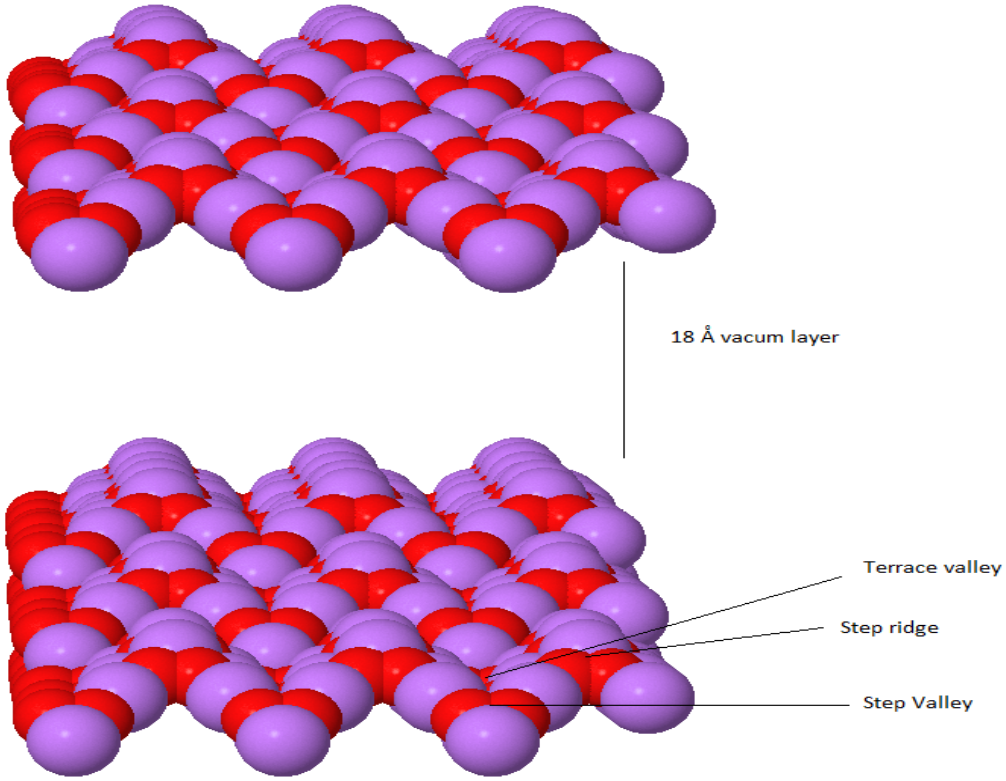

FIG S1: The stepped $(1\bar{1}00)$ Li_2O_2 surface with 3x3x2 super cell consisting of a 56-64 atoms slab with a 18 Å vacuum layer between periodic images along the z-axis.

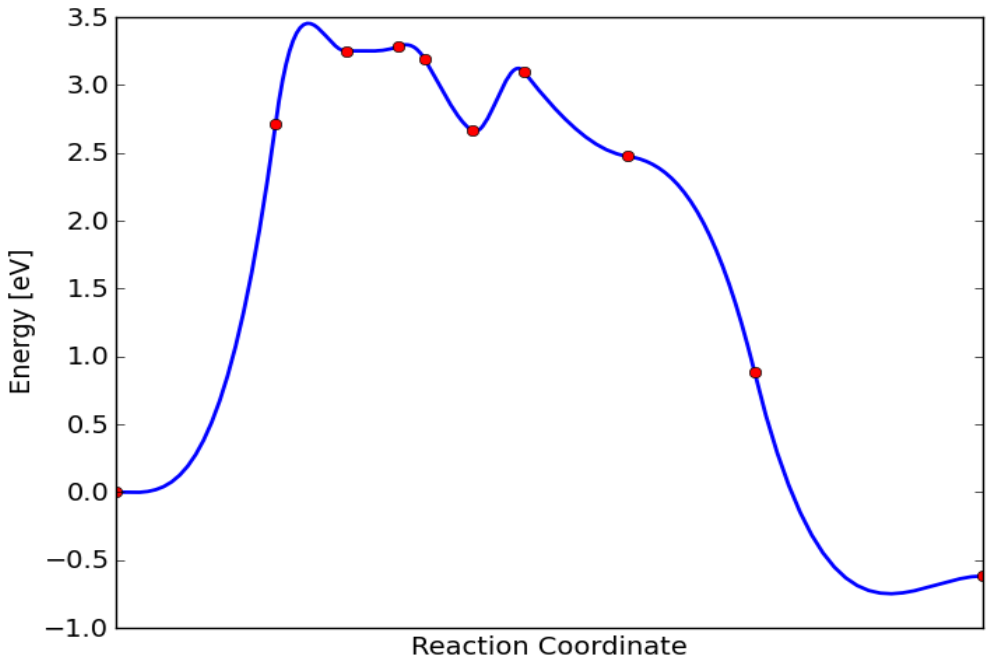

FIG S2. Climbing image Nudged elastic band calculations for CO_2 migration from less favorable terrace site to more favorable step valley site on stepped $(1\bar{1}00)$ Li_2O_2 surface with energy barrier above 3 eV.

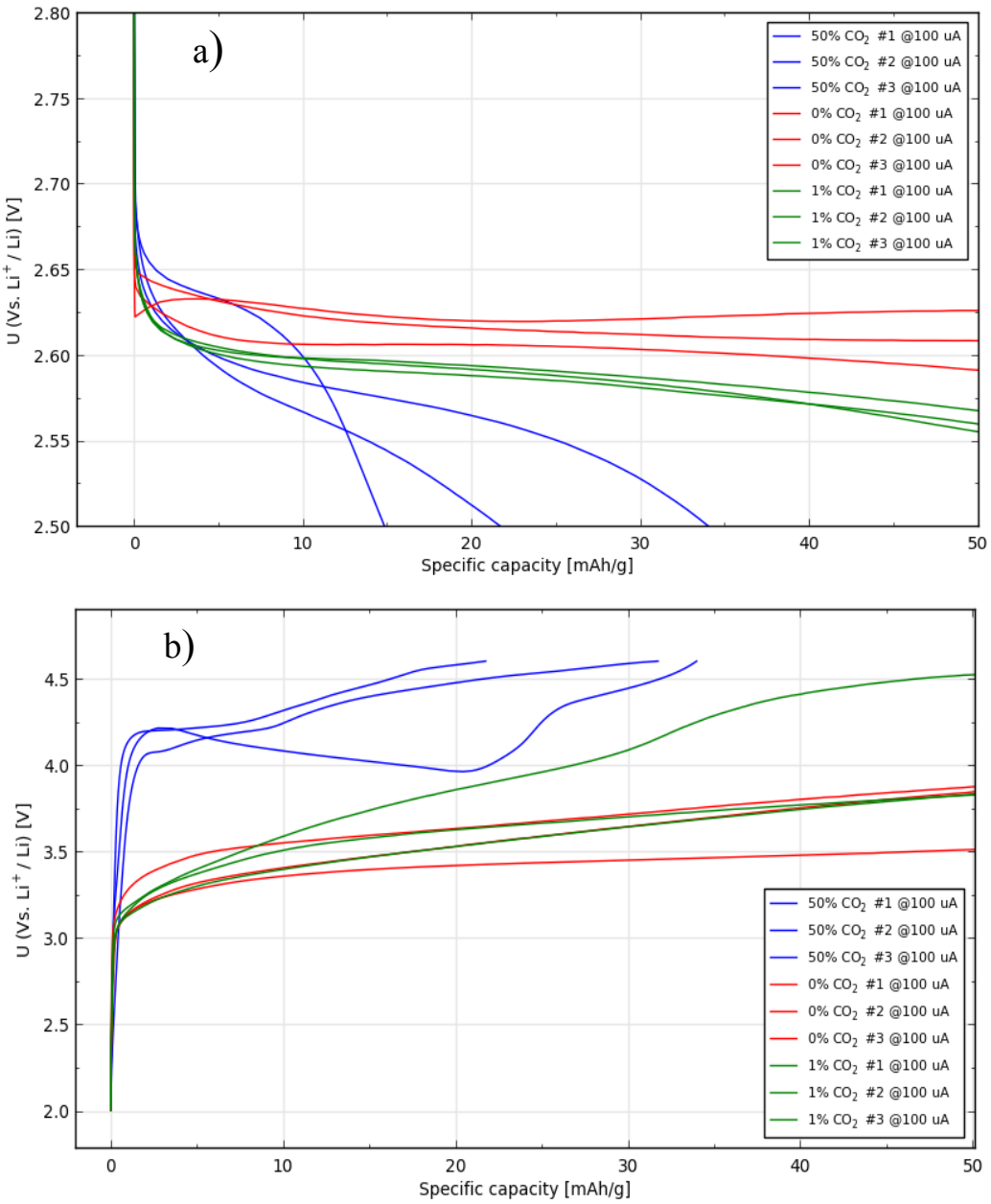

FIG S3: The average discharge and charge curves of each of the three atmospheric conditions (0, 1 and 50 % CO_2) are taken from the three cells measurements at *127.3 µA/cm*^{2}.

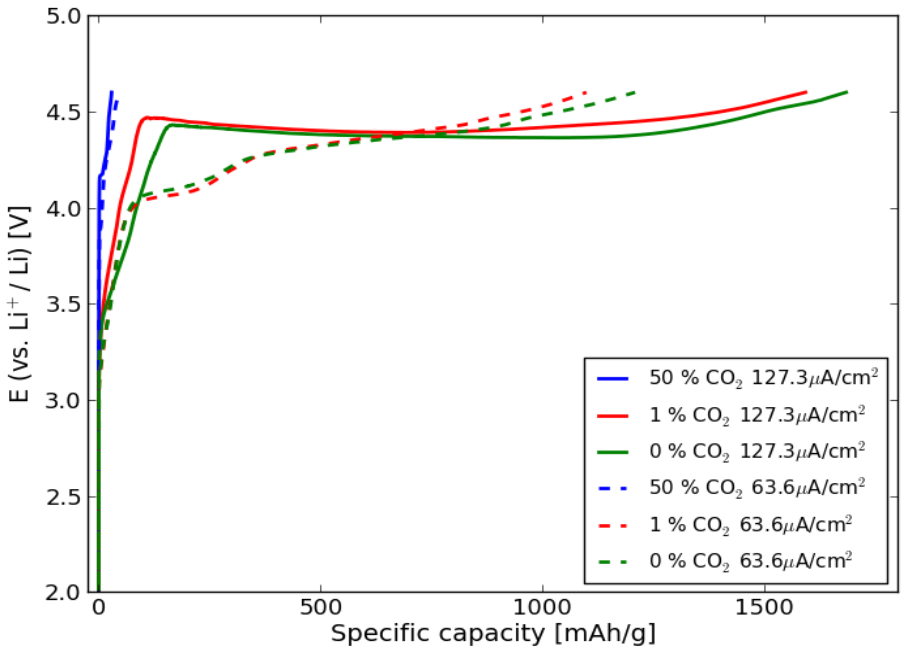

FIG S4: A Complete Galvanostatic charge profiles at 127.3 µA/cm^2 (solid) and 63.6 (dotted) µA/cm^2 (dotted) at three different atmospheres: 50 % CO_2, 1 % CO_2 and 0 % CO_2.

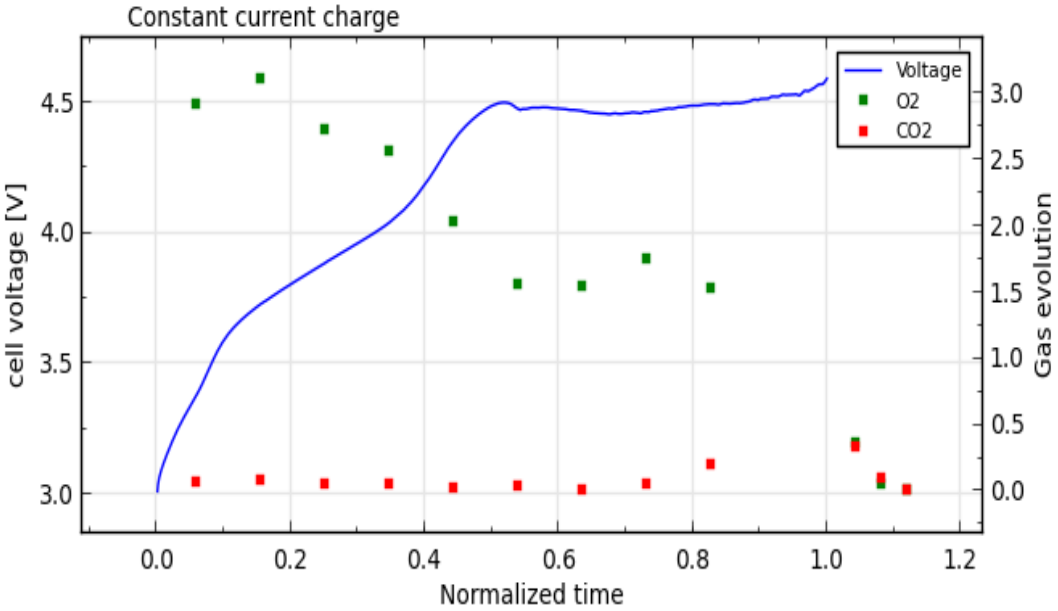

FIG S5. Evolution of O_2 and CO_2 as a function of time during a constant current charge following a constant current discharge to 2 V. The current of both charge and discharge was 100 µA/cm^2. The tested cell is Li|DME+1M LiTFSI|P50 carbon paper. The measurement is performed with a differential electrochemical mass spectrometer.

Paper II

Role of Li_2O_2@Li_2CO_3 Interfaces on Charge Transport in Nonaqueous Li-Air Batteries

Yedilfana S. Mekonnen, Juan M. Garcia-Lastra, Jens S. Hummelshøj, Chengjun Jin, Tejs Vegge

The Journal of Physical Chemical C 2015, 119 (32), 18066-18073 DOI: 10.1021/acs.jpcc.5b04432

THE JOURNAL OF PHYSICAL CHEMISTRY C

Article

pubs.acs.org/JPCC

Role of Li_2O_2@Li_2CO_3 Interfaces on Charge Transport in Nonaqueous Li−Air Batteries

Yedilfana S. Mekonnen,[†] Juan M. Garcia-Lastra,[†] Jens S. Hummelshøj,[§] Chengjun Jin,[‡] and Tejs Vegge*[,†]

[†]Department of Energy Conversion and Storage, Technical University of Denmark, Fysikvej, Building 309, 2800 Kgs Lyngby, Denmark

[‡]Center for Atomic-Scale Materials Design and Department of Physics, Technical University of Denmark, Fysikvej, Building 307, 2800 Kgs Lyngby, Denmark

[§]SUNCAT Center for Interface Science and Catalysis, SLAC National Accelerator Laboratory, Menlo Park, California 94025, United States

ABSTRACT: The formation and oxidation of the main discharge product in nonaqueous secondary Li−O_2 batteries, that is, Li_2O_2, has been studied intensively, but less attention has been given to the formation of cathode−electrolyte interfaces, which can significantly influence the performance of the Li−O_2 battery. Here we apply density functional theory with the Hubbard U correction (DFT+U) and nonequilibrium Green's function (NEGF) methods to investigate the role of Li_2O_2@Li_2CO_3 interface layers on the ionic and electronic transport properties at the oxygen electrode. We show that, for example, lithium vacancies accumulate at the peroxide part of the interface during charge, reducing the coherent electron transport by two to three orders of magnitude compared with pristine Li_2O_2. During discharge, Li_2O_2@Li_2CO_3 interfaces may, however, provide an alternative in-plane channel for fast electron polaron hopping that could improve the electronic conductivity and ultimately increase the practical capacity in nonaqueous Li−O_2 batteries.

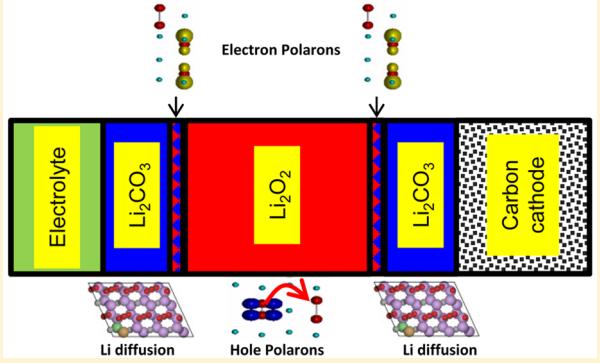

1. INTRODUCTION

Today, most electric vehicles and hybrid electric vehicles rely on Li-ion batteries. The main drawbacks of Li-ion batteries are their high price, slow charging, and low energy/power density compared with that of gasoline.[1] The latest specific energy of Li-ion batteries is ∼300 mAh/g,[2] which is an order of magnitude lower than that of the Li−air battery, ∼3842 mAh/g.[3] Recently, metal−air batteries have gained significant attention as a future alternative to Li-ion batteries in the transportation sector. In particular, the Li−O_2 couple appears to be a promising choice due to its superior energy storing capacity.

Li−air batteries, however, suffer from several drawbacks that must be resolved before they can enter the market. Various complex chemical and electrochemical side-reactions occur at the interfaces in practical nonaqueous Li−air batteries, which limits the rechargeability and cyclability.[4] Several kinds of parasitic compounds and interfaces are likely formed between/within the reaction products and cell components in the nonaqueous Li−air batteries. The types of interfaces depend on the type of electrodes and electrolytes used in the cell and the reaction conditions. Li_2CO_3 is readily formed at the cathode together with Li_2O_2 when carbonate-based electrolytes, for example, ethylene carbonates (ECs), are used,[5,6] but if noncarbonate-based electrolytes such as dimethoxyethane (DME) are used, Li_2O_2 is the main discharge product. In the latter case, layers of Li_2CO_3 can also form due to side reactions with the carbon cathode, DME, or CO_2 impurities from the air.[7,8] The discharge capacity in Li−O_2 batteries is primarily limited by the poor electronic conduction in Li_2O_2[9] and because electronic conductivity in Li_2CO_3 is even smaller than that of Li_2O_2, it is critical to determine the effect of such layers. Experiments performed in carbon- or ether-based electrolytes reported that the evolution of CO_2 gas when the battery recharges at slightly above 3 and 4 V mainly comes from the electrolyte decomposition and carbonate deposit at the cathode surface, respectively.[4,6,8,10] It has also been reported in Li-ion battery studies that Li_2CO_3 is one of the most chemically[11] and mechanically[12] stable species formed at both cathode and anode electrodes. Thus, it is inevitably the formation of Li_2O_2@Li_2CO_3 interfaces in the cathode of nonaqueous Li−air batteries, for instance, at Li_2O_2@C(graphite) and Li_2O_2@electrolyte interfaces.[4] To summarize, Li_2O_2@Li_2CO_3 interfaces could be formed in different scenarios, namely, (a) liquid electrolyte |Li_2CO_3|Li_2O_2| carbon cathode, which appears when a carbon-based electrolyte is used or due to the presence of atmospheric CO_2; (b) liquid electrolyte |Li_2O_2|Li_2CO_3| carbon cathode, which has been shown to be formed due to the

Received: May 8, 2015
Revised: June 24, 2015
Published: July 20, 2015

DOI: 10.1021/acs.jpcc.5b04432
J. Phys. Chem. C 2015, 119, 18066−18073

reactions between the Li ions and C cathode in the presence of oxygen; and (c) liquid electrolyte $|Li_2CO_3|Li_2O_2|Li_2CO_3|$ carbon cathode, which is the combination of the above scenarios a and b. We should stress that in the present work we only model the $Li_2O_2@Li_2CO_3$ interface, disregarding where the interface appears. Thus, our model is valid in the three scenarios previously mentioned.

Here we investigate the implications of $Li_2O_2@Li_2CO_3$ interfaces for charge transport, that is, mainly the lithium diffusion and electronic transport properties in nonaqueous Li–O_2 batteries.[13] Regarding, the electronic transport we study both polaronic and tunneling conduction regimes. We also show that the Li vacancies have a thermodynamic driving force for accumulation at the Li_2O_2 part of the $Li_2O_2@Li_2CO_3$ interface compared with pristine Li_2O_2. Consequently, we have studied in detail the impact of these Li vacancies on the coherent transport properties at the interface.

The paper is structured in four major sections. The description of the crystal structures, computational methods, and electronic properties of the materials is covered in Section 2. In Section 3, the main results are discussed in three subsections. The first subsection (3.1) covers the ionic transport calculations in the materials of interest in nonaqueous Li–air batteries, that is, Li_2O_2, Li_2CO_3, and $Li_2O_2@Li_2CO_3$ interface. The coherent electron transport properties with and without lithium vacancies in Li_2O_2 and $Li_2O_2@Li_2CO_3$ interface are discussed in subsection 3.2, while the polaronic conduction in the $Li_2O_2@Li_2CO_3$ interface is detailed in subsection 3.3. Finally, we present our main conclusions in Section 4.

2. CRYSTAL STRUCTURES AND COMPUTATIONAL METHODS

Li_2O_2 crystallizes in a hexagonal crystal structure with lattice parameters $a = b = 3.187$ Å, $c = 7.726$ Å (space group $P6_3/mmc$, see Figure 1a), and it can effectively be viewed as individual peroxide O_2^{2-} ions embedded in sea of Li^+ ions.[14−16]

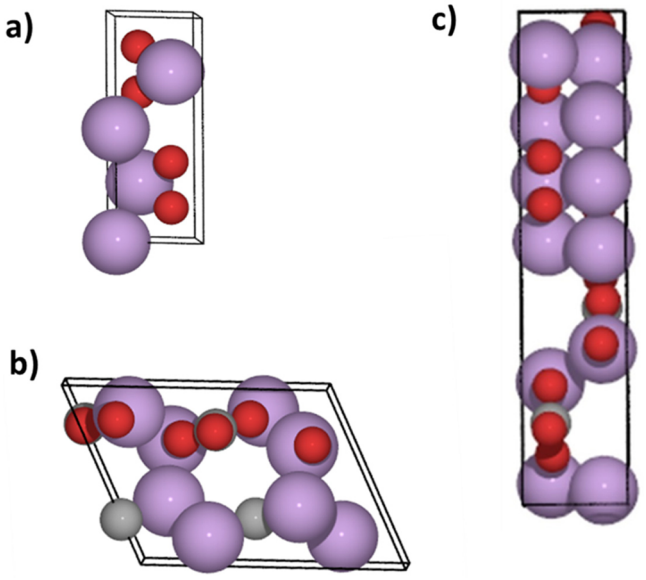

Figure 1. (a) Hexagonal Li_2O_2 structure with lattice parameters $a = b = 3.187$ Å and $c = 7.726$ Å (space group $P6_3/mmc$). (b) Monoclinic Li_2CO_3 structure with space group 15 ($C2/c$) with lattice parameters $a = 8.359$ Å, $b = 4.973$ Å, $c = 6.197$ Å, and $\beta = 114.83°$. (c) Interface, $Li_2O_2@Li_2CO_3$, with 4.8% strains on Li_2O_2.

Moreover, in previous DFT calculations it has been reported that the reconstructed (0001), $(1\bar{1}00)$, and $(1\bar{1}20)$ surfaces are the most stable and predominant exposed facets at operating potentials, being ~80% dominated by (0001) surface.[17,18]

The monoclinic Li_2CO_3 crystal structure with space group $C2/c$ (see Figure 1b) consists of four formula units per unit cell with lattice parameters $a = 8.359$ Å, $b = 4.973$ Å, $c = 6.197$ Å, and $\beta = 114.83°$.[19] The planar CO_3^{-2} groups with C–O bond lengths of 1.284, 1.305, and 1.305 Å are surrounded by the sea of Li^+ ions. The Li^+ and CO_3^{-2} groups are oriented alternatively on the XY plane. Each Li^+ ion is coordinated with four oxygens to form a tetrahedral structure.

The $Li_2O_2@Li_2CO_3$ interface explored in this study is assembled from Li_2CO_3 (adopting a two formula unit cell version of a Li_2CO_3 crystal structure) and Li_2O_2 (adopting a four formula unit cell). The interface is built from a (0001) facet of Li_2O_2 and a (011) facet of Li_2CO_3 with lattice parameters $a = 5.135$ Å, $b = 6.918$ Å, and $c = 16.165$ Å (see Figure 1c). In both components, oxygen-terminated surfaces are used. In the Li_2CO_3 part of the interface, the planes of the carbonate groups are aligned parallel to the peroxides along the z axis. The facets are chosen based on their stability and presence in the discharge products: The (0001) facet is one of the most stable and predominant facets (80%) on Li_2O_2 around the equilibrium potential during discharge and charge in nonaqueous Li–air batteries, with an abundant portion of the oxygen-rich (0001) surface at potentials suitable for charging.[17,18,20] Moreover, the $Li_2CO_3(011)$ surface is one of the low-energy facets,[21] which has an excellent lattice matching with Li_2O_2 (0001). As it can be seen in Figure 1c, the two facets match well and form a stable interface with <5% lattice mismatch (the strain is on Li_2O_2). This setup of the interface contains a relatively small number of atoms (the unit cell contains 28 atoms), which makes the calculations tractable and at the same time provides a reliable description of the interface.

Regarding the polarons and Li vacancy migration studies, all of the calculations are performed within density functional theory (DFT),[22,23] as implemented in the GPAW package[24,25] combined with the Atomic Simulation Environment (ASE).[26] The package uses a real-space grid algorithm based on the projector-augmented wave function method[27] with the frozen core approximation. The revised Perdew–Burke–Ernzehof (RPBE) exchange correlation functional is used in all calculations.[28] For bulk Li_2O_2, we use a $3 \times 3 \times 1$ supercell (72 atoms) with a $3 \times 3 \times 3$ k-point sampling. For bulk Li_2CO_3, we employ a $2 \times 2 \times 2$ supercell (192 atoms) with a $1 \times 2 \times 2$ k-point sampling. The calculations of the ionic transport in the $Li_2O_2@Li_2CO_3$ interface are carried out using the setup previously described (Figure 1c) with $2 \times 2 \times 1$ k-point sampling (112 atoms in the supercell) to minimize the electrostatic interactions between replicas. A similar supercell size is implemented for the polaronic transport calculations study in the $Li_2O_2@Li_2CO_3$ interface.

It has been previously reported that it is necessary to introduce Hubbard corrections to the DFT Hamiltonian to describe properly the localization of polarons using general gradient approximation (GGA) functionals. Following previous works in our group, we use a $U = 6$ eV Hubbard correction applied on the 2p orbitals of carbon and oxygen atoms

The energy barrier, E_b, in both the lithium diffusion and polaronic (hole and electron) hopping is calculated using the climbing image nudged elastic band method (CI-NEB).[29−31] All ground-state energies are determined when Hellmann–

DOI: 10.1021/acs.jpcc.5b04432
J. Phys. Chem. C 2015, 119, 18066−18073

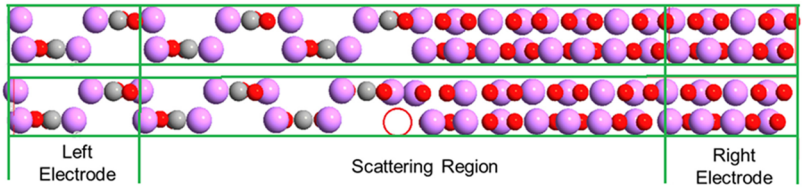

Figure 2. Structural setup for the device region for the pristine interface Li_2O_2@Li_2CO_3 (upper) and with a Li vacancy at the peroxide part of the interface, Li_2O_2 vac@Li_2CO_3 (lower).

Feynman forces are <0.03 eV/Å. All of the atoms in the supercell are free to relax during the optimization. From the computed E_b, it is possible to obtain the rate (r) and the diffusion coefficient (D) using the relations $r = \nu e^{-E_b/k_BT}$ and $D = a^2 r$, respectively, where ν is the hopping rate (in this work we use $\nu = 10^{13}$ s^{-1}) and a is the jump length.

The coherent electronic transport calculations in the tunneling regime are carried out using the Nonequilibrium Green's function (NEGF) formalism. The calculations are performed using a localized linear combination of atomic orbitals (LCAO) basis set (double-ζ plus polarization quality basis for all atomic species), as implemented in the Atomistix ToolKit (ATK)[32−34] package, where a central device region (or scattering region) is connected to two semi-infinite leads, which are kept at fixed electronic chemical potentials, μ_L and μ_R, respectively, to simulate an applied bias voltage across the device region given by $V = (\mu_L - \mu_R)/e$. The scattering region describing the Li_2O_2@Li_2CO_3 interface contains four formula units of Li_2CO_3 and eight formula units of Li_2O_2. The electrode regions consist of two formula units of bulk Li_2CO_3 (left lead) and four formula units of Li_2O_2 (right lead). For the sake of consistency, RPBE exchange correlation functional is employed. A 4 × 6 × 100 k-point sampling is used during the NEGF self-consistent loop. In the finite bias calculations, a positive bias is defined as sending electrons from the left lead to the right lead (see Figure 2).

3. RESULTS AND DISCUSSION

Here the main results and discussions are presented in three subsections as shown later. The first subsection (3.1) covers the ionic transport calculations in the bulk Li_2O_2, Li_2CO_3, and Li_2O_2@Li_2CO_3 interface. The coherent electron transport properties with and without lithium vacancies in Li_2O_2 and Li_2O_2@Li_2CO_3 interface are discussed in subsection 3.2, while the polaronic conduction in the Li_2O_2@Li_2CO_3 interface is detailed in subsection 3.3.

3.1. Ionic Transport in Li_2O_2, Li_2CO_3, and Li_2O_2@Li_2CO_3 Interface. In this subsection, the details of the lithium vacancy diffusion in bulk Li_2O_2, Li_2CO_3, and Li_2O_2@Li_2CO_3 interface across various pathways are discussed. Lithium vacancies, V^0_{Li}, are modeled by removing a single Li atom from a supercell and subsequently relaxing the system internally. Here we analyze the effect of neutral vacancies, but positive (V^{+1}_{Li}) and negatively charged vacancies (V^{-1}_{Li}) can also be present, depending on the potential.[35] For lithium diffusion studies, a single Li atom is removed from the corresponding supercells with a total vacancy concentration [V^0_{Li}] of 2.78, 1.6, and 2% in the peroxide, carbonate, and interface systems, respectively. We have checked that the formation energy of a second [V^0_{Li}] vacancy in all of the systems is practically the same as that of the first [V^0_{Li}] vacancy; that is, the formation energy of the vacancies is nearly independent of their concentration.

In Li_2O_2, there are four possible inequivalent hops in the intralayer direction (in the XY plane, see Figure 4), namely,

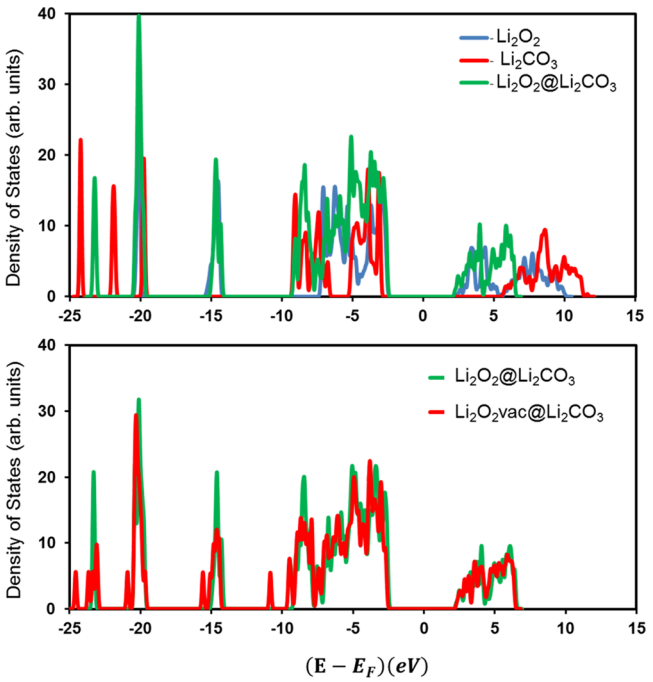

Figure 3. Total density of states (DOS) relative to the Fermi energy for (a) pristine Li_2O_2, Li_2CO_3, and Li_2O_2@Li_2CO_3 and (b) pristine Li_2O_2@Li_2CO_3 and with a defect (neutral Li vacancy, V^0_{Li}) at the peroxide part of the interface Li_2O_2 vac@Li_2CO_3 is obtained using RPBE + U (U = 6 eV).

BE(X) and AD(X) in the X direction and AF(Y) and BG(Y) in the Y direction, being in all of the cases the energy barriers close to 1 eV. Regarding the interlayer diffusion (in Z direction), there are two possible inequivalent hops, namely, AB(Z) and BC(Z). We find E_b = 0.44 eV and the E_b = 0.36 eV for AB(Z) hop and BC(Z) hop, respectively, giving an average E_b = 0.40 eV. Thus, it is clear that V^0_{Li} diffusion has a preferential channel in the Z direction. The microscopic diffusion channel follows A → B → C series along the Z direction with an average rate of $r = 2 \times 10^6$ s^{-1} and a diffusion coefficient of $D = 1.5 \times 10^{-9}$ cm^2/s. This relatively small barrier in the Z direction opens the possibility of V^0_{Li} diffusion under ambient conditions (For more details, see ref 36.)

We have conducted a similar analysis in Li_2CO_3, studying five different possible hops (see Figure 5). As it can be seen in Figure 5, the NEB calculations show low-energy barriers, that is, ~0.2 eV, for V^0_{Li} vacancy diffusion in all directions (X, Y, and Z). The most plausible diffusion channel follows the D → A hop in the Y direction, while the C → E hop is preferred in the Z direction and the A → B → C (D → A = B → C) hop

DOI: 10.1021/acs.jpcc.5b04432
J. Phys. Chem. C 2015, 119, 18066−18073

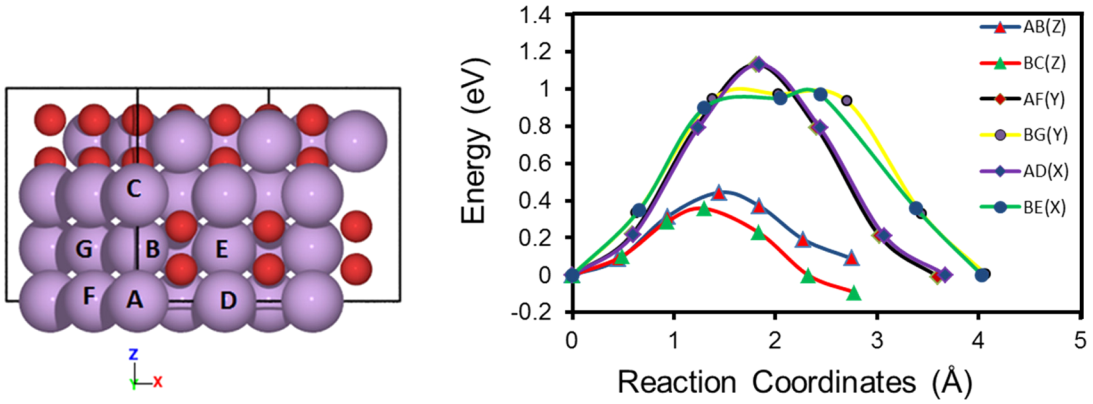

Figure 4. Calculated NEB paths for migration of neutral Li-vacancies, V^0_{Li}, following various diffusion paths in bulk Li_2O_2 using a 3 × 3 × 1 supercell. The minimum barrier is found to be 0.35 eV.

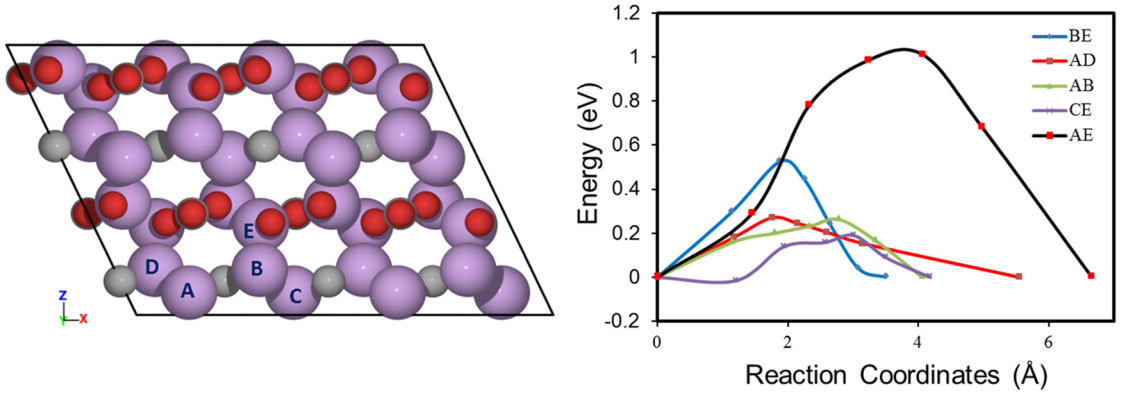

Figure 5. Calculated NEB paths for migration of neutral Li vacancies, V^0_{Li}, following various diffusion paths in bulk Li_2CO_3. The minimum barrier is found to be 0.20 eV.

sequence is favored in the X direction. The average rate (r) of Li vacancy diffusion in Li_2CO_3 yields $r = 9 \times 10^8$ s^{-1} with a corresponding diffusion coefficient of $D = 1.6 \times 10^{-6}$ cm^2/s.

The formation energies of V^0_{Li} vacancies relative to metallic lithium in Li_2O_2 bulk and Li_2CO_3 bulk are 3.00 and 4.20 eV, respectively, whereas the formation energies of V^0_{Li} vacancies at the Li_2O_2@Li_2CO_3 interface are 2.71 eV in the Li_2O_2 part of the interface and 3.24 eV in the Li_2CO_3 part. This means that in both materials vacancies will accumulate at the Li_2O_2@Li_2CO_3 interface rather than in their respective bulk. We have also calculated that there is no barrier to move V^0_{Li} vacancies from the Li_2CO_3 part of the interface to the Li_2O_2, suggesting that V^0_{Li} vacancies will tend to pile in the latter (see Figure 6). This also implies that the presence of the interface will not cause the ionic conductivity to become rate-limiting under practical operating conditions in Li−O_2 batteries.

The relatively large V^0_{Li} vacancy formation energy could lead us to think that the concentration of these vacancies should be negligible; however, it should be noted that the concentration of V^0_{Li} vacancies should be estimated using the formation energies at the working potentials of the battery. Varley et al.[35] and Radin et al.[36] have shown that at these potential V^0_{Li} vacancy formation energies are much lower, leading to a sufficient concentration to have significant ionic conduction.

3.2. Coherent Electron Transport in Li_2O_2 and Li_2O_2@Li_2CO_3 Interface. It is instructive to examine the density of states (DOS) of Li_2O_2 and Li_2CO_3 bulks and compare them with the one of the interface to have a comprehensive understanding of the coherent electron transport at the

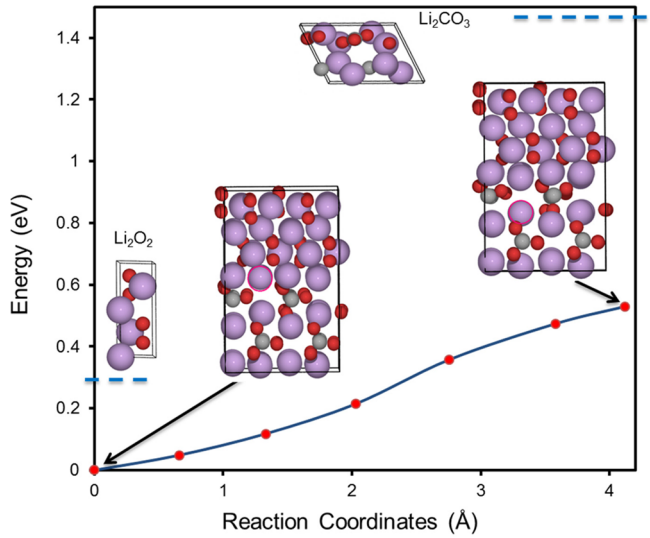

Figure 6. NEB calculations for the Li vacancy diffusion barrier at the $Li_2O_2(0001)$@$Li_2CO_3(011)$ interface. The thermodynamic barrier is found to be 0.53 eV going from the peroxide to the carbonate; the blue dashed lines represent the vacancy formation energies of bulk Li_2O_2 (+0.3 eV) and Li_2CO_3 (+∼1 eV) relative to the interface values.

Li_2O_2@Li_2CO_3 interface. In Figure 3 we can see that both Li_2O_2 and Li_2CO_3 are both wide bandgap insulators with calculated band gaps (using RPBE+U functional with U = 6 eV) of 5.03 eV for Li_2O_2 and 8.01 eV for Li_2CO_3. The Li_2O_2@

DOI: 10.1021/acs.jpcc.5b04432
J. Phys. Chem. C 2015, 119, 18066−18073

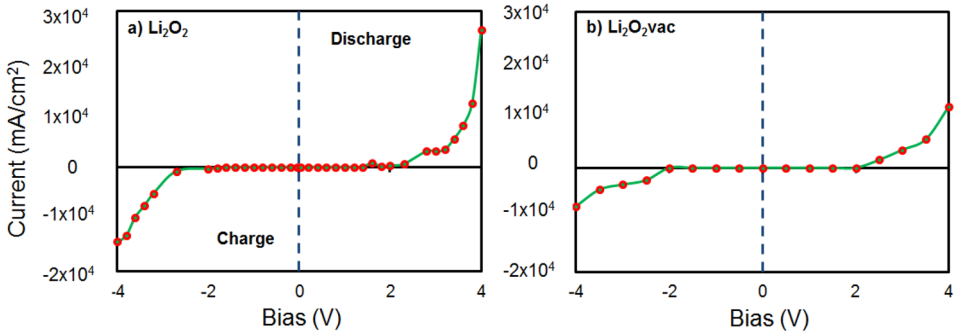

Figure 7. Calculated $I-V$ curves from ATK using the RPBE exchange correlation functional with k-point sampling $4 \times 6 \times 100$ using an electronic temperature of 300 K for (a) pristine Li_2O_2 and (b) in the presence of a neutral lithium vacancy.

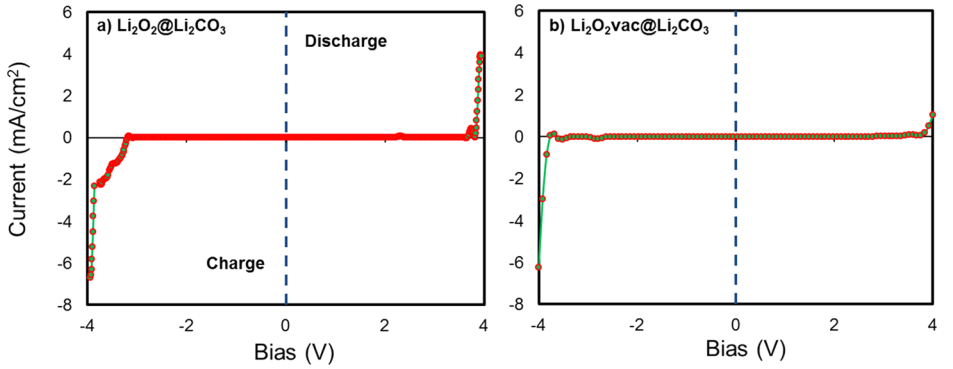

Figure 8. Calculated $I-V$ curves for (a) pristine $Li_2O_2(0001)@Li_2CO_3(011)$ and (b) with a neutral lithium vacancy at the $Li_2O_2(0001)$ vac@ $Li_2CO_3(011)$ interface.

Table 1. Energy Difference between the Localized (Polaron) and Delocalized States ($\Delta E_{loc\text{-}del}$) in Electronvolts for the Li_2O_2@ Li_2CO_3 Interface[a]

method	hole polaron in the Li_2O_2 part	hole polaron in the Li_2CO_3 part	electron polaron in the Li_2O_2 part	electron polaron in the Li_2CO_3 part
RPBE	delocalized	delocalized	delocalized	delocalized
RPBE+U (U = 6 eV)	−1.40	−0.57	−2.57	−2.67

[a]Hole and excess electron are localized at the Li_2O_2 and Li_2CO_3 parts of the interface using RPBE + U (U = 6 eV), as shown in Table 1.

Li_2CO_3 interface shows a 4.82 eV band gap (very close to the one of pristine Li_2O_2 bulk), and it can be viewed as the superposition of individual DOS of the Li_2O_2 and Li_2CO_3, with no presence of midgap interface states. In this situation it is expected that for bias voltages (negative or positive) around 2 to 2.5 eV (i.e., half of the bandgap of Li_2O_2) we will start to see a relative good conductance in the Li_2O_2 bulk; however, for the same bias we will expect a drastic drop in the conductance at the $Li_2O_2@Li_2CO_3$ interface because there are no Li_2CO_3 levels at these energies.

Regarding the presence of vacancies in Li_2O_2 bulk and at the $Li_2O_2@Li_2CO_3$ interface (vacancies are located at the Li_2O_2 part of the interface, following the results in Section 3), the DOS of both defect systems reveals that the vacancy levels pin the Fermi level of the pristine systems. This implies that V^0_{Li} vacancies are not going to open new electron tunneling channels in these systems, and they are going to have a detrimental effect in the conductivity due to their action as scattering centers.

To check the plausibility of these assumptions, we have performed DFT-NEGF calculations, as described in Section 2. We can see in Figure 7a that a significant current (~10 mA/cm^2) begins to show up just around ±2.0 V in pristine Li_2O_2 bulk; however, the current at the interface only starts rising at higher potentials (above ±3.80 V) due to the wider gap of Li_2CO_3 (see Figure 8). We also observe that the current at relevant voltages is reduced 3 orders of magnitude with respect to the one in Li_2O_2 bulk. Furthermore, V^0_{Li} vacancies reduce the currents at relevant voltages, of both Li_2O_2 bulk and $Li_2O_2@Li_2CO_3$ interface, by a factor of 2. In summary, we can conclude that the presence of $Li_2O_2@Li_2CO_3$ interfaces and V^0_{Li} vacancies in Li_2O_2 has a substantial negative effect on the coherent electronic transport at the oxygen electrode of Li−O_2 batteries.

3.3. Polaronic Transport in $Li_2O_2@Li_2CO_3$ Interface. We have already reported that both Li_2O_2 and Li_2CO_3 bulks can hold hole polarons with sufficiently low migration barriers (0.39 eV for the former and 0.55 eV for the latter) to become an alternative path for electronic transport.[37] We also found that both materials can hold excess electron polarons; however, the migration barriers for electron polarons are much higher than those of hole polarons (1.408 eV in Li_2O_2 and 1.05 in Li_2CO_3). Here we will focus on polaronic conduction (for both holes and excess electrons) at the $Li_2O_2@Li_2CO_3$ interface.

When we consider polaron localization at the Li_2O_2 part of the interface we observe that the hole (excess electron) polaron

DOI: 10.1021/acs.jpcc.5b04432
J. Phys. Chem. C 2015, 119, 18066−18073

is localized by shortening (stretching) the bond length of one of the O−O peroxide bond from 1.55 to 1.33 Å (2.45 Å). The localization can also take place at the Li_2CO_3 part of the interface. In this case the hole (excess electron) is localized in one of the carbonate ions that shortens (stretches) its C−O bond lengths from an average of 1.31 Å to an average of 1.23 Å (1.35 Å). Apart from the geometry distortions we observe in all of the cases the appearance of a magnetic moment in the oxyanions, which is another footprint of the hole (excess electron) localization. These localized states are more stable than the delocalized ones, and particularly the electron polaron is found to be strongly localized, that is, by >2 eV relative to the delocalized state (see Table 1). All of these features are very similar to the ones we found for Li_2O_2 and Li_2CO_3 bulks.[37]

It is interesting to notice that hole polarons are more stable in the Li_2O_2 part of the Li_2O_2@Li_2CO_3 interface by 0.83 eV, whereas the excess electron polarons are more stable in the Li_2CO_3 part by 0.10 eV (see Table 1 and Figure 9). This is due

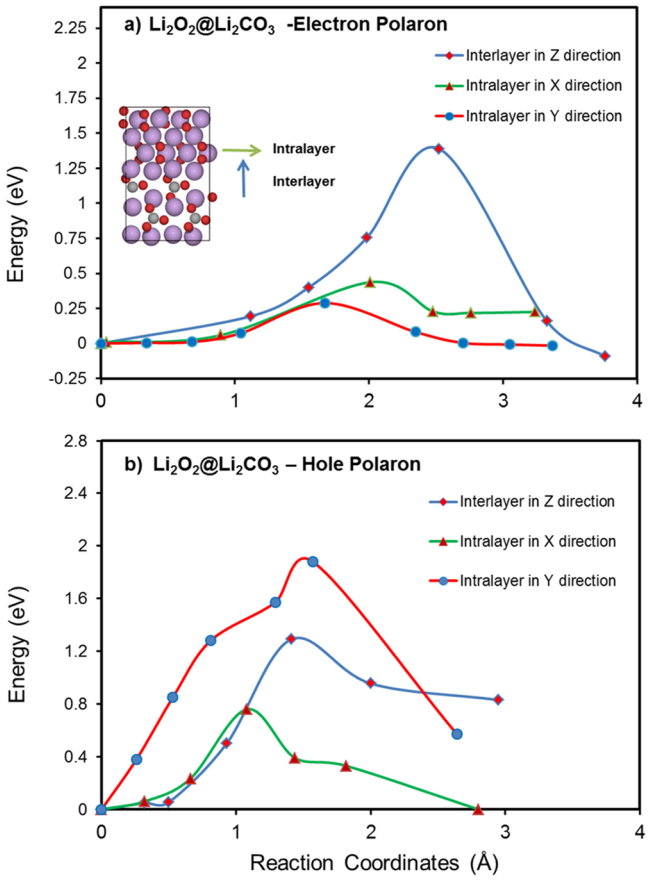

Figure 9. Calculated polaron hopping paths using the NEB method along the intralayer in X and Y directions and interlayer along Z direction in a 2 × 2 × 1 Li_2O_2@Li_2CO_3 interface supercell. Energies are obtained from RPBE + U (U = 6 eV) method for (a) excess electron and (b) hole.

to the different magnitude of the distortions in the peroxide ions of Li_2O_2; that is, a hole localized in a peroxide ion involves a change in the O−O bonding distance of 0.2 Å, while the localization of an excess electron requires stretching the bonding by 0.9 Å.

Accordingly to the NEB calculations, the energy barriers for the polaronic transport of excess electrons across the interface (see direction z in Figure 9) are very similar to the ones observed in Li_2O_2 and Li_2CO_3 bulks. The barrier for transporting excess electron polarons from Li_2O_2 to Li_2CO_3 is 1.39 eV (and 1.48 eV from Li_2CO_3 to Li_2O_2), very close to the 1.41 eV in Li_2O_2 bulk and 1.05 in Li_2CO_3 bulk. This implies that the excess electron polaronic transport across Li_2O_2@Li_2CO_3 interfaces is an inaccessible channel for electronic transport. The polaron hopping barrier for holes is much more asymmetric: the barrier for the hop from Li_2CO_3 to Li_2O_2 to is 0.4 eV (in Li_2O_2 bulk is 0.39 eV), while it is 1.3 eV in the opposite direction. In this scenario we can conclude that Li_2O_2@Li_2CO_3 interfaces act like a diode, which allows hole polaronic transport only from the Li_2CO_3 part of the interface to the Li_2O_2 one.

Regarding the polaronic transport parallel to the Li_2O_2@Li_2CO_3 interface we observe that an alternative channel for electron polaron hopping opens within the peroxide part of the interface (intralayer in the X and Y directions in Figure 9) with a low hopping barrier of <0.5 eV, providing an improved conduction channel compared with bulk Li_2O_2. The corresponding rates (r) in X and Y intralayer electron polaron hopping are found to be 5 × 10^5 and 9 × 10^7 s^{-1} with the diffusion coefficients of 5 × 10^{-10} and 1 × 10^{-7} cm^2/s, respectively. By contrast, the hole polaron hopping barriers parallel to the Li_2O_2@Li_2CO_3 interface are significantly larger compared with the low barriers reported for bulk Li_2O_2 by Garcia-Lastra et al.[37] (The barriers at the interface are at least two times larger than in bulk Li_2O_2.)

4. CONCLUSIONS

The detailed understanding of charge carrier transport across the Li_2O_2@Li_2CO_3 interfaces can shed new light on the limited performance of nonaqueous Li−O_2 batteries. DFT+U and NEGF's calculations have been applied to study the neutral lithium vacancy and electron/hole polaron migration barriers and I−V curves of the Li_2O_2 and Li_2O_2@Li_2CO_3 interface with and without defects. The role of Li vacancies in the cycling process is investigated and found to be prone to trapping at the peroxide part of the interface based on the relative vacancy formation energies, resulting in substantial reduction in the coherent transport. According to NEB calculations, the Li vacancy diffusion revealed low-energy barriers both across and parallel to the interface. The hole polaron conduction seems to be limited at the interface compared with values obtained for Li_2O_2.[37] The NEGF calculations also showed that the coherent transport is reduced due to the presence of interfaces and defects; however, low electron polaron hopping barriers are revealed in the plane parallel to the interface, opening an alternative conduction pathways, which may improve the electronic conduction under charge/discharge conditions, where the electron polaron formation energy is low and the concentration near the interface is consequently expected to be high.[35] Experimental realization of such well-defined interfaces may prove highly challenging, but this effect could possibly be investigated using nanostructured cathodes, (e.g., pillared graphene nanostructures as recently tested for Li-ion battery anodes[38]). In this case, alternating between electrochemical discharge (leading to Li_2O_2 formation) and short rest periods allowing some level of chemical degradation to form Li_2CO_3 inclusions should allow for a sufficient number of Li_2O_2@Li_2CO_3 interfaces capable of supplying the required electronic conduction to fill the space between the nanopillars.

DOI: 10.1021/acs.jpcc.5b04432
J. Phys. Chem. C 2015, 119, 18066−18073

AUTHOR INFORMATION

Corresponding Author

*E-mail: teve@dtu.dk.

Notes

The authors declare no competing financial interest.

ACKNOWLEDGMENTS

We acknowledge support of this work from the ReLiable project (project nr. 11-116792/0603-00462B) funded by the Danish Council for Strategic Research - Programme Commission on Sustainable Energy and Environment under the Danish Innovation Foundation, as well as the European Union's Seventh Framework Programme (FP7/2007-2013) under grant agreement no. 608575. J.M.G.-L. acknowledges support from the Spanish Ministry of Economy and Competitiveness under projects FIS2012-30996 and FIS2010-21282-C02-01 and from the Mat4Bat project founded by Villum Foundation Young Investigators Program (Project No. 10096). We also would like to thank Prof. Alan C. Luntz and Dr. Umberto M. Pozzoni for the constructive discussions we had.

REFERENCES

(1) Tarascon, J. M.; Armand, M. Issues and Challenges Facing Rechargeable Lithium Batteries. *Nature* **2001**, *414*, 359−367.

(2) Armand, M.; Tarascon, J. M. Building Better Batteries. *Nature* **2008**, *451*, 652−657.

(3) Balaish, M.; Kraytsberg, A.; Ein-Eli, Y. A Critical Review on Lithium-Air Battery Electrolytes. *Phys. Chem. Chem. Phys.* **2014**, *16*, 2801−2822.

(4) Mccloskey, B. D.; Speidel, A.; Scheffler, R.; Miller, D. C.; Viswanathan, V.; Hummelshøj, J. S.; Nørskov, J. K.; Luntz, A. C. Twin Problems of Interfacial Carbonate Formation in Nonaqueous Li−O_2 Batteries. *J. Phys. Chem. Lett.* **2012**, *3*, 997−1001.

(5) Younesi, R.; Hahlin, M.; Bjorefors, F.; Johansson, P.; Edstrom, K. Li−O_2 Battery Degradation by Lithium Peroxide (Li_2O_2): A Model Study. *Chem. Mater.* **2013**, *25*, 77.

(6) Xu, W.; Hu, J.; Engelhard, M. H.; Towne, S. A.; Hardy, J. S.; Xiao, J.; Feng, J.; Hu, M. Y.; Zhang, J.; Ding, F.; et al. The Stability of Organic Solvents and Carbon Electrode in Nonaqueous Li−O_2 Batteries. *J. Power Sources* **2012**, *215*, 240−247.

(7) Viswanathan, V.; Thygesen, K. S.; Hummelshøj, J. S.; Nørskov, J. K.; Girishkumar, G.; McCloskey, B. D.; Luntz, A. C. Electrical Conductivity in Li_2O_2 and Its Role in Determining Capacity Limitations in Non-Aqueous Li−O_2 Batteries. *J. Chem. Phys.* **2011**, *135*, 214704.

(8) Mekonnen, Y. S.; Knudsen, K. B.; Mýrdal, J. S. G.; Younesi, R.; Højberg, J.; Hjelm, J.; Norby, P.; Vegge, T. Communication: The Influence of CO_2 Poisoning on Overvoltages and Discharge Capacity in Non-Aqueous Li-Air Batteries. *J. Chem. Phys.* **2014**, *140*, 121101.

(9) Højberg, J.; McCloskey, B. D.; Hjelm, J.; Vegge, T.; Johansen, K.; Norby, P.; Luntz, A. C. An Electrochemical Impedance Spectroscopy Investigation of the Overpotentials in Li−O_2 Batteries. *ACS Appl. Mater. Interfaces* **2015**, *7*, 4039−4047.

(10) Albertus, P.; Girishkumar, G.; McCloskey, B.; Sánchez-Carrera, R. S.; Kozinsky, B.; Christensen, J.; Luntz, A. C. Identifying Capacity Limitations in the Li/Oxygen Battery Using Experiments and Modeling. *J. Electrochem. Soc.* **2011**, *158*, A343−A351.

(11) Shi, S.; Qi, Y.; Li, H.; Hector, L. G. Defect Thermodynamics and Diffusion Mechanisms in Li_2CO_3 and Implications for the Solid Electrolyte Interphase in Li-Ion Batteries. *J. Phys. Chem. C* **2013**, *117*, 8579−8593.

(12) Fracassi, P. F.; Klein, M. L.; Della Valle, R. G. Lattice Dynamics of Ionic Molecular Crystals in the Rigid Ion Approximation, Phases II and III of Sodium Superoxide. *Canada J. Phys.* **1984**, *62*, 54−64.

(13) Chen, J.; Hummelshøj, J. S.; Thygesen, K. S.; Myrdal, J. S. G.; Nørskov, J. K.; Vegge, T. The Role of Transition Metal Interfaces on the Electronic Transport in Lithium−air Batteries. *Catal. Today* **2011**, *165*, 2−9.

(14) Cota, L. G.; De La Mora, P. On the Structure of Lithium Peroxide, Li_2O_2. *Acta Crystallogr., Sect. B: Struct. Sci.* **2005**, *B61*, 133−136.

(15) Hummelshøj, J. S.; Blomqvist, J.; Datta, S.; Vegge, T.; Rossmeisl, J.; Thygesen, K.; Luntz, A. C.; Jacobsen, K. W.; Nørskov, J. K. Communication: Elementary Oxygen Electrode Reactions in the Aprotic Li-Air Battery. *J. Chem. Phys.* **2010**, *132*, 071101.

(16) Garcia-Lastra, J. M.; Bass, J. D.; Thygesen, K. S. Communication: Strong Excitonic and Vibronic Effects Determine the Optical Properties of Li_2O_2. *J. Chem. Phys.* **2011**, *135*, 121101.

(17) Radin, M. D.; Tian, F.; Siegel, D. J. Electronic Structure of Li_2O_2 {0001} Surfaces. *J. Mater. Sci.* **2012**, *47*, 7564−7570.

(18) Hummelshøj, J. S.; Luntz, a C.; Nørskov, J. K. Theoretical Evidence for Low Kinetic Overpotentials in Li−O_2 Electrochemistry. *J. Chem. Phys.* **2013**, *138*, 034703.

(19) Effenberger, H.; Zemann, J. Refining the Crystal-Structure of Lithium-Carbonate, Li_2CO_3. *Z. Kristallogr.* **1979**, *150*, 133−138.

(20) Mo, Y.; Ong, S. P.; Ceder, G. First-Principles Study of the Oxygen Evolution Reaction of Lithium Peroxide in the Lithium-Air Battery. *Phys. Rev. B: Condens. Matter Mater. Phys.* **2011**, *84*, 205446.

(21) Bruno, M.; Prencipe, M. Ab Initio Quantum-Mechanical Modeling of the (001), and (110) Surfaces of Zabuyelite (Li_2CO_3). *Surf. Sci.* **2007**, *601*, 3012−3019.

(22) Ernzerhof, M.; Scuseria, G. E. Perspective on "Inhomogeneous Electron Gas". *Theor. Chem. Acc.* **2000**, *103*, 259−262.

(23) Kohn, W.; Sham, L. J. Self-Consistent Equation Including Exchange and Correlation Effects. *Phys. Rev.* **1965**, *140*, A1133−A1138.

(24) Mortensen, J. J.; Hansen, L. B.; Jacobsen, K. W. A Real-Space Grid Implementation of the Projector Augmented Wave Method. *Phys. Rev. B: Condens. Matter Mater. Phys.* **2005**, *71*, 035109.

(25) Enkovaara, J.; Rostgaard, C.; Mortensen, J. J.; Chen, J.; Dułak, M.; Ferrighi, L.; Gavnholt, J.; Glinsvad, C.; Haikola, V.; Hansen, H. a; et al. Electronic Structure Calculations with GPAW: A Real-Space Implementation of the Projector Augmented-Wave Method. *J. Phys.: Condens. Matter* **2010**, *22*, 253202.

(26) Bahn, S. R.; Jacobsen, K. W. An Object-Oriented Scripting Interface to a Legacy Electronic Strcture Code. *Comput. Sci. Eng.* **2002**, *4*, 56−66.

(27) Blochl, P. E. Projected Augmented-Wave Method. *Phys. Rev. B: Condens. Matter Mater. Phys.* **1994**, *50*, 17953−17979.

(28) Hammer, B.; Hansen, L.; Nørskov, J. Improved Adsorption Energetics within Density-Functional Theory Using Revised Perdew-Burke-Ernzerhof Functionals. *Phys. Rev. B: Condens. Matter Mater. Phys.* **1999**, *59*, 7413−7421.

(29) Henkelman, G.; Jonsson, H. Improved Tangent Estimate in the Nudged Elastic Band Method for Finding Minimum Energy Paths and Saddle Points. *J. Chem. Phys.* **2000**, *113*, 9978−9985.

(30) Hanggi, P.; Talkner, P.; Borkovec, M. Reaction-Rate Theory: Fifty Years after Kramers. *Rev. Mod. Phys.* **1990**, *62*, 251−342.

(31) Vegge, T.; Rasmussen, T.; Leffers, T.; Pedersen, O.; Jacobsen, K. Determination of the of Rate Cross Slip of Screw Dislocations. *Phys. Rev. Lett.* **2000**, *85*, 3866−3869.

(32) Atomistix ToolKit version 2014.1, QuantumWise A/S (www.quantumwise.com).

(33) Brandbyge, M.; Mozos, J.-L.; Ordejón, P.; Taylor, J.; Stokbro, K. Density-Functional Method for Nonequilibrium Electron Transport. *Phys. Rev. B: Condens. Matter Mater. Phys.* **2002**, *65*, 165401.

(34) Soler, J. M.; Artacho, E.; Gale, J. D.; Garcia, A.; Junquera, J.; Ordejon, P.; Sanchez-Portal, D. The SIESTA Method for Ab Initio Order-N Materials Simulation. *J. Phys.: Condens. Matter* **2002**, *14*, 2745−2779.

(35) Varley, J. B.; Viswanathan, V.; Nørskov, J. K.; Luntz, a. C. Lithium and Oxygen Vacancies and Their Role in Li_2O_2 Charge Transport in Li−O_2 Batteries. *Energy Environ. Sci.* **2014**, *7*, 720−727.

DOI: 10.1021/acs.jpcc.5b04432
J. Phys. Chem. C 2015, 119, 18066−18073

(36) Radin, M. D.; Siegel, D. J. Charge Transport in Lithium Peroxide: Relevance for Rechargeable Metal−air Batteries. *Energy Environ. Sci.* **2013**, *6*, 2370−2379.
(37) Garcia-Lastra, J. M.; Myrdal, J. S. G.; Christensen, R.; Thygesen, K. S.; Vegge, T. DFT+U Study of Polaronic Conduction in Li_2O_2 and Li_2CO_3: Implications for Li-Air Batteries. *J. Phys. Chem. C* **2013**, *117*, 5568−5577.
(38) Wang, W.; Ruiz, I.; Guo, S.; Favors, Z.; Bay, H. H.; Ozkan, M.; Ozkan, C. S. Hybrid Carbon Nanotube and Graphene Nanostructures for Lithium Ion Battery Anodes. *Nano Energy* **2014**, *3*, 113−118.

DOI: 10.1021/acs.jpcc.5b04432
J. Phys. Chem. C 2015, 119, 18066−18073

Paper III

Thermodynamic and Kinetic Limitation of Sodium Peroxide and Formation of Sodium Superoxide in Na-O_2 Batteries (*to be submitted*)

Yedilfana S. Mekonnen, Rune Christensen, Juan M. Garcia-Lastra, Tejs Vegge

Thermodynamic and Kinetic Limitations for Peroxide and Superoxide Formation in Na−O_2 Batteries

Yedilfana S. Mekonnen[1], Rune Christensen[1], Juan M. Garcia-Lastra[1], Tejs Vegge[1*]

[1]Department of Energy Storage, Technical University of Denmark, Fysikvej, Building 309, 2800 Kgs Lyngby, Denmark

[*]Corresponding Author E-mail: teve@dtu.dk

Abstract

The Na−O_2 system holds great potential as a low cost, high energy density battery, but under normal operating conditions, the main discharge product is sodium superoxide (NaO_2), whereas the high capacity peroxide (Na_2O_2) remains elusive. Here, we apply density functional theory calculations to determine equilibrium potentials and free energies as a function of temperature for the different phases of NaO_2 and Na_2O_2, using an improved metal chloride correction scheme, showing the high temperature cubic NaO_2 phase to be the thermodynamically preferred discharge product up to ~120 K, after which Na_2O_2 is thermodynamically preferred. We also investigate the reaction mechanisms and resulting overpotentials on stepped model surfaces of the NaO_2 and Na_2O_2 systems, showing low overpotentials for NaO_2 formation (0.18 V) and depletion (0.14 V), which are in excellent agreement with experiments, whereas the overpotentials for Na_2O_2 formation (0.3 V) and depletion (0.5 V) are found to be prohibitively high. These findings are in excellent agreement with experimental data on the thermodynamic properties of the Na_xO2 species and provide the first kinetic explanation for why NaO_2 is the main discharge product in Na-O_2 batteries under normal operating conditions.

Key Words: NaO_2, Na_2O_2, Na-O_2 batteries, DFT, Thermodynamic and Kinetic, Overpotential

I. Introduction

In the last decade, significant efforts have been paid to the development of next generation batteries. In particular metal-air batteries (Li-, Na-, Mg-, Al-, Fe- and Zn$-O_2$ batteries) in either aqueous or non-aqueous (aprotic) electrolytes have gained a lot of attention,[1,2] e.g. for use in electric vehicles. The cost of commercially available Li-ion batteries is generally too high and the energy storage capacity too low to solve the increasing demands on batteries for transportation [3]. Metal-air batteries have high theoretical specific energies since the technology, once it is mature, would apply metal as an anode and oxygen gas from air on the cathode side. The reaction products are peroxides and/or superoxides during discharge depending on the experimental conditions and cell components used in the system. The oxygen reduction (ORR) and oxygen evolution reaction (OER) are the two main reactions taking place reversibly during discharge and charging, respectively. However, metal-air battery technologies are limited by a number of drawbacks and challenges, which must be resolved before becoming commercially viable, *i.e.*, low accessible capacity (sudden death), poor electronic conductivity and rechargeability, limited chemical and electrochemical stability of electrodes, electrolytes [4], salts [5] and high sensitivity to air impurity-like water and CO_2. [6,7,8,9,10]

Among the battery systems reported so far, the Li$-O_2$ couple offers higher equilibrium potential (~2.96 V) and extremely high specific capacity (~3,842 mAh/g), which is comparable to gasoline [11] and nearly an order of magnitude higher than that of current Li-ion batteries [12]. However, in practice non-aqueous Li-O_2 batteries suffer from poor rechargeability and high overpotentials, particularly at charging process. [13] Although the capacity and equilibrium potential is lower, the Na$-O_2$ battery technology displays some advantages over the Li$-O_2$ battery and other similar batteries. The non-aqueous secondary Na$-O_2$ battery operates at low dis/charge overpotentials (< 200 mV) even at higher current densities (0.2 mA/cm^2) and yields high electrical energy efficiency (90 %), which is consistently observed for many cycles.[14,15,16]. The theoretical specific capacity of the Na$-O_2$ battery is ~1,500 mAh/g [16] when NaO_2 deposited on carbon nanotubes. This is lower compared to the Li$-O_2$, but still higher than the existing Li-ion batteries; at least twice the Li-ion batteries, which is about half of the state of the art Li$-O_2$ battery specific capacity. If, however, Na_2O_2 can be formed reversibly, it would be possible to increase the specific capacity to ~2,800 mAh/g. [17]

Among the battery systems reported so far, the Li−O_2 couple offer higher equilibrium potential (~2.96 V) and extremely high specific capacity (~3842 mAh/g), which is comparable to gasoline [11] and nearly an order of magnitude higher than that of current Li-ion batteries [12]. However, in practice nonaqueous Li-O_2 batteries suffer from poor rechargeability and high overpotential particularly at the charging process. Although the capacity and equilibrium potential is lower, the Na−O_2 battery technology displays some advantages over the Li−O_2 battery and other similar batteries. The nonaqueous rechargeable Na−O_2 battery operates at low dis/charge overpotentials (< 200 mV) even at higher current densities (0.2 mA/cm^2) and yield high electrical energy efficiency (90 %), which is consistently observed for many cycles.[14,15,16]. The theoretical specific capacity the Na−O_2 battery is about 1500 mAh/g [16] when NaO_2 is grown on carbon nanotubes which is lower compared to the Li−O_2 but still higher than the existing Li-ion batteries, at least twice the Li-ion batteries, which is about half of the state of the art Li−O_2 battery specific capacity. If, however, Na_2O_2 can be formed reversibly, it would be possible to increase the specific capacity to 2800 mAh/g. [17]

Hartmann *et al*. [15,18] and McCloskey *et al*. [19] have reported sodium superoxide (NaO_2) as the dominant reaction product. Whereas, Kim *et al.* [17] have reported sodium peroxide (Na_2O_2) as dominant discharge product instead. Poor rechargeability (< 10 cycles) and high charging overpotential (> 1.3 V) is exhibited when Na_2O_2 is formed at the cathode at room temperature, which is also similar to the challenges observed in Li−O_2 system. However, sufficiently low dis/charge overpotentials and interestingly high rechargeability are observed when NaO_2 is formed [16].

Scanning electron microscopy (SEM) image have revealed that highly ordered cubic NaO_2 is grown at the carbon cathode surface. [15,19,18] A recent computational study by Ceder *et al.* reports that NaO_2 is more stable at the nanoscale level (up to about 5 nm), whereas bulk Na_2O_2 is thermodynamically stable at standard conditions (in agreement with experimental observations). For electrochemical growth during battery discharge, the size of the NaO_2 particles is, however, found in the micrometer size (1-50 micro meters).[15] The size of the particle cannot be explained from the effect of the differences in surface energy, nor the effect of e.g. oxygen partial pressure or temperature, which may lead to the formation of larger NaO_2 particles (up to 20 nm based on the calculations by Ceder *et al*. It is therefore clear that NaO_2 formation is not only kinetically but also thermodynamically favored in an increased oxygen partial pressure even at higher temperatures and lead to a higher scale growth (up to 20 nm). [20]

The equation for non-aqueous Na−O_2 cathode electrochemistry using, e.g. ether based electrolytes like diglyme is shown below [19].

$$Na^+ + e^- + O_2 \leftrightarrow NaO_2, \qquad E^0 = 2.27\ V, Vs\ Na/Na^+$$

According to a previous report by Kang *et al.,* [21] flat low index surfaces of NaO_2 are activated by a chemical barrier up to 0.8 V. Moreover, according to HSE Hybrid functional calculations the bandgap of NaO_2 is found to be as low as 1.11 eV [21]. Siegel *et al*. [22] however, reported that GW calculations revealed wide bandgap of 5.30 eV and 6.65 eV for NaO_2 and Na_2O_2, respectively. Nevertheless, a 1.3 eV experimental bandgap is previously reported for KO_2 (similar to NaO_2) [23].

It should be noted that this significant discrepancy is obtained using higher-level computational methods like HSE and GW. This illustrates the computational complexity of the Na-O_2 system, which in part, is due to the computational challenges in describing the thermodynamics of reactions involving superoxide vs. peroxide species and to the high temperature phase of NaO_2 ($Pa\bar{3}$) being dynamically stabilized relative to the orthorhombic low temperature phase (*Pnnm*) by procession of misaligned superoxide species (see Figure 1). Such effects and energetics are generally not accounted for in DFT or higher-level calculations, making it highly challenging to describe the relative stability of NaO_2 vs. Na_2O_2 at finite temperatures. In the following, we describe a comparatively simple GGA-level computational approach using metal chloride reference energies and entropic contributions, which yields excellent agreement with experimental observations.

Here, we will discuss overpotentials and free energies of the reaction mechanisms as a function of temperature. In this study, other alternative pathways on some selected stepped model surfaces *i.e*., (001) and (100) for NaO_2 and $(1\bar{1}00)$ for Na_2O_2. Hence, the step surfaces are likely to give accessible barriers and favorable nucleation sites for minimum overpotentials, as it has been reported in case of Li–O_2 [24].

II. COMPUTATIONAL METHODOLOGY

Here, we present fundamental investigations at the DFT-level [25,26] using the PBE (Perdew-Burke-Ernzerhof) [27] exchange correlation functional as implemented in the GPAW package [28] using the Atomic Simulation Environment (ASE) [29]. The GPAW package is built on a real space grid algorithm based on the projector augmented wave (PAW) function method with frozen core approximation [30,31]. The study is conducted in the materials of interest in the Na−O_2 battery, *i.e.* NaO_2 and Na_2O_2.

The NaO_2 growth/depletion mechanism is studied on stepped (001) and (100) surfaces of the face-centered $Pa\bar{3}$ NaO_2 structure with a lattice constant of 5.523 Å.[21] All presented calculations are spin-polarized with an initial magnetic moment values of 0.5 located in each O atom in NaO_2. The k-points are sampled with a $2 \times 4 \times 1$ Monkhorst-Pack mesh. The supercell consists of 60-72 atoms. The vacuum layer between periodic images along the Z-axis is 20 Å. Here, due to the computational complexity in describing stepped surfaces of Na_2O_2, the highly similar and well-studied stepped $(1\bar{1}00)$ surface model of Li_2O_2 (space group $P6_3/mmm$) is adopted instead for Na_2O_2 reaction mechanism studies on the stepped surface. The stepped $(1\bar{1}00)$ Na_2O_2 surface with a super cell consisting of a 56-64 atoms slab with a 18 Å vacuum layer between periodic images along the z-axis is used to study the reaction mechanism. The k-points are sampled with a (4,4,1) Monkhorst-Pack mesh and 0.18 Å grid point spacing is used. Atomic energy optimization calculations are performed until all forces are less than 0.03 eV/Å.

For the free energy calculations, we calculate the translational contributions to the entropy and enthalpy (through the heat capacity) for O_2 in the gas phase at STP and the difference in the rotational contribution between Na_2O_2 and NaO_2/O_2, where the O_2^{2-} species are constrained whereas the O_2^- and O_2(g) species are effectively free rotors at STD. To a first approximation, we only include these contributions, since the vibrational properties of O_2(g) , O_2^- and O_2^{2-} are very similar and and expected to cancel, and the rotational properties of O_2(g) and O_2^- ions are equally similar and expected to cancel (see Section 3).

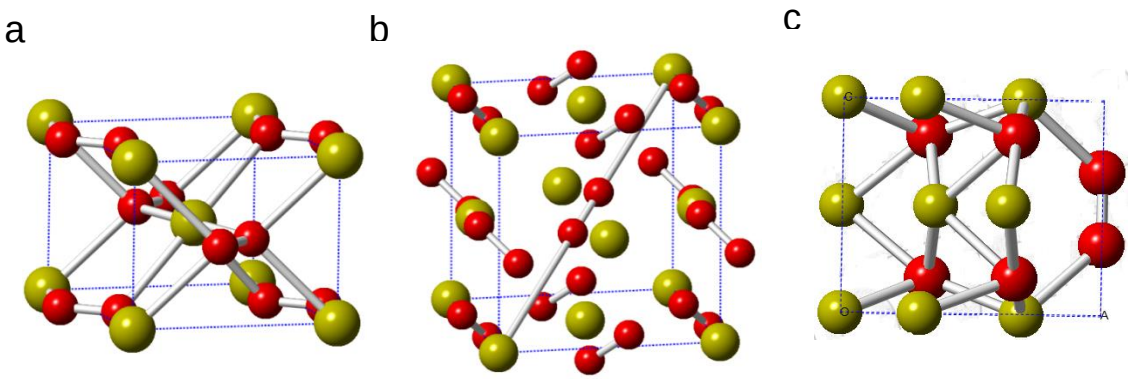

Figure 1: a) *Pnnm* NaO_2 orthorhombic structure with lattice constant a = 4.26 Å, b = 5.44 Å, c = 3.36 Å. b) Face-centered cube $\mathbf{Pa\bar{3}}$ NaO_2 structure (Pyrite) with lattice constant a = 5.523 Å. c) Hexagonal Na_2O_2 structure space group of $\boldsymbol{P\bar{6}2m}$ with lattice constants of a = 6.39 Å, b = 6.39 Å and c = 4.6 Å. Color: Grey (Sodium), Red (Oxygen).

The computational sodium electrode approach is used in the free energy calculations, analogous to the lithium electrode approach used for Li-Air batteries.[32,33] Defined as, $\mathrm{U} = 0$, when bulk Na anode and Na ions in solution ($Na^+ + e^-$) are at equilibrium. The free energy change of the reaction is shifted by $-neU$ at an applied bias, where n is the number of electrons. From Hummelshøj *et al*. reports kinks and step surfaces are favorable nucleation sites for low overpotential reaction mechanisms. [24]

At neutral bias all reaction steps are downhill, but at an applied potential, the free energy difference changes for each step calculated as,

$$\Delta G_{i,U} = \Delta G_i - eU \quad (1)$$

The limiting discharge potential ($\mathrm{U_{discharge}}$) is the lowest free energy step, $\Delta \mathrm{G_{min}}$, along the reaction path which becomes uphill at an applied potential. Likewise, the largest free energy step, $\Delta G_{i,max,}$ that is last to become downhill for the reversed reaction at an applied potential called limited charge potential ($\mathrm{U_{charge}}$) obtained as,

$$U_{discharge} = \min[-\Delta G_i/e] \text{ and } U_{charge} = \max[-\Delta G_i/e] \quad (2)$$

The calculated effective equilibrium potential can be obtained as $U_o = -\Delta G/ne$. All reaction steps are downhill at neutral bias, however at an applied potential, the free energy difference changes for each step calculated from equation (1), where n is the number of electrons.

Systematic errors in description of superoxides, peroxides and monoxides have previously been documented by various groups and accounted for in various ways [24,20,34]. Here, we adopt the approach of Christensen *et al*.[34] using NaCl as reference to obtain the metallic Na energy. In line with Christensen *et al*.[34] an energy correction is applied to O_2(g), which is notoriously difficult to describe correct with DFT. With the used computational code the optimal energy correction of O_2(g) is -0.33 eV. The used approach is chosen as it reduces the systematic errors significantly, while allowing consistent calculation of surfaces with various oxide species present required for studying reactions in Na-O_2 batteries.

III. RESULTS AND DISCUSSIONS

3.1. Enthalpy of Formation and Equilibrium Potential

To evaluate the accuracy of the calculations, bulk enthalpies of formation are compared with experiment [35] as seen in Table 1. The calculated formation enthalpies are converted to free energies at standard conditions (ΔH_{form} -> ΔG_{form}) using experimental entropies [35] and the equilibrium potential calculated. As an alternative to using experimental entropies, we predict the equilibrium potentials with the approximation that the temperature dependence can be described solely considering the translational and rotational degrees of freedom of O_2(g). As superoxide ions are known to rotate easily in the NaO_2 pyrite phase at room temperature, rotational degrees of freedom will to a good approximation cancel for NaO_2. This is not the case for NaO_2, where the orientation of peroxide ions is well defined at relevant temperatures. The approximation has obvious flaws, e.g. will it not be able to capture the low temperature structural changes of NaO_2 due to differences in the rotational degrees of freedom of superoxide ions in different phases. It does, however, have the advantage of being very simple to calculate with standard thermodynamics. Comparison with experiment also proves the simple assumption to be reasonable (see Figure 2). It can also be seen that the experimental data for NaO_2 at 0 K is identical to the calculational result for the P*nnm* structure.

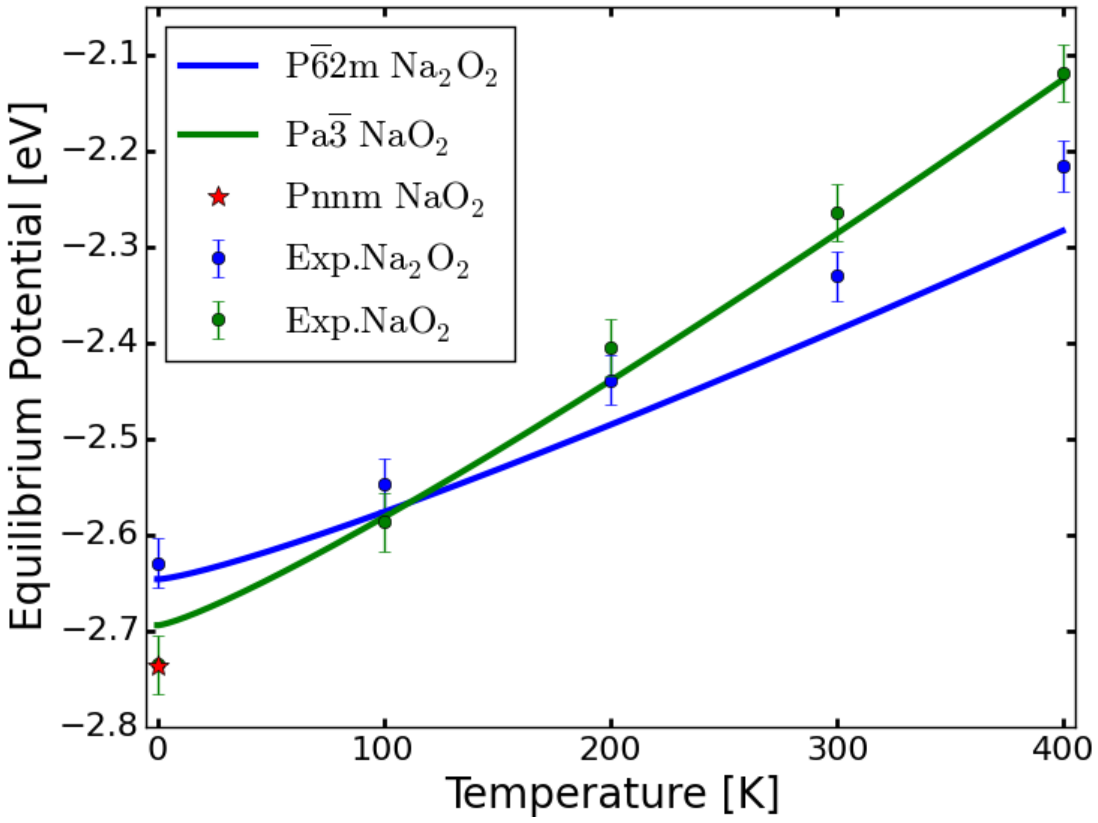

Figure 2: DFT-based equilibrium potentials predicted with the approximation that the temperature dependence is only due to the translational and rotational degrees of freedom for O_2(g). This simple approximation is in good alignment with experimental data and reproduces relatively small free energy differences between Na_2O_2 and NaO_2.

As seen in Table 1, the difference in equilibrium potential for NaO_2 and Na_2O_2 at standard conditions is less than 0.1 eV, for purely experimental results, calculated enthalpies with experimental entropies, and purely theoretical calculations with approximated entropies. This indicates that required overpotentials in electrochemical reactions to Na_2O_2 and NaO_2 could be decisive for the product formation.

Table 1: Calculations for Na_2O_2 and the pyrite phase of NaO_2 are compared with experimental values [32] in parentheses. Equilibrium potentials are calculated both using experimental entropies and with the approximation that all temperature dependence is due to translational and rotational degrees of freedom of O_2(g).

	$\Delta_f H°$ (eV)	Equil. Pot. (eV) (experimental ΔS)	Equil. Pot. (eV) (approximation)
$\mathbf{Pa\bar{3}\ NaO_2}$	-2.74 (-2.71)	-2.30 (-2.27)	-2.29 (-2.27)
$\mathbf{P\bar{6}2m\ Na_2O_2}$	-5.29 (-5.32)	-2.39 (-2.33)	-2.39 (-2.33)

3.2. NaO_2 Growth/desorption Mechanisms on Selected Step Surfaces

The four steps NaO_2 growth/depletion is investigated on stepped (001) and (100) NaO_2 surface. The method does not include specific effects of the electrolyte or possible kinetic barriers. DFT calculations can estimate the preferred pathways for the dis/charge mechanisms comparing the energies of the adsorbed species at every single step. The stepped surface is constructed manually from the bulk crystal in a specific direction in such a way that four sodium superoxide species are added (removed) at the step site for the complete pathways of growth (depletion).

In general, NaO_2 growth/depletion mechanisms on the step NaO_2 surfaces follows a four step mechanism; each step comprises of either Na* or NaO_2* species (electrochemical steps) or O_2 species (chemical step) and both are taken in to account to generate all possible pathways. Among which, the most thermodynamically favorable path with the low overpotential is selected. Thus, as shown in Figure 5, the first step for (001) step surface is adsorption of the first NaO_2 on bottom left site, which is the limiting discharge potential (2.39 V) step and is followed by adsorption of the second NaO_2 species to the bottom right site with the binding energy of 2.57 V, the third and the fourth NaO_2 species are adsorbed by 2.63 V and 2.71 V respectively. The fourth step is the limiting charge potential step and the growth mechanism is completed by forming 4 sodium superoxide species. The charging or desorption process follows the same reaction steps applied in reverse order (right to left), see Figure 3.

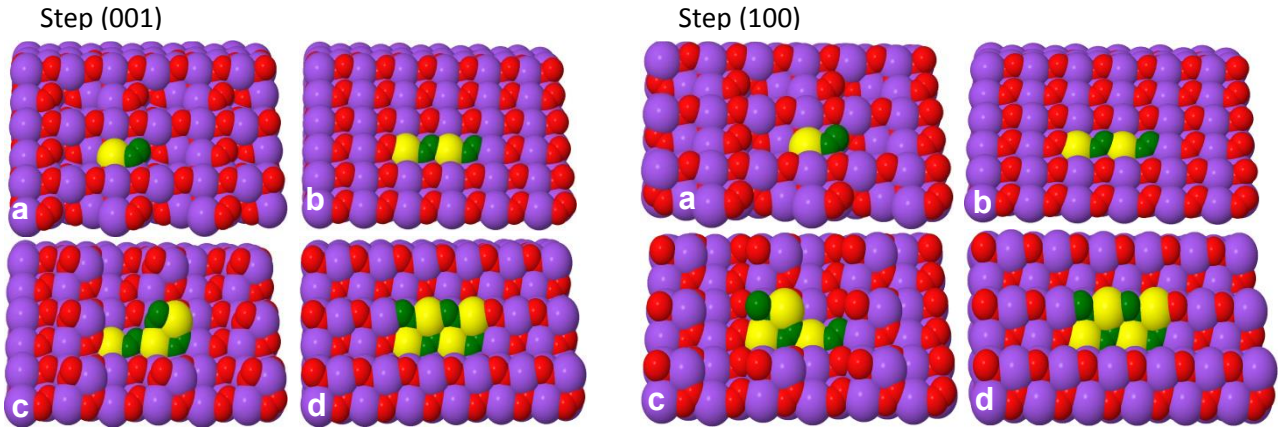

Figure 3: A 4 step growth/desorption mechanism on the step surface (001) and (100) of NaO_2. a) and b) NaO_2 adsorbs to the bottom site. c) and d) 2 NaO_2 adsorbs to the top site to complete the 4 formula units NaO_2 reaction mechanism. Color: Na purple and O red. Deposit atoms: Na yellow and O green.

Table 2: (Dis)/charge potentials and overpotentials (in V) estimated for NaO_2 growth/depletion mechanism studies on (001) and (100) step surfaces. Metallic Na energy is obtained from NaCl reference [34].

	Step (001)	**Step (100)**
$\mathbf{U_o}$	2.57	2.56
$\mathbf{U_{discharge}}$	2.39	2.32
$\mathbf{U_{charge}}$	2.71	2.85
$\mathbf{\eta_{discharge}}$	0.18	0.28
$\mathbf{\eta_{charge}}$	0.14	0.28

The growth/depletion mechanisms studies on the stepped NaO_2 surface revealed that the fundamental overpotentials in both discharge and charge processes are very low, which also has been experimentally observed [19]. Fundamentally, the overpotential in Li_2O_2 is also very low but experimentally different depending on the experimental conditions e.g. current density and parasitic chemistry.

Thus, the limiting discharge (charge) potential for the (001) stepped surface calculated using GGA is found to be 2.39 V (2.71 V) and the calculated effective equilibrium potential is 2.57 V (compared to the experimental value, $U_{0,Exp}$ = 2.27 V) leads discharge (charge) overpotential of 0.18 V (0.14 V) for the growth (depletion) mechanism. The growth/desorption mechanisms studies on the stepped NaO_2 surface revealed that the fundamental overpotentials in both discharge and charge processes are very low which also has been experimentally observed [19]. Fundamentally, the overpotential in Li_2O_2 is also very low but experimentally different depending on the experimental conditions e.g. current density and parasitic chemistry. [24]

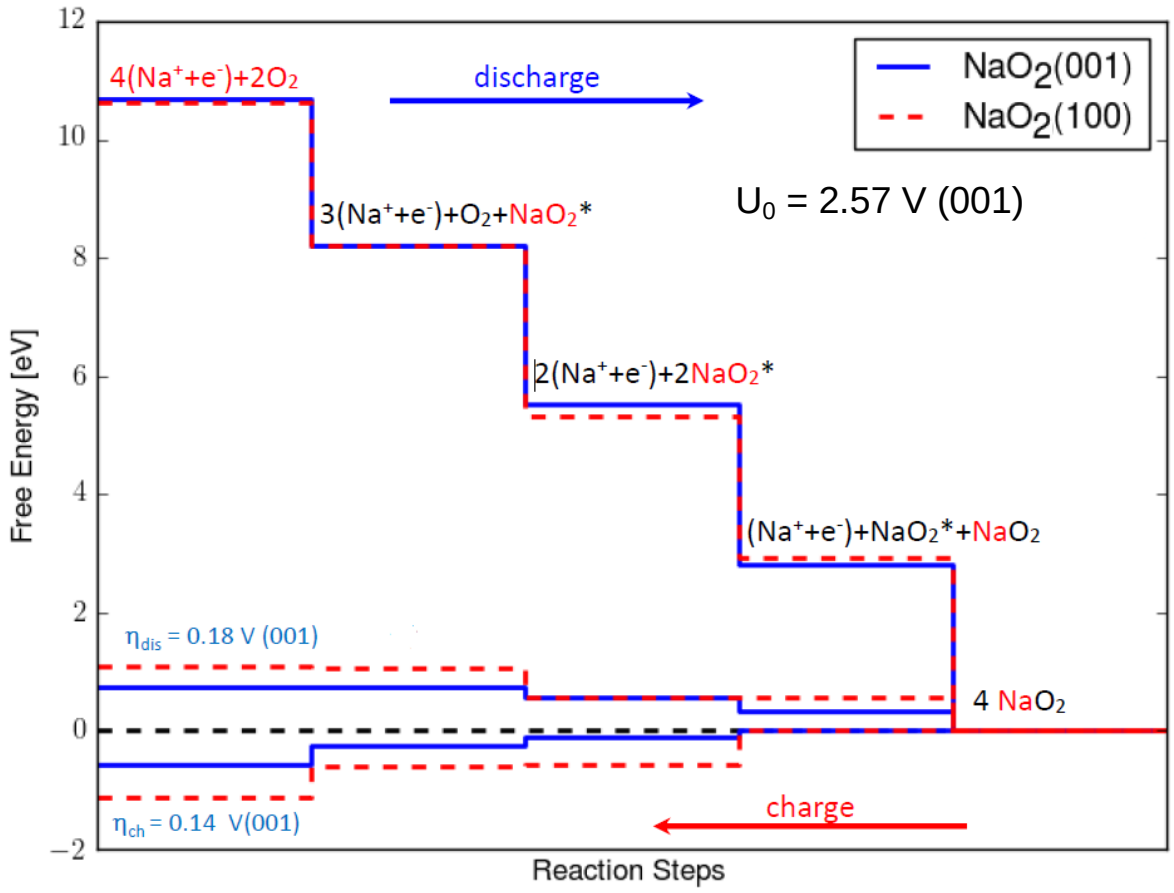

Figure 4: The calculated free energy diagram for NaO_2 growth/desorption mechanisms on stepped (001) and (100) NaO_2 surfaces using PBE.

Pathways involving a purely thermochemical step for O_2 ab/desorption are all found to be inactive due to high activation energy. The NaO_2 growth/depletion mechanism studies revealed a low overpotential path consists of four steps addition or removal of NaO_2 species electrochemically. The bulk equilibrium potential is in a good agreement with the experimental value of 2.27 V.

The NaO_2 growth/desorption mechanism studies revealed a low overpotential path consists of four electrochemical steps addition or removal of NaO_2 species. Pathways involving a purely thermodynamic step for O_2 ab/desorption are all found to be inactive due to high overpotentials. The bulk equilibrium potential is in a good agreement with the experimental value of 2.27 V however the surface equilibrium potential is off by 0.3 V compared to the bulk, it could be due to a variation in O-O bond length and magnetic moment at the surface and in bulk.

3.3. Na_2O_2 Growth/Desorption Mechanisms on $(1\bar{1}00)$ Step Surface

The free energy diagram in Figure 5 show four steps growth mechanism consists of two formula units of Na_2O_2 growth mechanism on the step $(1\bar{1}00)$ Na_2O_2 surface (from a to d). The first step adsorption of NaO_2* species (Fig. 1a) adsorbs with the binding energy by 1.89 V which is the potential limiting step for discharge. The next step is the addition of Na* species (Fig 1b) adsorbed with the binding energy of 2.02 V. This is again followed by additions of NaO_2* and Na* respectively with the binding energies of 2.69 V and 2.15 V (the third step is potential limiting step for charge) (Fig 1c and 1d). The full growth mechanism is accomplished with the two formula units of Na_2O_2 growth at the step surface with equilibrium potential of 2.19 V. The charging process follows the reverse order.

Previous work by Hummelshøj *et al*. [32] have reported that the pure Li_2O_2 growth mechanism follows 4 steps reaction mechanism, where all reaction steps are electrochemical. The equilibrium potential can be obtained as $U_0 = -\Delta G/2e$. The equilibrium potential of bulk Na_2O_2 is found to be 2.39 which is in good agreement with the experimental value of 2.33 V.

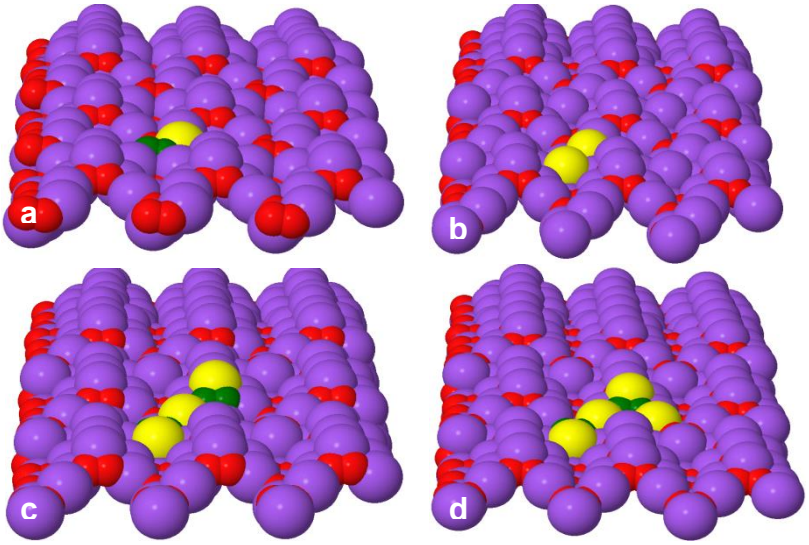

Figure 5: Reaction mechanism studies on stepped Na_2O_2 $(1\bar{1}00)$ surface follows 4 steps Na_2O_2 growth pathways during discharge. a) First NaO_2 adsorbs. d) Second NaO_2. c) First Li. f) Second Li adsorbs to the surface completing growth of 2 formula units of Na_2O_2. Atoms labeled as: Li purple and O red. Deposit atoms shown as: Li yellow and O green.

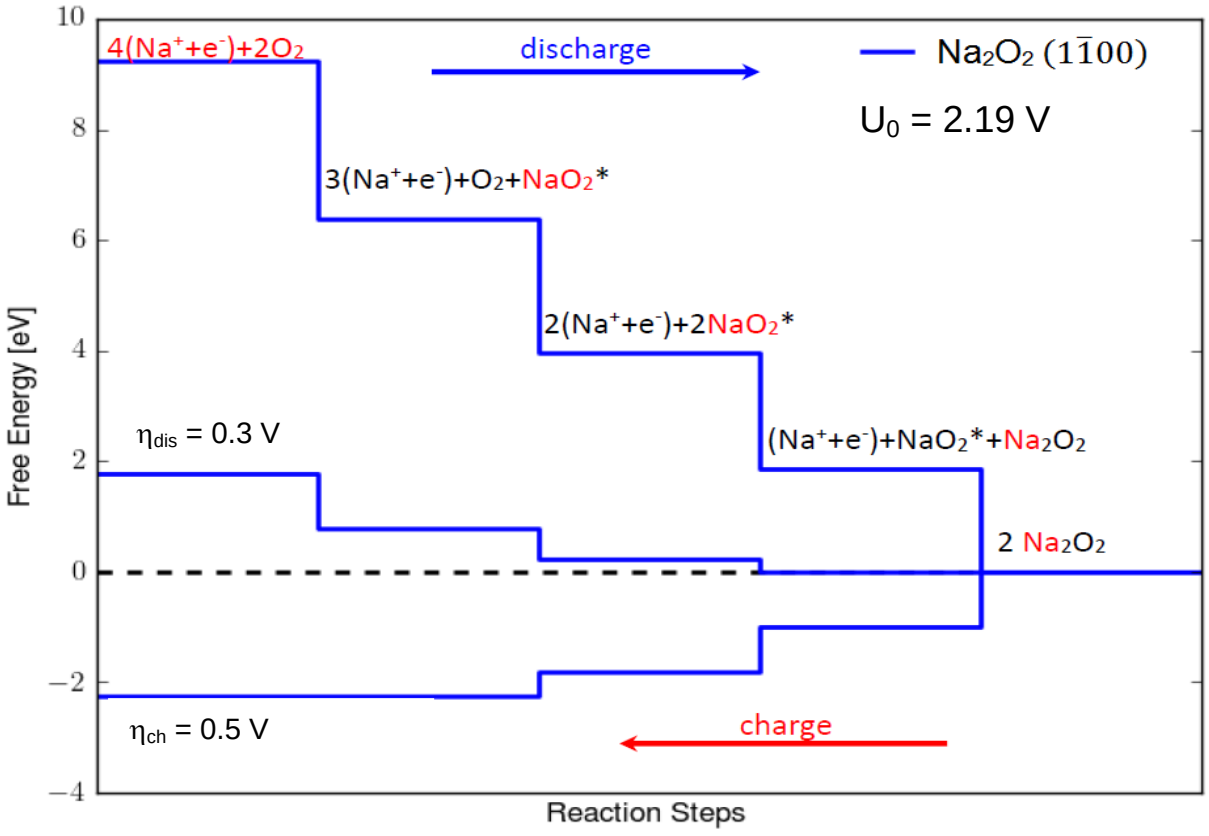

Figure 6: Calculated free energy diagrams for a four steps discharge mechanism from stepped $(1\bar{1}00)$ Na_2O_2 surface. The sodium metallic energy is obtained from NaCl reference.

The discharge occurs as described in Figure 5 and 6, among various paths the minimum low overpotential path resulting in discharge (charge) potential of 1.80 V (2.69 V) and overpotentials of 0.3 V (0.5 V). The preferred growth mechanism follows the following subsequent adsorption steps NaO_2*, Na*, NaO_2* and Na* respectively to form 2 formula units of Na_2O_2 at the step surface to complete the growth (* refers to surface adsorption). Here, the charging process follows the same reaction steps as discharging but in reverse (from d to a in Figure 5 and right to left in Figure 6). Pathways involving a purely thermochemical step for O_2 ab/desorption are all found to be inactive due to high overpotential.

IV. CONCLUSIONS

A rechargeable Na-O_2 battery could display a number of advantages over other similar technologies at STD, but too low overpotentials for NaO_2 formation at the cathode compared to the high overpotential for Na_2O_2 formation/depletion is limiting the performance of the Na-O_2 battery. Here, reaction mechanism studies on selected step surfaces of NaO_2 and Na_2O_2 materials that are formed at the cathode of rechargeable non-aqueous Na-O_2 battery.

The NaO_2 discharge/charge mechanism on stepped (001) and (100) NaO_2 surfaces in nonaqueous Na-O_2 batteries were studied using DFT (PBE) calculations. In this model, the effect of low index step surface on the growth/depletion mechanisms is investigated. The NaO_2 reaction mechanism model consists of four electrochemical steps, adsorption of four NaO_2 species step by step at the cathode surface. The equilibrium potential for bulk high temperature NaO_2 structure calculated from sodium chloride reference and oxygen reference is found to be 2.29 V that is in good agreement with the experiment 2.27 V. Moreover, this studies also revealed low discharge (charge) overpotential 0.18 V (0.14 V).

Similarly, four steps reaction mechanism on stepped $(1\bar{1}00)$ Na_2O_2 surface were studied using DFT calculations. The Na_2O_2 growth mechanism consists of four electrochemical steps. Accordingly, the subsequent growth mechanism steps are adsorption of NaO_2*, Na*, NaO_2* and Na* to form 2 Na_2O_2 at the cathode surface. For charge similar reaction steps apply in reverse order. The equilibrium potential of bulk Na_2O_2 is 2.39 V estimated using the sodium chloride reference is in excellent agreement with the experimental value of 2.33 V. In general, the DFT calculations and few experimental results show that, the Na_2O_2 reaction mechanism has high overpotentials compared to low overpotential paths in NaO_2 formation.

The NaCl-correction scheme has improved the understanding of this system and similarly why only including the translational O_2 contributions is a simple and reasonable way to estimate the temperature dependence of the NaO_2 to Na_2O_2 transition. Further, it is shown that by going beyond room temperature, it may be possible to circumvent the higher overpotentials for Na_2O_2 formation and thereby increase the specific capacity of the Na-O_2 battery

Acknowledgements

The authors acknowledge support of this work from the ReLiable project (project nr. 11-116792) funded by the Danish Council for Strategic Research Programme Commission on Sustainable Energy and Environment.

References

(1) Lee, J.-S.; Tai Kim, S.; Cao, R.; Choi, N.-S.; Liu, M.; Lee, K. T.; Cho, J. Metal-Air Batteries with High Energy Density: Li-Air versus Zn-Air. *Adv. Energy Mater.* **2011**, *1* (1), 34–50.

(2) Whittingham, M. S. *Metal-Air Batteries: A Reality Check. Meeting Abstract*; 2012; p 1099.

(3) Linden, D.; Reddy, T. B. *HANDBOOK OF BATTERIES*.

(4) Younesi, R.; Norby, P.; Vegge, T. A New Look at the Stability of Dimethyl Sulfoxide and Acetonitrile in Li-O2 Batteries. *ECS Electrochem. Lett.* **2014**, *3* (3), A15–A18.

(5) Younesi, R.; Veith, G. M.; Johansson, P.; Edström, K.; Vegge, T. Lithium Salts for Advanced Lithium Batteries: Li–metal, Li–O $_2$, and Li–S. *Energy Environ. Sci.* **2015**, *8* (7), 1905–1922.

(6) Girishkumar, G.; McCloskey, B.; Luntz, a. C.; Swanson, S.; Wilcke, W. Lithium−Air Battery: Promise and Challenges. *J. Phys. Chem. Lett.* **2010**, *1* (14), 2193–2203.

(7) Luntz, A. C.; Mccloskey, B. D. Nonaqueous Li − Air Batteries : A Status Report. **2013**.

(8) Mekonnen, Y. S.; Knudsen, K. B.; Mýrdal, J. S. G.; Younesi, R.; Højberg, J.; Hjelm, J.; Norby, P.; Vegge, T. Communication: The Influence of CO2 Poisoning on Overvoltages and Discharge Capacity in Non-Aqueous Li-Air Batteries. *J. Chem. Phys.* **2014**, *140*, 121101.

(9) Yang, S.; Knickle, H. Design and Analysis of Aluminum / Air Battery System for Electric Vehicles. **2002**, *112*, 162–173.

(10) Tarascon, J. M.; Armand, M. Issues and Challenges Facing Rechargeable Lithium Batteries. *Nature* **2001**, *414*, 359–367.

(11) Balaish, M.; Kraytsberg, A.; Ein-Eli, Y. A Critical Review on Lithium-Air Battery Electrolytes. *Phys. Chem. Chem. Phys.* **2014**, *16*, 2801–2822.

(12) Armand, M.; Tarascon, J. M. Building Better Batteries. *Nature* **2008**, *451*, 652–657.

(13) Hojberg, J.; Knudsen, K. B.; Hjelm, J.; Vegge, T. Reactions and SEI Formation during Charging of Li-O2 Cells. *ECS Electrochem. Lett.* **2015**, *4*, A63–A66.

(14) Das, S. K.; Lau, S.; Archer, L. a. Sodium–oxygen Batteries: A New Class of Metal–air Batteries. *J. Mater. Chem. A* **2014**.

(15) Hartmann, P.; Bender, C. L.; Vračar, M.; Dürr, A. K.; Garsuch, A.; Janek, J.; Adelhelm, P. A Rechargeable Room-Temperature Sodium Superoxide (NaO2) Battery. *Nat. Mater.* **2013**, *12* (3), 228–232.

(16) Zhao, N.; Li, C.; Guo, X. Long-Life Na-O_2 Batteries with High Energy Efficiency Enabled by Electrochemically Splitting NaO_2 at a Low Overpotential. *Phys. Chem. Chem. Phys.* **2014**, *16* (29), 15646–15652.

(17) Kim, J.; Lim, H.-D.; Gwon, H.; Kang, K. Sodium-Oxygen Batteries with Alkyl-Carbonate and Ether Based Electrolytes. *Phys. Chem. Chem. Phys.* **2013**, *15* (10), 3623–3629.

(18) Hartmann, P.; Bender, C. L.; Sann, J.; Dürr, A. K.; Jansen, M.; Janek, J.; Adelhelm, P. A Comprehensive Study on the Cell Chemistry of the Sodium Superoxide (NaO2) Battery. *Phys. Chem. Chem. Phys.* **2013**, *15* (28), 11661–11672.

(19) Mccloskey, B. D.; Garcia, J. M.; Luntz, A. C. Chemical and Electrochemical Di Ff Erences in Nonaqueous Li − O 2 and Na − O 2 Batteries. **2014**, 2–7.

(20) Kang, S.; Mo, Y.; Ong, S. P.; Ceder, G. Nanoscale Stabilization of Sodium Oxides: Implications for Na-O2 Batteries. *Nano Lett.* **2014**, *14* (2), 1016–1020.

(21) Lee, B.; Seo, D.-H.; Lim, H.-D.; Park, I.; Park, K.-Y.; Kim, J.; Kang, K. First-Principles Study of the Reaction Mechanism in Sodium–Oxygen Batteries. *Chem. Mater.* **2014**, *26* (2), 1048–1055.

(22) Yang, S.; Siegel, D. J. Intrinsic Conductivity in Sodium-Air Battery Discharge Phases: Sodium Superoxide vs. Sodium Peroxide. *Chem. Mater.* **2015**, 150508165039003.

(23) Khan, A. U.; Mahanti, S. D. Collective Electron Effects of O2− in Potassium Superoxide. *J. Chem. Phys.* **1975**, *63* (6), 2271.

(24) Hummelshøj, J. S.; Luntz, a C.; Nørskov, J. K. Theoretical Evidence for Low Kinetic Overpotentials in Li-O2 Electrochemistry. *J. Chem. Phys.* **2013**, *138*, 034703.

(25) Ernzerhof, M.; Scuseria, G. E. Perspective on “Inhomogeneous Electron Gas.” *Theor. Chem. Acc.* **2000**, *103*, 259–262.

(26) W. Kohn and L. J. Sham. Self-Consistent Equation Including Exchange and Correlation Effects. *Phys. Rev.* **1965**, *140*, A 1133 – A 1138.

(27) Perdew, J. P.; Burke, K.; Ernzerhof, M.; of Physics, D.; Quantum Theory Group Tulane University, N. O. L. 70118 J. Generalized Gradient Approximation Made Simple. *Phys. Rev. Lett.* **1996**, *77* (18), 3865–3868.

(28) Enkovaara, J.; Rostgaard, C.; Mortensen, J. J.; Chen, J.; Dułak, M.; Ferrighi, L.; Gavnholt, J.; Glinsvad, C.; Haikola, V.; Hansen, H. a; et al. Electronic Structure Calculations with GPAW: A Real-Space Implementation of the Projector Augmented-Wave Method. *J. Phys. Condens. Matter* **2010**, *22*, 253202.

(29) Bahn, S. R.; Jaconsen, K. W. An Object-Oriented Scripting Interface to a Legacy Electronic Strcture Code. *Comput. Sci. Eng.* **2002**, *4*, 56–66.

(30) Blochl, P. E. Projected Augmented-Wave Method. *Phys. Rev. B* **1994**, *50*, 17953–17979.

(31) Mortensen, J. J.; Hansen, L. B.; Jacobsen, K. W. A Real-Space Grid Implementation of the Projector Augmented Wave Method. *Phys. Rev. B* **2005**, *71*, 035109.

(32) Hummelshøj, J. S.; Blomqvist, J.; Datta, S.; Vegge, T.; Rossmeisl, J.; Thygesen, K. S.; Luntz, a C.; Jacobsen, K. W.; Nørskov, J. K. Communications: Elementary Oxygen Electrode Reactions in the Aprotic Li-Air Battery. *J. Chem. Phys.* **2010**, *132* (7), 071101.

(33) Nørskov, J. K.; Rossmeisl, J.; Logadottir, A.; Lindqvist, L.; Lyngby, D.-; Jo, H. Origin of the Overpotential for Oxygen Reduction at a Fuel-Cell Cathode. **2004**, 17886–17892.

(34) Christensen, R.; Hummelshøj, J. S.; Hansen, H. a.; Vegge, T. Reducing Systematic Errors in Oxide Species with Density Functional Theory Calculations. *J. Phys. Chem. C* **2015**, *119* (31), 17596–17601.

(35) Chase, M. W.; National Institute of, S.; Technology, NIST-JANAF thermochemical tables. American Chemical Society ; American Institute of Physics for the National Institute of Standards and Technology: [Washington, D.C.]; Woodbury. N.Y. 1998.